Transport and Targeted Binding of Polymer-Coated Nanoparticles in Unsaturated Porous Media

by

Najmeh Jaberi

A thesis
Presented to the University of Waterloo
In fulfillment of the
Thesis requirement for the degree of
Doctor of Philosophy
In
Civil Engineering

Waterloo, Ontario, Canada, 2021

Examining Committee Membership

The following served on the Examining Committee for this thesis. The decision of the Examining Committee is by majority vote.

External Examiner	Kela Weber Associate Professor, Royal Military College of Canada
Supervisor(s)	Neil R. Thomson Professor, University of Waterloo
Internal Member	Monica Emelko Professor, University of Waterloo
Internal Member	Stefano Normani Assistant Professor, University of Waterloo
Internal-external Member	Frank Gu Professor, University of Toronto

Author's Declaration

This thesis consists of material I authored or co-authored: see Statement of Contributions included in the thesis. This is a true copy of the thesis, including any required final revisions, as accepted by my examiners.

I understand that my thesis may be made electronically available to the public.

Statement of Contributions

Chapter 2 of this thesis been prepared with the intent for submission to a peer reviewed journal, and is co-authored by myself, Dr. Stuart Linley (now at University of Cambridge, UK), my supervisor Dr. Neil R. Thomson (University of Waterloo), Dr. Kevin McVey, Dr. Kanwartej Sra (Chevron Energy Technology Company, Houston, Texas, USA), and Dr. Frank X. Gu (now at University of Toronto). I designed and performed all experiments, ran all simulations, analyzed the data, prepared the figures and wrote the manuscript. S.L prepared nanoparticles used for all experiments and provided support with editing and review; and N.R.T, supervised the project and helped with experimental design, provided the modeling tool, aided with data interpretation, writing and editing and critically reviewed the manuscript.

Chapter 3 of this thesis has been prepared with the intent for submission to a peer reviewed journal, and is co-authored by myself, Dr. Stuart Linley (now University of Cambridge, UK), Dr. Neil R. Thomson (University of Waterloo), Kevin McVey, Dr. Kanwartej Sra (Chevron Energy Technology Company, Houston, Texas, USA), and Dr. Frank X. Gu (now at University of Toronto). Similar to the previous contribution, I designed and performed all experiments, executed all simulations, analyzed the data, prepared the figures and wrote the manuscript. S.L prepared nanoparticles used for all experiments and provided support with editing and review, N.R.T, supervised the project and helped to design the experiments, modified the conceptual modeling tool, aided with data interpretation, writing editing and critically reviewed the manuscript.

Chapter 4 of this thesis has been prepared with the intent for submission to a peer reviewed journal, and is co-authored by myself, Dr. Stuart Linley (now at University of Cambridge, UK), and Dr. Neil R. Thomson (University of Waterloo). I designed and performed the experiments, executed all simulations, analyzed the data, prepared the figures and wrote the manuscript. S.L aided with performing the experiment, prepared nanoparticles, helped with editing the manuscript and review. N.R.T supervised the project, helped with the design of the experiment, writing, editing, and provided a critical review of the manuscript.

Abstract

The effectiveness of most *in situ* remedial technologies lies on successful delivery of reagents to a target treatment zone. Advances in nanoparticle (NP) materials has led to the targeted delivery concept in which the NP coating is engineered so that the NPs are able to transport in a porous medium but bind to specific target contaminants. By taking advantage of this capability, the accumulation of NPs within a target treatment zone increases with a concomitant decrease in the mass of NPs required to achieve treatment goals. In addition to delivery parameters, the transport and binding behaviour of NPs depends on the properties of the NPs and the porous media. NPs coated with an amphiphilic co-polymer (Pluronic) can be tuned so that they have stability in an aqueous suspension as well as preferential binding to oil-water interfaces. The Pluronic coating is comprised of a middle hydrophobic segment which provides sufficient affinity to an oil phase through hydrophobic interactions and two outer, hydrophilic segments that extend into the aqueous phase surrounding the nanoparticle and prevent nanoparticle aggregation. While extensive investigations on this type of engineered NP coating in saturated conditions have been completed, the transport and targeted binding behaviour of these coated NPs in unsaturated conditions has not been studied. Thus, the focus of this research effort was to comprehensively examine the ability of amphiphilic co-polymer coated NPs to transport and bind to a target contaminant in unsaturated porous media.

Initially, the effect of porous medium texture, initial water saturation, input dosage, and flowrate on NP transport behaviour was evaluated and then targeted NP binding to a representative non-aqueous phase liquid (i.e., crude oil) zone was examined using a series of short column experiments. To isolate the effects of controlling parameters, NPs (iron oxide (Fe_3O_4) core material) coated with a high polymer concentration which enhances transport and stability were used except for the targeted NP binding systems where NPs (cobalt ferrite ($CoFe_2O_4$)) with lower polymer concentration which promotes binding to an oil phase was used. Building on the findings from the short-column experiments, the transport and binding ability of these NPs at a spatial scale representative of the unsaturated zone above a shallow aquifer system was evaluated using a 1.4-m long column. Finally, to evaluate the capability of the NPs to bind to a heterogeneous crude oil-impacted zone in a less constrained unsaturated system, a two-dimensional physical model experiment was performed. Reactive transport models were used in all investigative phases to support experimental observations and characterize the transport and binding of these NPs.

Results from the short column experiments demonstrated that NP retention was influenced by the initial water content, injection flowrate, and clay and silt content. Both initial water content and injection flowrate affect air saturation and hence the abundance of air/water interfaces where NPs are retained. Increased retention of the NPs was observed in sediments with a higher clay and silt content as a result of the larger surface area. NP retention was insensitive over the range of injection doses examined. The transport model that represented the observed NP breakthrough data included mobile and immobile porosity regions, and a simple attachment/detachment reaction with nonlinear Langmuirian blocking for NP retention. The NP binding data demonstrated preferential attachment to the crude oil-impacted sediment under unsaturated conditions. As a result of the lower polymer concentration used in the binding experiments, depth-dependent straining was required to simulate the observed NP retention profile.

Observations from the 1.4-m long column experiments also demonstrated preferential NP attachment to the crude oil-impacted sediment consistent with the short-column experiments. Again, depth-dependent straining was required in the transport model to reproduce the observed NP retention near the top of the column. However, as a result of the longer distance that the NP solution travelled, compared to the short-column experiments, a first-order mass loss term was used in the transport model to represent suspected NP aggregation and trapping deeper in the column system.

Results from the two-dimensional physical model experiment showed that NP transport and targeted binding were significantly influenced by physical heterogeneities present in the system. Preferential attachment of NPs to the crude oil zone was confirmed; however, substantial retention of NPs was also observed between the infiltration gallery and the top of the crude oil zone as a result straining consistent with the column experiments. Despite the demonstrated targeted binding of the NPs to the crude oil zone, the presence of preferential flow paths reduced NP delivery efficiency to portions of the crude oil zone. An acceptable description of the observed NP retention behaviour in this two-dimensional system was obtained using a single porosity transport model with depth-dependent straining and kinetic attachment/detachment reactions.

This thesis provides critical information on the transport of Pluronic-coated NPs in unsaturated porous media and targeted binding to crude oil. The important role of initial water content, flow rate and porous medium texture on NP transport and retention behaviour was established. In addition, the effect of travel distance and heterogeneity on NP targeted binding capability was revealed. The supporting modelling efforts showed that physical and chemical nonequilibrium considerations were required to better represent the observed NP transport and binding behaviour in unsaturated experimental systems investigated. Multiple lines of evidence demonstrated targeted binding of the Pluronic-coated NPs to a crude oil zone in unsaturated porous media which will ultimately improve the treatment efficiency of these systems. The delivery of these NPs to a target NAPL zone distal from the injection location may be a challenge due to the possible aggregation observed at increased travel distances. Furthermore, like other flushing-based technologies, physical heterogeneities may restrict access of the NP solution throughout the NAPL zone. For efficient targeting these factors should be considered during the design of a NP delivery system to treat a NAPL source in the unsaturated zone.

Acknowledgments

I would first and foremost like to express my considerable thanks to my supervisor, Prof. Neil R. Thomson, for not only his valuable technical guidance and advice through all these years but also for his support, especially through the toughest last year of my PhD program during the pandemic. I am sincerely thankful and honored that he accepted me as his student and gave me this opportunity to grow and be the best of me by challenging me through this research path. Also I am grateful for his assistance in the modeling effort and providing the 1DUSAT simulation software. Without his support this thesis would not have been possible.

I would like to thank the members of my advisory committee Dr. Kela Weber, Dr. Monica Emelko, Dr. Stefano Normani, and Dr. Frank Gu for sharing their time and technical expertise in evaluating my thesis and participating in my defence. I specially would like to thank Dr. Monica Emelko for mentoring the colloid related theories and providing me with materials which helped me expand my knowledge in this matter.

Special thanks to Dr. Stuart Linley who has been providing technical support and feedbacks, helping with conducting experiments, and preparing nanoparticles. I highly appreciate his assistance throughout this research.

Financial support for this research was provided by Chevron Energy Technology Company, University of Waterloo International Doctoral Student Award, Provost Doctoral Entrance Award for Women – Engineering, University of Waterloo Graduate Scholarship, and Natural Sciences and Engineering Research Council (NSERC) of Canada Discovery Grant (N.R. Thomson).

I would like to extend my gratitude towards anyone who took part in this research including University of waterloo staff – present, past and retired (Shirley Chatten, Felipe Solano, Terry Ridgway, Mark Sobon, and Mark Merlau). I should thank Mohammad Haghshenas for his help and guidance in HYDRUS 2D model simulations. I am also grateful to our research group members including graduate students (Dr. Saeid Shafieiyoun, Zahra Sadeghi Ardestani, Iolanda Montagnese, Andrea Marrocco, Bill McLaren, and Dr. Michelle cho) whom I was blessed to have crossed paths during my PhD studies.

I would not be here without constant support and love of my family (my parent, my brother, and my aunt). I am so grateful to them whom never stopped believing in me and cheering me up during this

challenging PhD path and gave me courage to keep on moving forward after each failure. I would like to specially thank my brother, Ali Jaberi, for all his support and faith in me, who never let me give up and was my best cheerleader.

I also owe this thesis to my husband, Dr. Armin Abedini, for his unconditional love and support. From the day we met to now he kept encouraging me while listening to my rant and cry. My gratitude goes to him for standing beside me through the toughest times of my PhD journey and carrying the burden.

Thank you all from the bottom of my heart.

Dedication

To my parents, Mr. Mehrzad Jaberi and Mrs. Mahnaz Mortahan

Table of Contents

List of Figures

List of Tables

Chapter 1

Introduction

1.1 General Background

Soil and groundwater contamination by petroleum hydrocarbons (PHCs) resulting from activities including exploration, refining and transportation is a global concern. PHCs such as crude oil, a non-aqueous phase liquid (NAPL), are persistent and can be detrimental to the environment and human health (Labud et al., 2007; USEPA, 2000). Upon release on the ground surface, a NAPL will migrate through the unsaturated zone down to the water table, and due largely to capillary forces some mass will be retained in the unsaturated zone forming a long-term contaminant source. As a result of infiltration or seasonal water table fluctuations in a shallow aquifer system, leachate from the NAPL source will reach to the saturated zone resulting in contamination. Significant technical remediation challenges are associated with PHC persistence and their relative inaccessibility. Due to limitations associated with *ex situ* remediation methods, research efforts have focused on developing novel *in situ* technologies (Kuppusamy et al., 2016).

Nanoremediation is an emerging technology which involves the injection of an aqueous solution of nano-size particles into a NAPL source. This *in situ* technology benefits from the properties of the nanoparticles (NPs) such as their small size that allows them to evade filtration by the porous medium, and their large surface area that enhances interactions with contaminants (Molnar et al., 2016; O'Carroll et al., 2013; Schrick et al., 2004; Tasco et al., 2014). Recently, polymeric materials have been used to coat NPs to facilitate their mobility in porous media and to preferentially bind to a target contaminant (Bishop et al., 2010; Linley et al., 2019, 2020a,b; Saleh et al., 2007; Schrick et al., 2004). As a result, these engineered NPs can accumulate within a target treatment zone through enhanced adsorptive interactions between the NPs and the NAPL interface which ultimately reduces the mass of NPs required to achieve treatment goals (Bishop et al., 2010). As a result, the environmental risk of unwanted NP distribution and deposition beyond the target treatment zone is reduced. Implementation of these NPs for *in situ* remediation is a novel technique which benefits from enhanced delivery strategies with targeted binding to a specific NAPLs.

Demonstrated targeted delivery of NPs to a NAPL zone has been reported using various NP coating materials such as amphiphilic polymers (Bishop et al., 2007; Phenrat et al., 2010; Saleh et al., 2007). Recently, Linley et al. (2019, 2020a,b) achieved targeted binding of NPs towards a NAPL in saturated conditions by adding a copolymer NPs coating (Pluronic) to the surface of the NPs. This coating promoted hydrophobic interactions with the NAPL and enhanced NP stability in an aqueous solution (through electrosteric stabilization) which were found to be proportional to the polymer structure and concentration. Improved binding to the NAPL was achieved using a polymer with a more hydrophobic structure or lower polymer concentration, while better NP stability and mobility was attained as the hydrophobicity of the polymer was decreased or the polymer concentration increased. Despite extensive investigations contributing to our understanding of the binding response of these engineered NPs to a NAPL in saturated systems, their transport and binding behavior in unsaturated porous media remains to be investigated.

1.2 NP Transport and Binding in Porous Media

To develop effective delivery systems for a complex subsurface environment and to protect groundwater, knowledge of NP transport and binding behavior is essential. NP transport through a porous medium is primarily governed by advection, wherein NPs move with the water flow (in the pore fluid) (Elliott and Zhang, 2001). NP transport from the pore fluid to near the surface of sediment grains is affected by three mechanisms: Brownian diffusion, dominant for small particles (<100 nm); and interception and gravitational sedimentation dominant for larger particles and aggregates (Tufenkji and Elimelech, 2004).

The transport of NPs within a porous medium has been found to directly correlate with the moisture content (e.g., Bradford et al., 2002; Torkzaban et al., 2008; Wan and Wilson, 1994). In saturated porous media, NP retention is limited to attachment at solid-water interfaces (SWIs) or sediment grains, and pore straining (i.e., physical trapping of NPs in pores and pore throats). While NP transport in unsaturated porous media is further complicated by the air phase present in the system which provides additional retention sites at air-water interfaces (AWIs), low velocity regions such as air-water-solid (AWS) interfaces, and thin water films formed around air-filled pores or sediments (Bradford et al., 2003; Wan and Wilson, 1994). Straining is also more pronounced in unsaturated porous media due to the constrained water flow in regions with smaller pores (Bradford et al., 2002, 2003) and thin water films (Wan and Wilson, 1994). It has been commonly reported in literature that the retention of different NPs increased with decreasing moisture content due to the presence of more AWIs leading to an increasing number of retention sites (e.g., Chen et al., 2008; Kumahor et al., 2015a; Yecheskel et al., 2018;). Torkzaban et al. (2008) also suggested that the extent of immobile flow regions increased with decreasing water content which results in greater retention of NPs in these regions.

The transport of NPs and their interaction with a porous medium depends on a number of factors including physicochemical properties of NPs, composition of the porous medium, and delivery rate of the NP solution (Chowdhury et al., 2011; Fang et al., 2009; Predelus et al., 2017; Torkzaban et al., 2008). For example, increased transport of NPs has been reported with a higher NP injection dosage (product of the input concentration and volume of the injected NP solution) which contributes to saturation of retention sites, and subsequent repulsive interaction between the retained NPs and those in the pore fluid (Chowdhury et al., 2011). In contrast, some studies showed higher mobility of NPs at lower concentrations due to less agglomeration (i.e., sticking of NPs together and formation of clusters) (Phenrat et al., 2010). Fang et al.

(2009) reported significant impact of porous medium texture on the retention of TiO_2 NPs as observed by considerable retention of NPs in saturated soil columns with higher clay content as a result of additional straining. In addition, Torkzaban et al. (2008) reported that increasing the flow rate decreased the retention of NPs in unsaturated soil columns due to an increase in hydrodynamic forces acting on particles weakly retained at the SWIs as well as reduced immobile porosity.

In addition to the air phase present in the unsaturated zone and various controlling factors, NP transport and binding may be affected during their migration over long distances and by natural heterogeneities. NPs are typically required to travel a nominal distance from a delivery location to access a target source zone. The relative influence of the rate of NP collisions, interactions, detachment and attachment at the SWIs can vary with transport distance (Bradford et al., 2011; Tufenkji and Elimelech 2004). However, only a few studies have reported on the transport behavior of NPs over longer transport distances (e.g., Hoggan et al., 2016). Moreover, delivery of NPs, as remediation agents or as delivery vehicles for treatment reagents, is controlled by various physical and chemical heterogeneities. These heterogeneities may significantly affect the ability of NPs to bind to a target treatment zone and ultimately reduce treatment efficiency (Phenrat et al., 2010, 2011). To mimic field conditions, representative multidimensional systems have been previously used to provide insight into the *in situ* delivery and transport behavior of NPs; however, all these studies were in saturated conditions and used nano-zero valent iron (nZVI) exclusively (e.g., Busch et al., 2014; Phenrat et al., 2010, 2011). It is essential to expand our knowledge of NP transport and binding behavior in unsaturated (see **Error! Reference source not found.**) and more realistic conditions in order to support the esign of pilot-scale investigations.

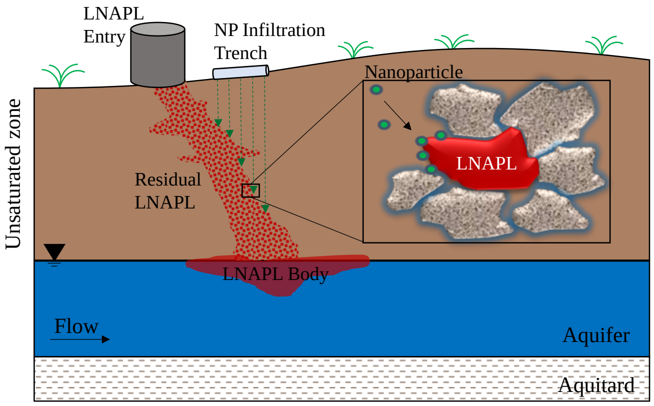

Figure 1-1. Targeted delivery of engineered NPs to residual LNAPL within the unsaturated zone; NPs infiltrated through the unsaturated zone using an infiltration trench transport through porous medium, and selectively bind to an oil phase as illustrated in the insert.

Reactive transport models are typically used in conjunction with experimental data to predict the fate and transport of NPs. The advection dispersion reaction equation (ADRE) combined with a reversible kinetic attachment/detachment model is commonly used to describe NP transport and retention in porous media (e.g., Bradford et al., 2002; Liang et al., 2013a,b; Rahmatpour et al., 2018). Several studies have reported that transport models which allow for depth-dependent retention in addition to reversibility of retained NPs provide a better description of NP behaviour particularly when natural porous media is used (Liang et al., 2013a). Some studies have suggested that when the ADRE formulation is extended to account for both mobile and immobile porosity regions, the results provide an improved description of the transport of NPs in unsaturated porous media (Padilla et al. 1999; Predulus et al. 2017; Šimůnek and van Genuchten, 2008). This expanded formulation can take account of mass transfer of NPs between mobile and immobile flow regions, thus representing both physical and chemical nonequilibrium transport. Nevertheless, due to the added complexity, the use of this expanded NP transport model is limited.

1.3 Research Questions

The overarching objective of this research effort was to advance the earlier work dealing with the transport and binding of Pluronic-coated NPs in saturated conditions (Linley et al. 2019, 2020a,b) to unsaturated conditions at different spatial scales. To satisfy the research gaps discussed above, the following four Research Questions (RQ) were developed:

RQ-1. What is the role of water content, porous medium texture, flowrate, and NP concentration on the transport and binding of Pluronic-coated NPs in unsaturated conditions?

RQ-2. How does a longer travel distance affect Pluronic-coated NP transport and binding behavior in an unsaturated porous medium?

RQ-3. What is the potential for Pluronic-coated NPs to preferentially bind to a heterogeneous NAPL zone in a multidimensional unsaturated porous medium system?

RQ-4. What is the capability of reactive transport models to capture that observed transport and binding behavior of Pluronic-coated NPs in unsaturated porous media?

1.4 Scope

This thesis consists of five additional chapters: three core chapters (Chapters 2, 3 and 4) addressing the four research questions; Chapter 5 summarizing the major conclusions and contributions, along with recommendations for future work; and Chapter 6 that provides a complete list of the literature cited. Three appendices contain supplementary figures, tables and text for each of the core chapters.

The effect of some key controlling parameters (RQ-1) including, initial water saturation, porous medium texture, input dosage, and flowrate on NP transport behavior was investigated using a series of short column experiments. NP targeted binding to a crude oil zone was also explored. These NPs were coated with an amphiphilic co-polymer which can be tuned to provide stability in aqueous suspension as well as preferential binding to oil-water interfaces. NPs coated with a higher polymer concentration which enhances transport and stability were used initially to isolate the effects of controlling parameters, while NPs with lower polymer concentration which promotes binding to an NAPL were used for the targeted binding experiments. Each column experiment involved a pulse injection of NPs and tracer followed by Millipore water at the same flowrate until near complete breakthrough of the NPs and tracer was achieved. To support the experimental observations and characterize the transport and binding of the NPs, a reactive transport model (1DUSAT) (Thomson, 2019) which included mobile and immobile flow regions and a simple attachment/detachment reaction with nonlinear Langmuirian blocking was used (RQ-4). A single porosity model was used for saturated systems. The hydraulic data (flow breakthrough profile), as well as tracer and NP breakthrough responses collected during the experiments were used for model calibration. Chapter 2 is devoted to the results and discussion from these short column experiments and modelling investigations of NP transport and binding behavior, and addresses RQ-1 and RQ-4.

Results from an investigation into the transport and binding ability of these NPs in a 1.4-m long column (RQ-2) are discussed in Chapter 3. To mimic a field delivery method, an infiltration system was used for the delivery of NPs (with the lower coating concentration) into the column system to bind to a crude oil zone emplaced in the middle of the system. An operational approach was adopted to deliver sufficient NPs to the crude oil zone while minimizing migration deeper into the system. To describe NP transport and retention behavior the 1DUSAT model was also used (RQ-4).

The investigations presented in Chapter 2 and Chapter 3 were performed in 1-D systems. In contrast, Chapter 4 describes a two-dimensional physical model experiment that focuses on the capability of the NPs (with lower coating concentration) to bind to a heterogeneous crude oil zone in an unsaturated system (RQ-3). To mimic a potential field delivery method, an infiltration gallery was used to deliver NPs into the 2-D system. An available 2-D numerical model, HYDRUS 2-D, was used to characterize the unsaturated transport and binding behavior of the NPs (RQ-4).

Chapters 2, 3 and 4 were prepared with the intent for submission to peer-reviewed journals, hence, they were prepared as stand-alone chapters and some repetition across these chapters is inevitable. A full list of contributions for the co-authored material is provided in the front pages of this thesis.

Chapter 2

Transport and Targeted Binding of Pluronic-coated Nanoparticles in Unsaturated Porous Media

Abstract

Effective targeted delivery of engineered nanoparticles (NPs) to treat petroleum hydrocarbons present in the unsaturated zone requires an understanding of their transport behaviour in these systems. A series of column experiments was conducted using NPs coated with an amphiphilic co-polymer to explore the role of initial water saturation, flow rate, input dosage, and porous medium texture. NP targeted delivery towards a crude oil impacted zone was also investigated. As the initial water content increased with a concomitant reduction in air saturation, the degree of tailing present in the NP breakthrough curves (BTCs) reduced, and the mass of NPs recovered increased. Air saturation is correlated with the magnitude of air-water interfaces, which provide additional NP retention sites. At a lower injection flow rate, NP retention increased due to a longer residence time and comparatively high air saturation. NP transport behaviour was not sensitive to NP injection dose over the range tested. Increased retention and retardation of the NP BTC was observed in sediments with a higher clay and silt content as a result of the larger surface area. NPs coated with a lower concentration of a Pluronic block co-polymer to promote binding were preferentially retained within a crude oil zone. Results from a model which accounts for both mobile and immobile flow regions provided a good description of the asymmetrical NP BTCs generated. To represent NP retention behaviour, a simple attachment/detachment model with nonlinear Langmuirian blocking was used, except when NPs coated with the lower concentration of a Pluronic block co-polymer were employed and, in this case, a depth-dependent straining term was also required. The initial water saturation and flow rate did not have an appreciable impact on the NP attachment rate coefficient, while it was an order of magnitude larger for columns packed with higher clay and silt content sediments. The detachment rate coefficient decreased with lower initial water saturation, flow rate, and increased for the higher clay and silt content sediment. The attachment rate coefficient was two-orders of magnitude higher for the crude oil impacted sand than that for the non-impacted sand demonstrating preferential NP attachment. As a result of the lower NP polymer concentration coating used to promote increased attachment to crude oil, higher retention was observed near the column inlet and was captured quantitatively by adding a depth-dependent straining term to the model. This retention behaviour represents a combination of irreversible attachment at the air-water interfaces and straining near the column inlet enhanced by the formation of NP aggregates. The findings from this study contribute to our understanding of the transport and binding behaviour of Pluronic-coated

NPs in unsaturated conditions and, in particular, the role of initial water content, flow rate and porous medium texture. Demonstrated targeted delivery of these NPs to a crude oil zone is an important step towards their application as a treatment reagent.

2.1 Introduction

Soil and groundwater contamination by light non-aqueous phase liquids (LNAPLs) such as gasoline and crude oil can be detrimental to the environment and human health (Labud et al., 2007). Following a near surface release, a LNAPL will migrate downward through the unsaturated zone where some of the mass is retained largely due to capillary forces (Brown et al., 2017). Since this immobile LNAPL mass represents a long-term contaminant source, *in situ* treatment methods able to effectively target this mass would be valuable to remediation practitioners (Kuppusamy et al., 2016; Schrick et al., 2004). Nanoremediation methods benefit from the high reactive surface area provided by nano-size particles which offer enhanced interactions with target contaminants (Molnar et al., 2016; O'Carroll et al., 2013; Schrick et al., 2004; Tratnyek and Johnson, 2006), and have the potential to minimize clean-up cost and time relative to more traditional technologies (Tosco et al., 2014; Tratnyek and Johnson, 2006). Nanomaterials such as metal oxides, carbon nanotubes, and bimetallic nanoparticles have been explored for the treatment of a variety of contaminants including heavy metals, chlorinated compounds, and polychlorinated biphenyls (Karn et al., 2009).

A major challenge for nanoremediation methods is to ensure efficient delivery of the nanoparticles (NPs) throughout the target treatment zone while at the same time avoiding migration of the NPs beyond this zone which may exacerbate the environmental impact of the site (Bishop et al., 2010; Elliott and Zhang, 2001). One effective strategy to minimize this issue is targeted delivery, in which specific NP coating materials such as polymers and surfactants are used to ensure both NP mobility in the porous medium and binding to a target NAPL (Bishop et al., 2010; Linley et al., 2019). By taking advantage of this capability, the accumulation of NPs within the target treatment zone increases with a concomitant decrease in the mass of NPs required to achieve treatment goals (Bishop et al., 2010). Consequently, treatment efficiency may be increased and the environmental risk of unwanted NP migration and deposition beyond the target treatment zone can be reduced. This targeted delivery concept mimics the injection of functionalized nanoparticles carrying therapeutic payloads into the human body to target specific receptors on tumors, diseased cells or tissues (Davis et al., 2008).

Targeted binding of NPs to a NAPL source zone present in porous media has been investigated with some success through various modifications of the coating material (Bishop et al., 2010; Phenrat et al., 2011; Quinn et al., 2005; Sridevi and Lakshmi, 2013). The concept of targeted binding of NPs to a NAPL interface was first demonstrated by Saleh et al. (2005) using a triblock copolymer coating around an iron NP core. Quinn et al. (2005) demonstrated enhanced partitioning of surfactant-stabilized (nonionic sorbitan triolate (Span 85)) nano-zero valent iron (nZVI) particles to NAPL in a field-scale investigation, while Saleh et al. (2007) used amphiphilic copolymer NPs with a high hydrophobe/hydrophile ratio for targeted binding at

NAPL/water interfaces. A similar approach was evaluated by Phenrat et al. (2011) who reported improved targeted binding of copolymer coated nZVI particles to a NAPL. Recently, we reported successful targeted binding of engineered iron oxide core NPs towards NAPL-impacted sand under saturated conditions (Linley et al., 2019; Linley et al., 2020a,b). This targeted binding was achieved by adding a copolymer coating to the surface of iron oxide NPs which promoted hydrophobic interactions with a target NAPL (crude oil) as well as stability in an aqueous solution. The hydrophobicity and stability of the NPs were found to be proportional to the polymer structure and concentration. Nanoparticle attachment in oil-impacted sand was found to increase when using polymers with a more hydrophobic structure and at lower concentrations, while nanoparticle retention in non-impacted sand columns decreased with decreasing hydrophobicity and increasing concentration. Although we have examined some factors affecting the binding response of these engineered NPs to crude oil in saturated systems, their transport and binding behaviour in unsaturated systems has yet to be established.

The transport of NPs in a porous medium is controlled by their retention within pores (Lecoanet and Wiesner, 2004) which is predominantly affected by the system moisture content, the composition of the porous medium sediments, the physiochemical properties of the NPs, and the delivery rate of the injected NP solution (Kumahor et al., 2016; Lin et al., 2010; Park et al., 2016). In addition, in some porous media, the porosity can be separated into mobile porosity where water flow is continuous, and immobile porosity where water is present as isolated clusters but loosely connected to the mobile porosity (Kumahor et al., 2015b). Both solutes and NPs can enter the immobile porosity by slow advection and/or diffusion (Gao et al., 2006); however, some NPs may be excluded from the immobile porosity due to their size (Bradford et al., 2003).

Moisture content is often cited as a controlling parameter positively correlated with NP transport. In saturated porous media, retention is usually limited to pore straining and attachment at solid-water interfaces (SWIs), while in unsaturated porous media the presence of an air phase introduces additional retention sites such as air-water interfaces (AWIs) and low velocity regions such as air-water-solid (AWS) interfaces (Bradford et al., 2003; Torkzaban et al., 2008). Retention at SWIs includes NP attachment to sediment grains which depends on the physiochemical characteristics of the NPs and the sediment surface properties. An AWI can retain NPs by either capillary, electrostatic, or hydrophobic forces that depend on the NP surface properties (Wan and Wilson, 1994). Straining involves the physical trapping of NPs in pores and pore throats which occurs in both saturated and unsaturated media; it is typically predominant in unsaturated porous media due to constrained water flow in regions with smaller pores (Bradford et al., 2003) and thin water films (Wan and Wilson, 1994). Chen et al. (2008) investigated the role of AWIs on the retention of titanium dioxide (TiO_2) NPs, and concluded that more NPs were retained at lower water saturations corresponding to film straining (i.e., retention of NPs in thin water films formed around air-filled pores or sediments). Yecheskel et al. (2018) found that the retention of silver NPs to sediments increased with decreasing moisture content due to the presence of more AWIs leading to an increasing number of retention sites, supporting this claim. Kumahor et al. (2015a) suggested that the retention of citrate-coated silver NPs in unsaturated sand packed columns was controlled by the presence of AWIs and SWIs. Using different flow rates corresponding to different water contents (0.17, 0.29 and 0.35 v/v), the results from their model simulations indicated non-equilibrium attachment at the SWIs, and equilibrium attachment at the AWIs. Torkzaban et al. (2008) investigated the impact of water content on NP transport using experimentation and modeling tools, and suggested that the extent of immobile porosity increased with decreasing water content which lead to greater retention of NPs (carboxylate-modified latex) in these regions. In contrast, Fang et al. (2013b) showed that the retention of TiO_2 NPs was not enhanced by decreasing water saturation in sand columns likely due to repulsive interactions between the negatively charged AWI and the TiO_2 NPs. Rahmatpour et al. (2018) also reported a negligible effect of water saturation on the mobility of silver NPs in undisturbed soil columns.

Transient flow through an unsaturated system alters the water saturation and, consequently, the retention of NPs at AWIs and SWIs (Prédélus et al., 2017; Torkzaban et al., 2008). Increasing the flow rate decreases the retention of NPs due to a reduced immobile porosity and an increase in hydrodynamic forces acting on particles weakly retained at the SWIs (Torkzaban et al., 2008). Gao et al. (2006) found that increased flow rate in unsaturated columns (granular quartz sand) remobilized NPs retained at the AWS interfaces, and from immobile porosity regions. Liang et al. (2013a) observed less retention of surfactant-stabilized silver NPs at a higher Darcy velocity (0.02 vs 0.006 cm/min) in columns (loamy sand) under unsaturated conditions. Kumahor et al. (2015b) investigated the effect of flow rate on the transport of citrate-coated silver NPs in unsaturated columns and reported less retention with increasing Darcy velocity (0.04 to 0.28 cm/min) as a result of reduced immobile porosity. Similarly, Prédélus et al. (2017) reported reduced NP retention at a higher Darcy velocity (0.127 vs 0.025 cm/min) presumably due to increased hydrodynamic forces acting on particles weakly retained at the AWIs.

Natural porous medium properties such as texture (i.e., sand, silt, clay content) or grain size can significantly impact the transport and retention of NPs. Fang et al. (2009) observed significantly increased retention of TiO_2 NPs in saturated soil columns with increasing clay content as a result of higher straining. Fang et al. (2013a) later investigated the transport of carbon nanotubes in 14 different soils using column experiments, and showed increased NPs retention in soils with smaller grain sizes (d_{50}: 45.8 vs. 165.3 μm) and higher clay contents (53 vs 1 % v/v) likely due to the presence of smaller pores which resulted in additional NP straining. Raychoudhury et al. (2014) investigated the retention of stabilized-nZVI particles in columns packed with four different silica sands (d_{50}: 775, 510, 250, 150 µm) and observed more retention in the finer sand, which was attributed to straining as a dominant mechanism. Similarly, Kamrani et al. (2018) also reported higher retention of carbon-based NPs at the SWIs in a smaller grain size quartz sand (0.2-0.5 mm vs 1.5-2.0 mm) under both saturated and unsaturated conditions presumably due to increased straining. Hoggan et al. (2016) investigated the mobility of TiO_2 NPs in a lysimeter packed with layers of fine and medium sand, and observed higher retention of NPs in the fine sand layers which was attributed to smaller pore sizes and an increase in attachment sites.

Increased transport of NPs has been reported with higher dosing (product of the input concentration and volume of the injected NP solution) which contributes to blocking or saturation of retention sites (i.e., SWIs, AWIs, and AWS surfaces), and subsequent repulsive interaction between the retained NPs and those in the aqueous phase (Chowdhury et al., 2011). Kasel et al. (2013) showed a direct correlation between the mobility of multi-wall carbon nanotubes and input concentration. Chowdhury et al. (2011) found that a higher TiO_2 injection concentration (800 vs 100 mg/L) contributed to increased effluent mass recovery from saturated columns, possibly, as a result of particle-particle repulsion. In contrast, Phenrat et al. (2010) reported higher mobility of nZVI at lower concentrations (30 mg/L) likely because of less agglomeration (i.e., sticking of two or more NPs and formation of clusters).

The research presented here is a continuation of the work reported by Linley et al. (2019, and 2020a,b) on the design, transport, and binding of Pluronic-coated NPs. Linley et al. (2019) applied a tunable amphiphilic co-polymer coating to iron oxide NPs, and demonstrated stability of these NPs in aqueous suspension, as well as interaction with a hydrophobic phase such that the NPs preferentially bound to NAPL-water interfaces in comparison to a non-impacted porous medium. The transport and targeted binding behaviour of these NPs was demonstrated through saturated column experiments, binding batch tests, and NP transport modeling (Linley et al., 2019; Linley et al., 2020a,b). The results showed that 54 % of the mass of injected NPs eluted (i.e., were recovered) from non-impacted sand packed columns (15 cm and 100 cm long), while almost all NPs were retained in NAPL (crude oil)-impacted sand packed columns (0.4 % recovery). Linley et al. (2020b) also reported that the binding affinity of these NPs to the NAPL was enhanced by decreasing the NP coating concentration, increasing the NAPL concentration, and increasing temperature. Collectively this effort demonstrated that targeted-delivery of NPs to crude oil-impacted porous media in saturated conditions is possible, and contributed to our understanding of the application conditions required for efficient targeting. Based on their observations (Linley et al, 2020a) it was reported that binding of these NPs was not dependent on DLVO interactions that are impacted by solution ionic strength. In this paper, we extend our previous findings to unsaturated conditions by initially evaluating the effect of initial water saturation, porous medium texture, input dosage, and flowrate on NP transport behaviour and then examine targeted NP binding to crude oil-impacted sediments using a series of column experiments. To support the experimental observations, and characterize the unsaturated transport and binding of the NPs in unsaturated systems, a reactive transport model was used.

2.2 Materials and Methods

2.2.1 Materials

Iron oxide NPs (Fe-NPs) and cobalt ferrite NPs (CoFe-NPs) employed in this study were prepared as described by Linley et al. (2019) and Linley (2019). The structure of each NP is a three-layer hierarchical sphere with a core of iron oxide (Fe_3O_4) or cobalt ferrite ($CoFe_2O_4$), a middle layer of oleic acid, and an outer layer of a Pluronic block co-polymer (P104, L62) (poly (ethylene oxide)-poly (propylene oxide)-poly (ethylene oxide) (PEO-PPO-PEO)). As previously mentioned, the transport and binding properties of these NPs are affected by the composition and concentration of the Pluronic coating (Linley et al., 2020a). In this work, Fe-NPs with a Pluronic coating concentration of 10 g/L (NP diameter of 7.6 ± 1.8 nm) and CoFe-NPs with a Pluronic coating concentration of 2.5 g/L (NP diameter of 89.7 ± 28.2 nm) were used (Linley, 2019). NPs with the higher coating concentration (identified as the transport formulation) have increased mobility and stability in aqueous suspension, whereas NPs with the lower coating concentration (identified as the binding formulation) have higher affinity towards a NAPL. Transmission electron microscopy (TEM) images of each of the NP formulations are presented in Appendix A (see Figure A-1). TEM data indicated distinct particles with crystalline spherical cores within an amorphous polymer coating. The lower coating concentration (i.e., 2.5 g/L) resulted in the presence of small, individually stabilized NPs along with spherical NP aggregates with an average size of 115 ± 41 nm. While for the higher coating concentration (10 g/L) the presence of large aggregates diminished, as sufficient amount of Pluronic fully saturated the surface of all individual NPs.

Crude oil (sour crude, API gravity 13.3 (density of 0.977 g/cm^3), average linear carbon number of 25.1, kinematic viscosity 4.75 x 10^{-4} m^2/s at 40 °C) was provided by Chevron Energy Technology Company (Houston, TX, USA). Sodium bromide (NaBr, ACS grade, ≥ 99%), dichloromethane (DCM, > 99.9 %), hydrogen peroxide (H_2O_2, 30%), ethanol (ACS grade, 99%), hexane (ACS Grade, >98.5%), hydrochloric acid (HCl, ACS grade, 37%), and nitric acid (HNO_3, ACS grade, 70%) were purchased from Fisher Scientific (Mississauga, ON). Iron (II) sulphate heptahydrate (FeSO4 · $7H_2O$, >99%), iron (III) chloride hexahydrate ($FeCl_3$ · 6H2O, >99%), ammonium hydroxide (NH_4OH, 28%-30% in water), oleic acid (>90%), sodium oleate (> 90% fatty acids (as oleic acid) basis), iron (III) nitrate nonahydrate (Fe(NO3)3·9H2O, ACS grade, > 98%), cobalt (II) nitrate (Co(NO3)2·6H2O, ACS grade, > 98%), sodium hydroxide (NaOH, ACS grade, > 98%), 1-pentanol (ReagentPlus® grade, >99%) were purchased from

Sigma Aldrich. Pluronic co-polymer P104 and L62 were gifted by BASF, Canada. All chemicals were used as received. Millipore water was obtained from a direct water purification system (EMD Millipore, 18.2 MΩ·cm at 25 °C).

Sandy aquifer material (denoted here as "Borden Sand" (BS)) (d_{10} of 75 µm, Cu of 2.7) with 2 % gravel, 92 % sand, 5.9 % silt, and 0.1 % clay was collected from 1 m below ground surface (bgs) at the University of Waterloo Groundwater Research Facility at the Canadian Force Base (CFB) Borden ON, Canada. BS is comprised of mostly quartz with minor amounts of other minerals, and has a total iron content of 1 % wt (29.6 g/kg) (Ball et al. 1990). A silty sand (d_{10} of 0.9 µm, Cu of 39) with 29 % sand, 59 % silt, and 12 % clay was collected from a depth of 1.5 m bgs from the North Campus (NC) of the University of Waterloo ON, Canada. Prior to use, the BS was sieved (1 mm mesh) to remove larger particles, repeatedly rinsed with DI water until the filtrate ran clear, and oven dried at 90 °C overnight. The NC sediment (NCS) was first dried at 90 °C overnight, gently homogenized, and then sieved (1 mm mesh). A synthetic silty sand (SSS) (d_{10} of 40 µm, Cu of 4) material (75 % sand, 23 % silt and 2 % clay) was created by homogenizing 80 % of the BS with 20% of the NCS. Particle size distributions were determined using standard methods (ASTM D 422, 2007) (see Figure A-2). All materials were stored in air-tight polyethylene bags at 4°C until used. Only the BS and SSS were used in this study.

2.2.2 Column experiments

All experiments were performed using Plexiglas columns (length of 15 cm, inner diameter of 3.5 cm) uniformly dry-packed in 1 cm-thick lifts with the selected porous medium material. The top and bottom of each column was fitted with a stainless steel screen (75 µm) to contain the material, and ~1 cm thick layer of glass beads (0.2 mm, Fisher Scientific) to distribute flow. To achieve consistent initial unsaturated conditions, each column was first saturated bottom-up with Millipore water, and then suction-drained using a vacuum pump (MA-32, Gilson) set at -6.86 kPa (-70 cm of H_2O). To obtain saturated conditions, each dry-packed column was flushed with CO_2 gas for 2 hours, and then Millipore water was injected bottom-up for 10 hours at a flow rate of 0.1 mL/min. The initial water content (v/v) of each column was estimated through differential mass measurements before and after saturation, and following the applied vacuum multiplied by the column bulk density (mass of dry sediment/volume of packed column).

To explore the impact of initial moisture content, flow rate, sediment type, and NP dosing on the transport behaviour of Pluronic-coated NPs, six sets of experiments were performed (Table 2-1) using Fe-NPs coated with 10 g/L Pluronic (i.e, transport formulation). Although the primary focus was on the transport of NP under unsaturated conditions, NP transport was also investigated in a fully saturated system, and in an initially dry system to establish endpoint behaviour. In all column experiments, sodium bromide (NaBr) was added as a conservative tracer to the Fe-NP injection solution to reach a Br^- concentration between 100 and 200 mg/L. Results from preliminary transport experiments indicated that the presence of the NaBr did not affect NP transport behaviour. Each transport experiment involved a pulse injection of a specified volume of the NP and Br^- solution at the top of a column at a constant flowrate (0.14 mL/min) using a peristaltic pump (Cole Parmer, MasterFlex 7535-04). The duration of the pulse injection was approximately 70 or 320 minutes depending on the experimental set (Table 2-1). Following the pulse injection, the influent was immediately switched to Millipore water at the same flowrate until near complete breakthrough of the NPs was achieved (typically between 600 and 900 minutes). To ensure unsaturated conditions were maintained as the NP pulse migrated down the column, the maximum Darcy velocity (flowrate/cross-sectional area) used was less than the saturated hydraulic conductivity. The saturated hydraulic conductivity (0.43 ± 0.01 cm/min for the BS, and 0.16 ± 0.00 cm/min for the SSS) of a representative sediment packed column was estimated using a constant head test (ASTM 2434).

A low ([NP] = 50 mg/L), middle ([NP] = 500 mg/L) or high ([NP] = 1000 mg/L) target injection NP concentration (denoted as Set B1, B2, and B3 respectively) was used depending on the experimental set (Table 2-1). For the fully saturated system (Set A) and the initially dry system (Set C) [NP] = 500 mg/mL was used. To investigate the role of velocity, a lower flowrate (0.06 mL/min) with [NP] = 1000 mg/mL was employed (Set D) (Table 2-1). The NP binding batch test data (described below) indicated a higher NP mass attached to the SSS compared to the BS, and therefore a longer pulse duration (400 mins) in conjunction with the high injection NP concentration was selected for the transport experiments using SSS (Set E1). For comparison purposes, the identical higher NP dose was used for a column packed with BS (Set E2). Effluent samples were collected every 20 mins in 1.7 mL microcentrifuge Polypropylene vials (VWR, Mississauga, ON, Canada). The effluent volume was continuously recorded and used to estimate the effluent flowrate. Each experimental set was conducted at room temperature (22 ^{o}C) and performed in triplicate, except for Set E2 which was a control experiment for Set E1 and only one trial was performed. A total of 22 column experiments were executed.

The targeted binding of NPs towards a crude oil source zone present in an unsaturated system (Set F1) was explored using the CoFe-NPs with 2.5 g/L Pluronic coating (i.e., binding formulation). The CoFe-NPs were used in these transport and binding experiments to minimize the analytical interference caused by the background Fe present in the BS when estimating the mass of NPs attached to sediment sub-samples. Linley (2019) demonstrated that the NPs with either the Fe or CoFe core material (with the same coating formulation) behave similarly in porous media. To prepare the crude oil- impacted sediment to use for packing, dry BS was first moistened using Millipore water (~0.2 v/v), then mixed with crude oil (2 % wt) heated to 60 °C, and homogenized by stirring. A ~5 cm thick layer of the impacted BS was packed using

1-cm thick lifts in the middle of each column (from 5 to 10 cm from the bottom). Non-impacted moistened BS was packed below and above the impacted zone (see Figure 2-1). The flowrate and CoFe-NP input concentration were selected based on the results from the transport experiments (Table 2-1). Similar to the Fe-NP transport experiments, a pulse injection of the NP and Br^- solution at the top of a column at a constant flowrate (0.14 mL/min) was followed by Millipore water at the same flowrate until near complete breakthrough of the NPs was achieved. At the conclusion of this experiment, the packed sediment was carefully excavated in 1 cm lifts (from top to bottom), and the mass of CoFe-NPs retained in each lift was determined and used to generate a NP retention profile. As a control, a transport experiment (using Br^- and the CoFe-NP solution) was also conducted in a column uniformly packed with moist BS (~0.2 v/v) (Set F2). In total, 4 column experiments were performed at room temperature (22 ^{o}C); 3 trials in Set F1 and one trial in Set F2.

The NP mass that can be attached to clean or oil-impacted sediment ($M_{attached}$) was determined by batch binding tests (see A-1 for a description). For the Fe-NP transport formulation, values ranged from 7.8 ± 2.3 mg/kg for BS (Linley, 2019) to 37.3 ± 2.4 mg/kg for SSS, while for the CoFe-NP binding formulation values ranged from 8.2 ± 0.6 mg/kg for BS to 25.9 ± 2.1 mg/kg for NAPL-impacted BS (Table A-1).

2.2.3 Analyses

The NP concentration (mg/L) was estimated from the total iron or cobalt concentration (Fe_T, Co_T) in aqueous samples by assuming the core material was composed 100 % of Fe_3O_4 or $CoFe_2O_4$. To measure Fe_T or Co_T, an aliquot of the effluent sample was digested with HCl solution (37 %) to dissolve the NPs, then diluted by a factor of 10 with 0.1 mol/L HCl, and analysed using Inductively Coupled Plasma Optical Emission Spectrometry (ICP-OES; Teledyne Leeman Laboratories; method detection limit (MDL) of 0.004 mg/L for both Fe and Co). The concentration of bromide in each effluent sample was measured using ion chromatography (Dionex ICS-1100) with a MDL of 0.5 mg/L.

To estimate the mass of NPs retained in each sediment lift, EPA Method 3050b was used. Each lift was oven dried at 90 ^{o}C for 12 hrs to remove water, then homogenized before a 1 g sub-sample was transferred into a 50 mL digestion tube (VWR, Mississauga, Ontario). To digest the oil and NPs present in the sub-sample, 10 mL of concentrated HNO_3 (70 %) was added to each tube which was then heated at ~95 ^{o}C for 30 min. After cooling, 5 mL of concentrated HNO_3 (70 %) was added and the tube re-heated to 95 ^{o}C until the reaction was complete (indicated by lack of brown smoke) and the solution volume was reduced to ~5 mL. After the tube was cooled, 3 mL of H_2O_2 was added and gently heated at 85 to 90 ^{o}C until effervescence was observed. Once effervescence subsided, the tube was removed from the heating block and allowed to cool. When cooled, an additional 3 mL of H_2O_2 (30%) was added and the tube heated (95 ^oC) until effervescence was insignificant, and the solution volume was reduced to 5 mL. To ensure complete digestion of the NPs, 10 mL of concentrated HCl (37 %) was added and the tube was heated (95 ^oC) until the volume was reduced to 5 mL. The digestate was then diluted by Millipore water to a total volume of 10 mL and filtered (Whatman No. 41). The filtrate was analysed by ICP-OES to estimate Co_T which was used to calculate the mass of NPs in each sediment sub-sample (mg of CoFe-NPs per kg of dry sediment).

2.2.4 Modeling

2.2.4.1 Description

To simulate Br^- transport, and the NP transport and binding behaviour observed in the column experiments, a flexible one-dimensional unsaturated flow and transport model, 1DUSAT, was used (Thomson, 2019). In this model, the mixed form of Richards' equation (Celia et al., 1990) is used to estimate the unsaturated/saturated flow conditions in conjunction with the single-valued (non-hysteretic) capillary pressure - water saturation relationship, and relative permeability function developed by van Genuchten (1980). The numerical solution of the Richards' equation requires the knowledge of the porous medium hydraulic parameters including the residual water content, θ_r (m^3/m^3), van Genuchten model parameters (n (-) and α (1/m)), saturated hydraulic conductivity K_s (m/s), tortuosity factor l (-) for the hydraulic conductivity function and the total porosity, (ϕ_T) (m^3/m^3). The transport domain or total porosity (ϕ_T) is divided into a mobile region (ϕ_m) and an immobile region (ϕ_{im}) such that $\phi_T = \phi_m + \phi_{im}$, with the rate of mass exchange between these regions assumed to be first-order. Relevant to this investigation, 1DUSAT solves the following advection dispersion and reaction equations for the mobile region

$$\phi_m S_w^m \frac{\partial C_w^m}{\partial t} = \frac{\partial}{\partial z}\left(D \frac{\partial C_w^m}{\partial z} \right) - q \frac{\partial C_w^m}{\partial z} - \phi_m S_w^m \psi_c^m k_a C_w^m + \rho_b k_d f_s M_{attach}^m - \phi_m S_w^m \psi_{str} k_{str} C_w^m - \gamma (C_w^m - C_w^{im}) \qquad (1a)$$

$$f_s \rho_b \frac{dM_{attach}^m}{dt} = \phi_m S_w^m \psi_c^m k_a C_w^m - f_s \rho_b k_d M_{attach}^m \qquad (1b)$$

with the following reaction equations for the immobile region

$$\phi_{im} S_w^{im} \frac{\partial C_w^{im}}{\partial t} = +\gamma (C_w^m - C_w^{im}) - \phi_{im} S_w^{im} \psi_c^{im} k_a C_w^{im} + (1 - f_s) \rho_b k_d M_{attach}^{im} \qquad (2a)$$

$$(1 - f_s) \rho_b \frac{dM_{attach}^{im}}{dt} = \phi_{im} S_w^{im} \psi_c^{im} k_a C_w^{im} - (1 - f_s) \rho_b k_d M_{attach}^{im} \qquad (2b)$$

where m and im refers to mobile and immobile regions; S_w^m and S_w^{im} is water saturation (-); C_w^m and C_w^{im} are the aqueous Br$^-$ or NP concentrations, respectively (g/m^3); $D = \phi_m \tilde{D} = \alpha_L |q| + \phi \tau_w D_w^*$ is the dispersion coefficient (m^2/s); α_L is dispersivity (m); q is Darcy flux (m/s); D_w^* is the diffusion coefficient (m^2/s), τ_w (-) is the tortuosity factor; ψ_c^m and ψ_c^{im} are blocking coefficients (-); k_a and k_d are the attachment and detachment rate coefficients, respectively (1/s); ρ_b is the bulk density (kg/m^3); M_{attach}^m and M_{attach}^{im} is the mass attached to the sediment or crude oil- impacted sediment (g/kg); γ is the first-order mass exchange coefficient for Br$^-$ or NPs between the mobile and immobile regions (1/s); $\psi_{str} = (1 + x / d_{50})^{-\beta}$ is the straining blocking coefficient (-) which is used to account for depth-dependent retention of NPs (1/s); d_{50} is the mean grain diameter (m); x is distance from the column inlet (m); β is an empirical variable (-); k_{str} is the straining rate coefficient (1/s); and $f_s = \phi_m / \phi_T$ is the fraction of mobile water (-) assumed to be constant during transient flow conditions. To account for the saturation of NP attachment at retention sites, the following nonlinear Langmuirian relationship (Adamczyk et al., 1994) for the blocking coefficient, ψ_c, was used

$$\psi_c = 1 - M_{attach} / M_{attach}^{\max} \tag{3}$$

where $M_{attach}^{\max}$ is the maximum mass of NPs that can be attached to the sediment or oil- impacted sediment (mg/kg). To reduce complexity, the mass transfer rate of flow between the regions of mobile and immobile porosity was assumed to be sufficiently large so that S_w^m and S_w^{im} can be considered essentially equal (Šimůnek et al, 2008). Eqs (1) and (2) provide the mathematical framework to investigate the observed transport and binding of the NPs in both mobile and immobile regions. Linley et al. (2020b) demonstrated that the reversible kinetic attachment/detachment model employed in this model was able to represent the attachment behaviour of the Fe-NPs in saturated column systems.

2.2.4.2 Parametrization

To simulate the observed hydraulic behaviour for each column experiment, the saturated hydraulic conductivity, K_{sat}, was assigned the estimated values from hydraulic testing, and the remaining required hydraulic parameters including total porosity (ϕ_T), residual water saturation (S_{wr}), and the van Genuchten model parameters (n and α) were determined by calibration. In this study, the dynamically dimensioned search (DDS) optimization method (Tolson and Shoemaker, 2007) within the OSTRICH toolkit (Matott, 2017) was used as the calibration tool. The DDS method is a heuristic global search algorithm which overcomes common issues with other automatic calibration methods that find locally optimal solutions in the neighborhood of the initial solution (e.g., quasi-Newton method), or are relatively inefficient (e.g., shuffled complex evolution algorithm). The DDS optimization method initially searches globally across the calibration range provided for each parameter, and then becomes more local as it advances towards the specified number of total model evaluations. The observed column outflow data were used as calibration targets with a root mean square error (RMSE) objective function as the model calibration measure. To ensure that an optimal solution was obtained, three different calibration trials and 100 model evaluations were performed. For each calibration trial, a different initial parameter set was generated randomly from the calibration parameter range specified for each parameter to allow the DDS algorithm to initiate from a new starting solution. The parameter set from the calibration trial that generated the lowest RMSE was deemed optimal. Posterior residual analyses were also used to assess goodness of fit (R^2), and the randomness of the residuals (observed-simulated values) was evaluated using the Shapiro-Wilk normality test (Shapiro and Wilk, 1965).

For the suction-drained columns, an initial equilibrium pressure head and corresponding water saturation distribution was specified based on the measured value of the applied vacuum at the bottom of the column. For the initial conditions of the impacted columns, the average estimated water content was used to prescribe a pressure head at the bottom of the column using representative hydraulic parameters from the Fe-NP transport experiment simulations. This prescribed pressure was used to establish an initial hydrostatic pressure and water saturation profile. Transient boundary conditions for all unsaturated column systems (see Table 2-1) were identical with a free-exit condition assigned at the bottom, and a specified water flux assigned at the top of the column. For the saturated column simulations, constant water flux and constant pressure head boundary conditions were applied at the top and bottom of the column, respectively.

The initial Br^- and NP concentrations in the computational domain were assigned zero, and a total mass flux consistent with the duration of the injection pulse was specified as the top boundary condition, and a zero dispersive flux as the bottom boundary condition. The 15 cm long spatial domain was discretized into 1000 computational volumes, and an initial time step interval of 1.0 secs was used and allowed to increase by 0.02% until a maximum time step increment of 10 secs was reached. Based on preliminary simulations, the mass balance for water, Br^- and NPs were all < 0.07%.

Using the calibrated hydraulic parameters, column transport parameters (dispersivity (α_L), mobile porosity (ϕ_m), immobile porosity (ϕ_{im}), and first-order mass exchange coefficient (γ_{Br})) for Br^- were estimated. A similar calibration approach, as described above for the hydraulic parameters, was used in conjunction with the observed Br^- effluent data as the calibration target. The NP attachment/detachment and straining terms in Eqs (1) and (2) were not used in these Br^- simulations. Finally, using the calibrated hydraulic and transport parameters for each column, the NP transport and attachment parameters ($M_{attach}^{\max}$, k_a , k_d , γ_{NP}) were determined by calibration with the observed NP effluent data as the calibration target for all NP transport experiments (Table 2-1). The bulk density was assumed to be 1800 kg/m^3 (Ball et al., 1990) for all column systems. To account for minor variations between the batch binding tests and the column experiments, the calibration range for $M_{attach}^{\max}$ was constrained to the 95% confidence interval (CI) as determined from the binding batch tests (see Table A-1).

Based on preliminary simulations using the BTC data from the targeted binding experiment (Set F1 and F2) the straining term in Eq (1) was activated, introducing the straining rate coefficient (k_{str}) as an additional calibration parameter. For the targeted binding column simulations, the mean grain diameter (d_{50}) was assigned a value of 0.02 cm based on Figure A-2, and β was set to 0.432 as presented by Bradford et al. (2003).

2.3 Results and Discussion

2.3.1 Hydraulic Behaviour

The average observed flowrates were 0.13 ± 0.02 mL/min (n = 21) and 0.06 ± 0.01 mL/min (n = 3) closely matching the target flowrates of 0.14 and 0.06 mL/min of sets A to F2 and D, respectively (Table 2-1). For the target flowrate of 0.14 mL/min, flow started to appear at the column outlet between 85 and 122 mins for the BS suction-drained systems (Sets B1, B2, B3), between 75 and 95 mins for the SSS suction-drained system (Set E1), and between 95 and 135 mins for the impacted system (Set F1). For the target flowrate of 0.06 mL/min, flow appeared at the column outlet between 165 and 245 mins. In comparison, for the initially dry system (Set C), flow appeared at the column outlet later (between 265 and 285 mins) due to the lower initial water content. In all systems, the flow breakthrough profile reflecting the shape of the wetting front was sharp; increasing from essentially no flow to a near steady flowrate in 20 ± 5 mins (e.g., see Figure A-3).

The model was able to capture this sharp wetting front and provided flow behaviour representative of the observations ($R^2 > 0.93$) (Figure A-3). The normality of residuals was also confirmed ($p > 0.05$) (see Figure A-4 for example residual plots). The calibrated hydraulic parameters (ϕ_T , S_{wr}, n, and α) varied slightly between experiments due to minor differences in packing, giving rise to small changes in pore connectivity (see Table A-2). Hydraulic parameters for the initially dry column systems were not determined since the capillary pressure - water saturation relationship used in 1DUSAT is not appropriate for initially dry systems. For the BS packed columns (n = 18), the average calibrated ϕ_T, S_{wr}, n, and α were 0.33±0.05, 0.20±0.02, 1.28±0.08, and 14.93±0.19 (1/m), respectively, and for the SSS packed columns (n = 3) the average ϕ_T, S_{wr}, n, and α were 0.31±0.01, 0.19±0.01, 1.17±0.65, and 11.00±0.82 (1/m), respectively. The calibrated S_{wr} and ϕ_T values for both SSS and BS suction-drained column systems are similar, as expected, since SSS is comprised of 80% BS and 20% of the silty sand material. The estimated n values for the SSS and BS materials are also similar which is reflective of the near identical shape of the pore size distribution. The slightly larger estimated α value for BS compared to the SSS is reflective of the lower fraction of fine-grained particles (Figure A-2) and hence the ability to drain at a lower capillary pressure. Figure A-3 presents the observed and simulated effluent flow profiles for a suction-drained column packed with SSS from Set E1, and one packed with BS from Set E2. Consistent with the estimated hydraulic parameters, a similar flow profile shape was observed in these trials. Flow breakthrough at the column outlet occurred around the same time for both columns, indicating similar initial water content and pore size distribution. As can be observed in Figure A-3, the effluent flow profile from an impacted column (Set F1) and a control column (Set F2) have the same shape with nearly identical flow arrival at the column outlet indicating that the presence of the crude oil did not significantly alter flow behaviour.

2.3.2 Column Experiments

2.3.2.1 BTC observations

To facilitate comparison between the various BTCs generated, the Br^- and NP concentrations were normalized by the injection concentration (C_o), and the time axis was normalized by the time to the center of mass of the Br^- BTC (T_c^{Br}). Representative observed Br^- and Fe-NP BTCs from the saturated (Set A), suction-drained (Set B2), and initially dry (Set C) column experiments are shown in Figure 2-2 (see Figure A-5 for the BTCs from the remaining trials).

The shape of the Br^- BTCs from all experiments (except for the saturated columns, Set A) were asymmetrical with a characteristic steep increase to the peak concentration followed by a falling limb with a noticeable tail (Figure 2-2). Shortly after effluent breakthrough from the initially dry columns, the Br^- concentration increased rapidly to the peak concentration, while for the suction drained systems, the rising limb of the Br^- BTC began slightly after effluent breakthrough and then increased relatively slower than observed for Set C to the peak concertation. The higher degree of Br^- BTC tailing observed in initially dry columns compared to the suction-drained columns is indicative of greater diversity of flow pathways. In contrast, the Br^- BTCs from the saturated columns were symmetric confirming that the observed Br^- tail from the suction-drained and initially dry columns is related to the unsaturated conditions. Similar tracer behaviour has been reported by others (Akhtar et al., 2011; Padilla et al., 1999; Prédélus et al., 2017) and was attributed to the presence of either zones of immobile water (i.e., low velocity regions) or dead end pores leading to non-equilibrium physical transport (Gao et al., 2006; Kumahor et al., 2015b; Molnar et al., 2014; Torkzaban et al., 2006).

The shape of the observed Fe-NP BTCs from the initially dry and suction-drained systems were also asymmetrical (Figure 2-2). While, the Fe-NP BTCs from the saturated columns, similar to their respective Br^- BTCs, were symmetrical with a slightly lower normalized peak concentration compared to Br^-. In comparison to the suction-drained system, the Fe-NP BTCs from the initially dry systems had significantly lower peak concentrations, more tailing, and delayed arrival. This behaviour suggests an increase in retention sites for NP attachment possibly due to more air phase present and more gradual release of NPs from retention sites. BTC metrics for (Br^- and NPs) for all experimental sets are presented in Table 2-2.

The mass recovery of Br^- and Fe-NPs were estimated by integrating under their BTCs and normalizing by the total mass injected ($M_R = M_{out}/M_{in}$ x 100) (see Table 2-2). The recovery of Br^-, a conservative tracer, was ~100%, while Fe-NP recovery decreased from 83% in the saturated columns to 76% in the suction-drained columns, and to 25% in the initially dry columns. Consistent with the Fe-NP M_R estimates, the average retained mass of NPs per mass of solid (estimated from mass balance (*MB*)) ($C_{retained}^{MB}$) (Table 2-2) was significantly higher for the initially dry columns (18.6 ± 0.2 mg/kg) compared to the suction-drained (4.3 ±1.9 mg/kg) and saturated columns (3.4 mg/kg). The $C_{retained}^{MB}$ for the dry columns (Set C) is 2.4 times higher than the attachment capacity of Fe-NPs to BS as estimated from the batch binding tests under saturated conditions (7.8 ±2.3 mg/kg). This increased NP retention for the initially dry systems may be caused by Fe-NP attachment to AWI in addition to SWIs, as well as physical trapping in lower velocity regions (e.g., AWS interfaces and grain-grain junctions). The attachment of Fe-NPs to SWIs may occur due to van der Waals forces acting between the PEO block of the NPs Pluronic coating and the silica (SiO_2) on sediment surfaces (Linley et al., 2019), while capillary forces are mainly responsible for the Fe-NP attachment at the AWIs. These retention mechanisms produced Fe-NP BTCs that are significantly suppressed and delayed relative to their respective Br^- BTCs. In the initially dry and suction-drained columns, as the water content increased behind the wetting front, the extent of AWIs and the immobile regions decreased, and some of the Fe-NPs attached at these retention sites may have detached, producing a long Fe-NP BTC tail (Figure 2-2 (a,b)). These observations are consistent with the effect of AWIs on NP transport seen in the wider literature (Chen et al., 2008; Gao et al., 2006; Kumahor et al., 2015a; Shang et al., 2008; Torkzaban et al., 2008; Yecheskel et al., 2018). For example, Gao et al. (2006) suggested that during transient flow, a fraction of NPs in contact with immobile region AWIs are susceptible to release when these regions are reconnected with the mobile porosity. Similarly, Shang et al. (2008) observed mobilization of colloids (NPs) and their subsequent elution by a wetting front, indicating the importance of capillary forces on NP migration.

To quantify the delayed breakthrough of Fe-NPs compared to Br^-, the time to the center of mass of the Fe-NP BTC (T_c^{NP}) was divided by T_c^{Br} to calculate an arrival time ratio (T_c^{NP}/ T_c^{Br}) (Table 2-2). The arrival of the center of mass of the Fe-NPs BTCs was significantly delayed with respect to Br^- for the initially dry columns compared to the saturated and suction-drained columns (i.e., T_c^{NP}/ T_c^{Br} of 1.22 compared to 1.00 for Set A, and 1.01 for Set B2). The near simultaneous arrival of the center of mass of the Fe-NPs and Br^- BTCs in most experimental sets, as well as a delayed arrival of Fe-NPs in other sets (i.e., Set C and Set E1) (Table 2-2) indicate that size exclusion did not occur in any of the systems investigated (Bradford et al., 2003; Prédélus et al. 2014, 2017; Sirivithayapakorn and Keller, 2003).

Figure 2-3 shows BTC data for suction-drained BS systems at low (0.06 mL/min; D) and high (0.14 mL/min; B3) flowrates. No substantial difference is observed between the shapes of these BTCs except for a slightly lower peak concentration and less tailing at the lower flow rate. Breakthrough of Fe-NPs and Br^- occurred around the same normalized time (t/T_c^{Br}), and both sets had the same the arrival time ratio (T_c^{NP}/T_c^{Br} of 1.01±0.01 for Set B3, and 1.00±0.01 for Set D). The M_R of Fe-NPs (Table 2-2) for the lower and higher flowrate sets were 76 ± 7% and 91 ± 5 %, respectively, due to an increase in both residence time and air phase in the lower flowrate columns. Chen et al. (2008) demonstrated that a slow flowrates resulted in a higher retention of NPs due to the longer residence time for NPs (TiO_2) to attach to AWIs. Shang et al. (2008) observed decreased colloid (NP) mass recovery under lower velocity conditions (0.288 to 0.018 cm/min) and related this behaviour to an increase in the AWI. Kumahor et al (2015a) investigated silver NP transport in unsaturated columns subjected to three flow rates (i.e., 2.5, 9.7 and 17.0 cm/h) and observed increased mobility with increased flowrate. Consistent with the results from experimental Sets B1, B2 and B3, the lower flow rate corresponds to a larger AWI and higher NP retention.

Representative Br^- and Fe-NP BTCs for suction-drained BS systems at three different Fe-NP injection concentrations (50 mg/L, B1; 500 mg/L, B2; 1000 mg/L, B3) are shown in Figure 2-4. All BTCs had similar asymmetrical profiles with a center of mass arrival time ratio of ~1 (Table 2-2). As expected, the Fe-NP peak concentration (C/C_0) increased with a higher injection concentration from an average of 0.48 (B1) to 0.57 (B2) and 0.61 (B3), consistent with the decreasing mass recovery (average M_R = 53% for B1, 76 ± 5% for B2, and 91 ± 5% for B3). This is consistent with other literature findings, for example, mass recovery increased with injection dosage for TiO_2 NPs in saturated columns and was attributed to particle-particle repulsion (Chowdhury et al., 2011). When NPs are attached to sand grains (i.e., SWIs), they can form a shield of NPs on the surface where unfavorable particle–particle interactions limit further NP attachment.

At higher dosages, more NPs occupy attachment sites and particle–particle repulsion dominates, leading to higher elution of NPs. High NP concentrations can also decrease mass recovery due to agglomeration (Phenrat et al., 2010; Raychoudhury et al., 2012) or attractive interactions (e.g. electrostatic forces) between the attached and suspended NPs (Liu et al., 1995); however, in this work the Pluronic NP coating establishes a neutral charge and, for the concentrations range investigated, NP agglomeration is hindered by steric interactions.

Figure 2-5 compares representative BTCs from SSS packed columns (E1) and BS packed columns (E2). In contrast to the BTCs from the other suction-drained experiments with a lower injection volume or dose, the BTCs for both Set E1 and Set E2 reached a plateau peak concentration of $C/C_0 = 1$. The Fe-NP and Br^- BTCs from the BS column essentially overlap ($T_c^{NP}/ T_c^{Br} = 1.00$), while the Fe-NP BTC for the SSS column was delayed with $T_c^{NP}/ T_c^{Br} = 1.09$ (Table 2-2), leading to an average M_R of 65 ± 1% and 96% for SSS and BS columns, respectively. The addition of 20% of the silty sand material in the SSS compared to BS had a significant impact on NP transport and retention behaviour. The average $C_{retained}^{MB}$ was 65 ± 1 mg/kg for the SSS packed columns which is significantly higher than the average $C_{retained}^{MB}$ of 6.4 mg/kg for the BS columns and the estimated attachment capacity of Fe-NPs to SSS sediment in binding batch tests ($M_{attached}$ = 37.3 ± 2.4 mg/kg; Table A-1). This increased NP retention in the column system is likely due to the presence of AWIs that would not be encountered in the batch test. Previous work that evaluated the effect of porous medium texture on NP transport has reported both a lower mass recovery and peak concentration with decreasing grain size (Fang et al., 2009; Kamrani et al., 2018; Liang et al., 2013b). In contrast, for the Fe-NPs used in this study the breakthrough front (Figure 2-5(a)) was essentially delayed until all attachment sites were saturated and then the concentration increased to $C/C_0 = 1$, similar to observations reported by Torkzaban et al. (2010) and Wang et al. (2014).

To evaluate the targeted binding capability and transport of the CoFe-NPs under unsaturated conditions, experimental parameters (BS, flowrate of 0.14 mL/min, NP injection concentration of 500 mg/L) were selected based on the findings from the Fe-NP transport experiments. In addition, an injection pulse of 20 mL (Table 2-1) (high input dosage) was used to ensure sufficient CoFe-NP mass was observed in the effluent since the batch binding test results indicated a higher attachment capacity to clean and crude oil-impacted BS as compared to Fe-NPs (Table A-1).

Representative Br^- and CoFe-NP BTCs for the crude oil-impacted (Set F1) and control (Set F2) columns are shown in Figure 2-6. The Br^- BTCs shape was similar for both experimental sets with a slightly lower T_c^{Br} for the crude oil-impacted column, likely due to minor packing variations and presence of the crude oil. In both column sets, the CoFe-NP BTCs were delayed relative to their respective Br^- BTCs, and had lower peak concentrations. Both of these features were more pronounced in the crude oil-impacted columns compared to the control columns; the average T_c^{NP}/T_c^{Br} was 1.22 ± 0.04 with M_R = 26 ± 3% for the oil-impacted columns and 1.05 with M_R = 49% for the control column (Table 2-2). Consistent with these values, the retained mass of CoFe-NPs per mass of solid, $C_{retained}^{MB}$, is twice as high in the oil-impacted columns compared to the control column (33.0 ± 2.0 vs 15.0 mg/kg). The increase in the mass of CoFe-NPs retained and the delay in arrival of the BTCs for the oil-impacted columns reflects the ability of the CoFe-NPs to preferentially bind to the crude oil under unsaturated conditions.

The distribution of CoFe-NPs retained along the oil-impacted columns (using the solid digestion and ICP-OES method) are presented in Figure 2-7 for the two trials of Set F1. These profiles clearly show a higher concentration of CoFe-NPs retained in the crude oil zone (27 to 35 mg/kg) compared to the lower non-impacted zone (0 to 0.05 m) of the columns (8 to 18 mg/kg). In the non-impacted zone, adsorptive interactions between PEO and the surface of the sand grains, as well as capillary forces at AWIs contribute to nanoparticle attachment. Additionally, hydrophobic forces (stronger due to the lower Pluronic coating concentration on the CoFe-NPs) between the CoFe-NP and the air phase may increase retention compared to Fe-NPs which saw $C_{retained}^{MB}$ between 4 and 6 mg/kg in suction drained BS packed columns. These hydrophobic interactions are also responsible for CoFe-NP attachment to the crude oil-impacted zone. In the non-impacted zone above the oil (0.10 to 0.15 m), the concentration of CoFe-NPs ranged from 19 to 32 mg/kg for the first trial of Set F1, and 15 to 28 mg/kg for the second trial with a distribution suggestive of depth-dependent straining.

These retention mechanisms decreased CoFe-NP transport compared to the Fe-NPs as demonstrated by the lower M_R (49% vs 91 ± 5%) and $C_{retained}^{MB}$ (15.0 vs 4.3 ± 0.6 mg/kg) for Sets F2 and B3, respectively, under nearly identical conditions (i.e, same flowrate, input dosage, aquifer material). This is also manifested as a decreased peak concentration and delayed arrival of CoFe-NPs with respect to Fe-NPs (Figure A-6).

2.3.2.2 Model simulations

The asymmetrical shape of the Br^- BTCs, indicative of physical non-equilibrium transport, was captured by the model (Eqs. (1) and (2) without the attachment/detachment and straining terms) with $R^2 > 0.95$ (see Figures 2 to 6). Attempts to fit the Br^- BTCs from all the suction-drained columns considering a single porosity system ($f_s = 1$) were unable to replicate the significant observed tail. In contrast, since no tailing was observed in the Br^- BTCs from the saturated columns (Set A), the model was able to produce a good fit ($R^2 = 0.99$) by considering a single porosity system (Figure 2-2(c)) (see Figure A-4 for example residual plots). A summary of the calibrated Br^- transport parameters for each experimental set is provided in Table 2-3 (See A-2 for explanations).

We assumed that the NP transport and attachment/detachment parameters were identical in both the mobile and immobile porosity regions because the sediments were homogenized prior to packing the columns. A range of values for the ratio of the NP diameter to the mean grain diameter (d_p/d_{50}) has been suggested from 0.002 (Bradford et al., 2002) to 0.154 (Herzig et al., 1970) as the threshold when physical straining is dominant. For the Fe-NPs (d_p: 7.6 x 10^{-6} mm) and porous media (d_{50}: BS = 0.18 mm, SSS = 0.14 mm) employed in this study, this ratio is < 0.002, and thus the straining term was not used for simulations of the Fe-NP transport experiments. Acceptable fits to the observed Fe-NP BTCs ($R^2 > 0.92$) were obtained, and residuals were normally distributed ($p > 0.05$). Selected simulated Fe-NP BTCs are shown on Figures 2 to 5. Attempts to fit the observed CoFe-NP BTCs from the impacted and control columns using the model components employed for the simulation of Fe-NP BTCs were unable to reproduce the peak concentrations. As noted above, the CoFe-NP retention profiles for Set F1 (Figure 2-7) above the crude oil zone (0.10 to 0.15 m) appear to follow an exponential shape characteristic of depth-dependant straining, likely due to aggregation from the lower Pluronic coating concentration on the CoFe-NPs (Figure A-1). The lower Pluronic coating concentration used for the CoFe-NPs (2.5 vs 10 g/L P104), makes them more susceptible to aggregate as a result of insufficient Pluronic to completely saturate the surface of individual particles (Figure A-1). With the inclusion of depth-dependent straining, the simulation was able to reproduce the CoFe-NP BTCs (Figure 2-6, $R^2 > 0.95$; residuals normally distributed ($p > 0.05$)), and the retention profile (Figure 2-7, $R^2 > 0.83$; residuals normally distributed ($p > 0.05$)). The calibrated straining rate coefficient, k_{str} ($3.0 \pm 0.6 \, x10^{-4}$ /s) is similar to the value reported by Linley et al. (2021) for same CoFe-NPs (and same coating formulation) in saturated conditions (see A.3). Table 2-3 lists the calibrated parameters. While evidence of straining was observed in the NP binding experiment, and addressed by a depth-dependent straining term in the model, a mechanistic investigation into f this retention behavior was not within the scope of this research.

For all the suction-drained and saturated column systems, except for Set E1, the optimal $M_{attach}^{\max}$ was within the 95% CI of the NP attachment capacity as estimated from the batch binding tests. In general, the calibrated $M_{attach}^{\max}$ value was slightly higher than the average observed $C_{Retained}^{MB}$ values (Table 2-2) depending on the injected dose of the Fe-NPs. To achieve an acceptable calibration of the observed BTCs from the suction-drained columns packed with SSS (Set E1), the upper bound of the calibration range for $M_{attach}^{\max}$ was increased. The average calibrated value was 65.4 ± 0.3 mg/kg, which was consistent with the observed mass of retained Fe-NPs ($C_{Retained}^{MB}$ = 65.2 ± 4.4 mg/kg), and almost twice the estimated attachment capacity from the batch binding tests (Table A-1). The need for a higher $M_{attach}^{\max}$ value indicates that additional or enhanced NP attachment mechanisms were occurring during the migration of Fe-NPs through the SSS packed systems that were not captured by the batch binding test. Treumann et al. (2014) explored differences in NP attachment mechanisms between batch and saturated column studies, and speculated on the role of a variety of forces acting on the NPs during their transport in column systems including hydrodynamic drag and lift, electrical double-layer repulsion (or attraction), and London–van der Waals interaction.

The calibrated first-order mass transfer rate coefficient for the Fe-NPs ($\gamma_{\text{Fe-NP}}$) varied slightly (1 x 10^{-5} to 4 x 10^{-5} /s) except for experimental Set D where the calibrated value was an order of magnitude smaller (6 x 10^{-6} /s), due to the lower injection flow rate. The calibrated $\gamma_{\text{Fe-NP}}$ values are consistent with the observation noted above for γ_{Br} . Prédélus et al. (2014) also found that the mass transfer rate coefficient for NPs and tracer between mobile and immobile regions was on the same order magnitude (2 x 10^{-4} to 9 x 10^{-4} /s for NP vs ~3.4 x 10^{-4} /s for tracer).

The calibrated attachment rate coefficient, k_a, for all column systems packed with BS varied over a narrow range (from 1 x 10^{-5} to 5 x 10^{-5} /s). The presence of additional retention sites (i.e., AWIs) in the suction-drained columns (Set B2) compared to the saturated experimental Set A did not have a statistically significant impact on k_a (5.1 x 10^{-5}/s for Set B3 vs 1.6 x 10^{-5}/s for Set A) ($p > 0.05$). Conversely, the calibrated detachment rate coefficient, k_d, was found statistically different between the two sets; for Set B2 it was an order of magnitude larger than k_d for Set A (6.0 x 10^{-7} vs 7.5 x 10^{-6} /s) which manifests as a longer tail in the Fe-NPs BTCs. This is attributed to the gradual release of NPs from the additional retention sites (i.e., AWIs) in the drained columns (Set B2) due to the gradual decrease in the air-water interfacial area during transient flow conditions (Sirivithayapakorn and Keller, 2003). It has been reported that NPs usually attach to AWIs irreversibly by capillary forces (Bradford et al., 2003; Flury et al., 2017) until the dissolution of trapped air behind the wetting front occurs (Sirivithayapakorn and Keller, 2003).

No significant difference in the calibrated k_a was attained for the three experimental systems that were used to investigate the impact of dosing or concentration on Fe-NP transport (Set B1, Set B2 and Set B3) (Figure 2-4); however, k_d slightly increased with higher dosing (from 3.0 to 7.5 to 9.1 x 10^{-6} /s for Set B1, B2 and B3 respectively, $p < 0.05$). The increase in k_d in response to the higher injection dosing is likely due to increased particle-particle collision between those in the bulk solution and those attached, and their subsequent remobilization. Collectively, based on the observed BTCs and the calibrated parameters, it appears that for the range of input concentrations investigated (50 to 1000 mg/L), there was no significant impact of concentration on the transport behaviour of the Fe-NPs used.

For Set D (lower flow rate), k_a is nearly identical to that determined for Set B3 ($1.50 \pm 0.8 \times 10^{-5}$ /s compared to $1.91 \pm 0.43 \times 10^{-5}$ /s), while the average k_d is about 36 times smaller ($2.5 \pm 0.8 \times 10^{-7}$ /s compared to $9.1 \pm 0.4 \times 10^{-6}$ /s) which is suggestive of a relative decrease in detachment. The decreased connectivity between the mobile and immobile regions indicated by an order of magnitude lower $\gamma_{\text{Fe-NP}}$ is also responsible. It has been reported that the primary retention mechanism of NPs at AWIs is capillary forces during steady or low flow rates (Wan and Wilson, 1994) where the remobilization of retained NPs are found to be very slow or negligible, and thus the attachment of NPs at AWIs can be considered irreversible. Any changes in the flow rate may alter the retention of NPs by affecting kinetics (i.e., k_a or k_d) (Torkzaban et al., 2008). Liang et al. (2013b) and Makselon et al. (2016) suggested that the rate of NP attachment increased (higher k_a) while k_d decreased or became negligible with lower flow rates indicating irreversible attachment.

For the columns packed with the SSS material (Set E1), the average calibrated k_a was an order of magnitude larger than the column systems packed with BS ($4.0 \pm 1.03 \times 10^{-4}$ /s vs 1×10^{-5} to 5×10^{-5} /s), while the calibrated k_d was ~8 times smaller than the BS packed systems (Table 2-3), suggesting a significant increase in attachment to, and decrease in detachment from, the SSS material. The increased k_a in combination with a larger $M_{attach}^{\max}$ manifested into the delayed arrival of the Fe-NPs BTC (Figure 2-5) as a result of the increased clay and silt content (larger surface area) and thus more NP retention sites. An increase in k_a with decreasing grain size was reported by Liang et al. (2013b) who observed a higher mass of silver NPs retained in columns packed with smaller sized sand and concluded that the higher k_a represented increased mass transfer to the grain surfaces as a result of the larger surface area. It has been proposed that straining becomes the dominant retention mechanism as the average grain size decreases (Raychoudhury et al. 2014; Hoggan et al. 2016; Fang et al. 2013b Kamrani et al. 2018); however, in the case of the Fe-NPs, straining was unlikely as previously described. In contrast, Jung et al. (2014) reported reduced retention of surface-modified nZVI in sand columns with increased clay content (2% by weight) as a result of increased electrosteric repulsion between the clay minerals and the negative surface charge of the modified nZVI.

The calibrated $M_{attach}^{\max}$, was ~3 times higher for the crude oil zone in the oil-impacted columns (26.4 ± 1.2 mg/kg) compared to the control column (7.8 mg/kg) and the upper and lower clean zones within the impacted column (8.2 ± 1.3 mg/kg). The calibrated attachment rate coefficient, k_a, for the crude oil zone ($2.8 \pm 0.15 \times 10^{-2}$/s) was two-orders of magnitude greater than k_a for the clean sand zones in the oil-impacted and the control columns (2.4×10^{-4} and $2.7 \pm 1.2 \times 10^{-4}$ /s). In contrast, the calibrated detachment rate coefficient, k_d, for the crude oil zone and the clean zones of the oil-impacted columns (Set F1) as well as the control column (Set F2) were essentially the same (values varied from 4.8 ± 1.1 x 10^{-6} to 7.6 ± 1.1 x 10^{-6}/s). The significantly larger attachment capacity ($M_{attach}^{\max}$) and rate coefficient (k_{a}) determined for the crude oil zone is a direct result of the hydrophobic forces between the amphiphilic NP coating and crude oil (compared to non-impacted zones).

Comparing the estimated parameters for the Fe-NPs in Set B3 with CoFe-NPs in Set F2 under nearly identical conditions, the estimated k_a for the CoFe-NPs in control column was about an order of magnitude higher than k_a for Fe-NPs in Set B3 (24 x 10^{-5} vs 1.9 ± 0.4 x 10^{-5}/s), while the estimated $M_{attach}^{\max}$ and k_d were nearly equal for both sets. The higher ratio of k_a to k_d for the CoFe-NPs in unsaturated columns compared to Fe-NPs in drained columns is consistent with the lower recovered mass of CoFe-NPs from the control column (F2).

2.4 Summary and Implications

A series of unsaturated column experiments investigated the role of initial water saturation, porous medium texture, input dosage, and flowrate on the transport of amphiphilic co-polymer coated iron oxide NPs (Fe-NPs). While the focus was on the transport behaviour of the Fe-NPs in unsaturated porous media, experiments in saturated and initially dry systems provided endpoint controls to contextualize the results which showed Fe-NP transport was affected by the initial water content of the column. Under near identical Fe-NP injection conditions, 83 % of the Fe-NP mass injected was eluted from the saturated columns, while ~25 % was eluted from the initially dry columns and ~76 % from the suction-drained columns. The Fe-NP and Br^- BTCs (co-injected conservative tracer) from the saturated columns were symmetric, while, for the suction-drained columns, both the Fe-NP and Br^- BTCs had an asymmetrical shape with a noticeable tail indicative of physical non-equilibrium transport. The Fe-NP BTCs were also dampened relative to the Br^- BTCs with lower normalized peak concentrations compared to those from the saturated columns. A higher degree of Br^- BTC tailing was observed for the initially dry columns indicative of a greater diversity of flow paths compared to the suction-drained columns. Additionally, the Fe-NP BTCs showed significantly lower peak concentrations, a higher degree of tailing, and delayed arrival of the center of mass (relative to their respective Br^- BTCs) compared to those from the suction-drained columns. The changes in Fe-NPs transport behaviour from saturated to suction-drained and then to initially dry conditions are reflective of an increase in Fe-NP retention sites due to a decrease in water saturation with concomitant increase in the magnitude of AWIs. Behind the wetting front, the quantity of AWIs is expected to gradually decrease as the water saturation increases and some attached Fe-NPs are slowly released which manifests as a long tail in NP BTCs.

The asymmetrical shape of the Br^- and Fe-NP BTCs from the suction-drained systems were successfully described using a model that considered Br^- and Fe-NP transport in mobile and immobile regions. In contrast, a single porosity system was sufficient to characterize the observed BTCs in saturated columns. A simple attachment/detachment model with nonlinear Langmuirian blocking was used to represent Fe-NP retention and release. The presence of additional retention sites (i.e., AWIs) in the suction-drained columns compared to the saturated columns did not have a significant impact on the Fe-NP attachment rate coefficient (k_a); however, the detachment rate coefficient (k_d) was found to be an order of magnitude smaller for the saturated columns compared to the suction-drained columns. A combination of the mass transfer of Fe-NPs between the immobile and mobile regions, as well as the gradual detachment from the retention sites (SWIs and AWIs) was responsible for a longer observed tail of the Fe-NP BTCs for the suction drained columns compared to the saturated ones. The slow detachment of NPs from AWIs is expected under transient flow conditions due to the gradual decrease in the air-water interfacial area and the extent of immobile regions.

A lower recovered mass of Fe-NPs from the columns with a lower flow rate (76 vs 91%) was attributed to an increase in the residence time and decrease in water saturation. The estimated k_a was nearly identical at both flow rates, while the k_d was 36 times smaller at the lower flow rate. The significantly smaller k_d compared to k_a at lower flowrate represents a relative lower rate of detachment and consistent with the lower recovered mass of NPs. For the range of injection concentrations investigated (50 to 1000 mg/L) no substantial impact was observed on Fe-NP transport behaviour. It was also observed that for the columns packed with higher clay and silt content sediments more Fe-NP retention (larger $M_{attach}^{\max}$ and k_a) occurred resulting in a significant delayed arrival of the Fe-NP BTC with respect to Br^-, which was attributed to the larger surface area. The estimated $M_{attach}^{\max}$ for the SSS packed columns was twice the value determined by the binding batch tests, clearly indicating that additional NP attachment mechanisms occurred during the transport of Fe-NPs through these sediments that were not captured in the binding batch test.

The capability of targeted binding of CoFe-NPs coated with a lower concentration of a Pluronic block co-polymer to crude oil present in an unsaturated system was investigated. Under identical CoFe-NP injection conditions, 49 % of the CoFe-NP mass injected was recovered from the non-impacted control column, while only ~26 % was recovered from the oil-impacted columns. The CoFe-NP BTCs from the impacted columns exhibited lower peak concentrations and significantly delayed arrival of the center of mass relative to the respective Br^- BTCs and those from the control column. Both the simulated CoFe-NP BTCs and CoFe-NP retention profile compared well with the observed data when a depth-dependant straining term in the model was used. This added simulation requirement is a result of a combination of increased retention of CoFe-NPs (capillary and/or hydrophobic forces) at the AWIs, and aggregation due to the lower Pluronic coating concentration and larger size compared to Fe-NPs. The $M_{attach}^{\max}$ for the crude oil zone was ~3 times higher than that for the surrounding non-impacted zones as well as the control column. The estimated k_a was about two-orders of magnitude higher for the crude oil zone than the k_a for the non-impacted zones and control column; however, the estimated k_d was nearly identical. The significant higher ratio of k_a to k_d in the crude oil zone compared to non-impacted zone is indicative of stronger attachment of CoFe-NPs to the crude oil.

These findings extend our understanding of the transport and binding behaviour of Pluronic-coated NPs from saturated to unsaturated systems where the presence of an air phase significantly impacts NP transport. Specifically, the additional retention processes in unsaturated porous media such as NP attachment at the air-water interface and low velocity regions (air-water-solid interfaces) add more complexities to transport and retention mechanisms than in similar saturated porous media. Findings established the significant role of initial water content, injection flow rate, and porous medium texture on NP transport and retention behaviour. This study also confirmed targeted delivery of Pluronic-coated NPs to crude oil-impacted porous media in unsaturated column systems which was previously only understood in saturated conditions (Linley 2019), broadening the potential of this technique. Finally, our simulation effort indicated that models that considered NP transport in both mobile and immobile flow regions could better reproduce NP physical and chemical non-equilibrium transport in unsaturated systems than the conventional single-porosity models. This study has clarified the influence of porous medium and injection parameters on the transport polymer-coated engineered NPs as well as the modelling approaches that should be taken to ensure better prediction of NP behaviour. Hence, these parameters and approaches should be considered when designing NP delivery strategies in natural porous media, enabling optimal NP utilisation in future monitoring or remediation technologies.

2.5 Acknowledgements

Funding for this research was provided by Chevron Energy Technology Company. We thank Felipe Solano, Shirley Chatten, Terry Ridgway, Mark Sobon and Mark Merlau for their technical assistance. Stuart Linley would like to thank the NSERC Postdoctoral Fellowship for supporting his work. We also acknowledge the Canadian Centre for Electron Microscopy for providing the TEM images of CoFe-NPs.

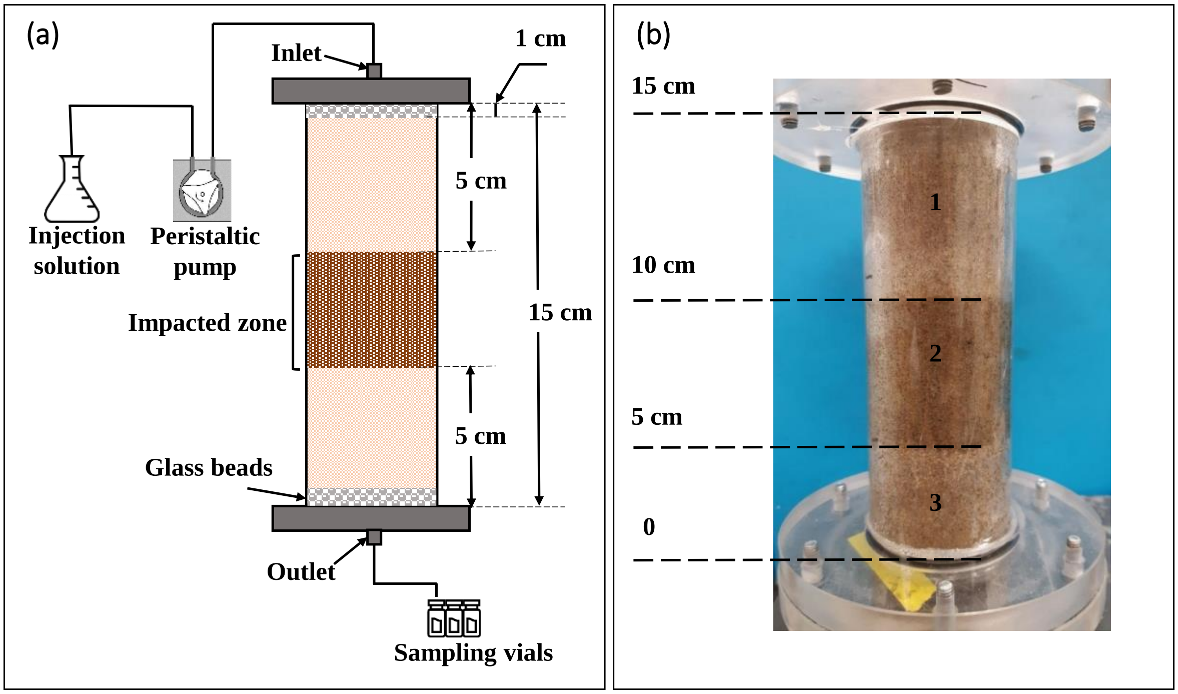

Figure 2-1. (a) Schematic of general column set-up, and (b) image of an oil-impacted column (Zones 1 and 3 are clean sand, Zone 2 is crude oil-impacted sand for the binding experiment). Not to scale. Flow was from top to bottom.

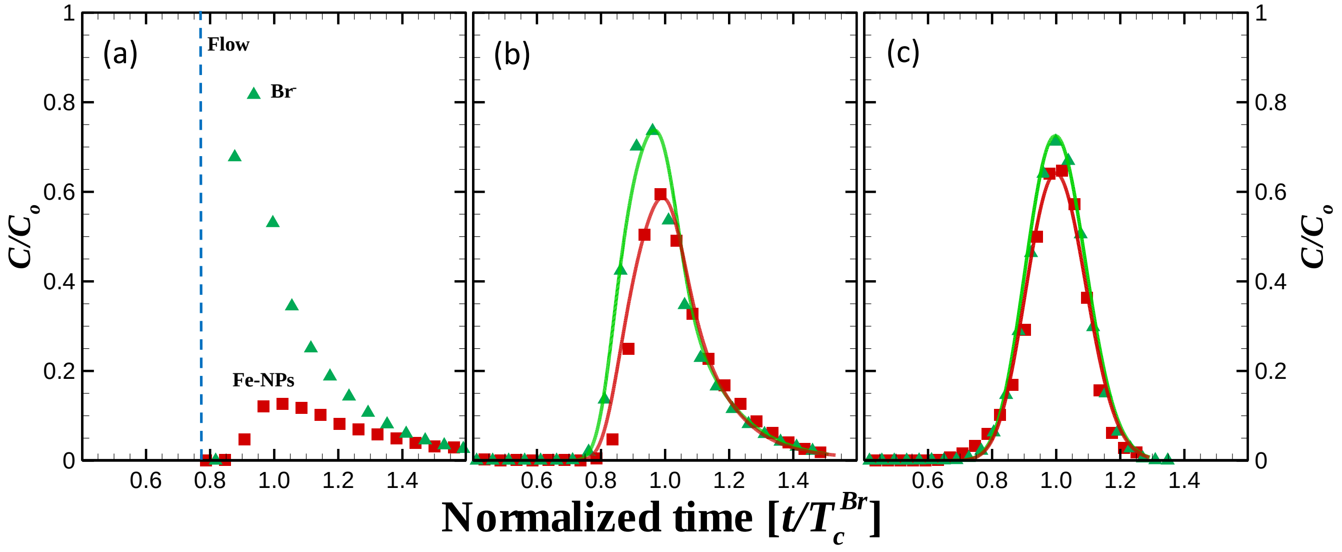

Figure 2-2. Observed (symbols) and simulated (solid lines) normalized BTCs of Br$^-$ (green) and Fe-NPs (red) for a representative (a) initially dry (Set C), (b) suction-drained (Set B2), and (c) saturated (Set A) column experiment. The time axis is normalized by the time to the center of mass of the Br$^-$ BTC (T_c^{Br}). Injection Fe-NP concentration of 500 mg/L (dosage of 5.0 mg), and flow rate of 0.14 mL/min were used. Also, indicated by the dashed line on (a) is when flow first appeared at the column outlet.

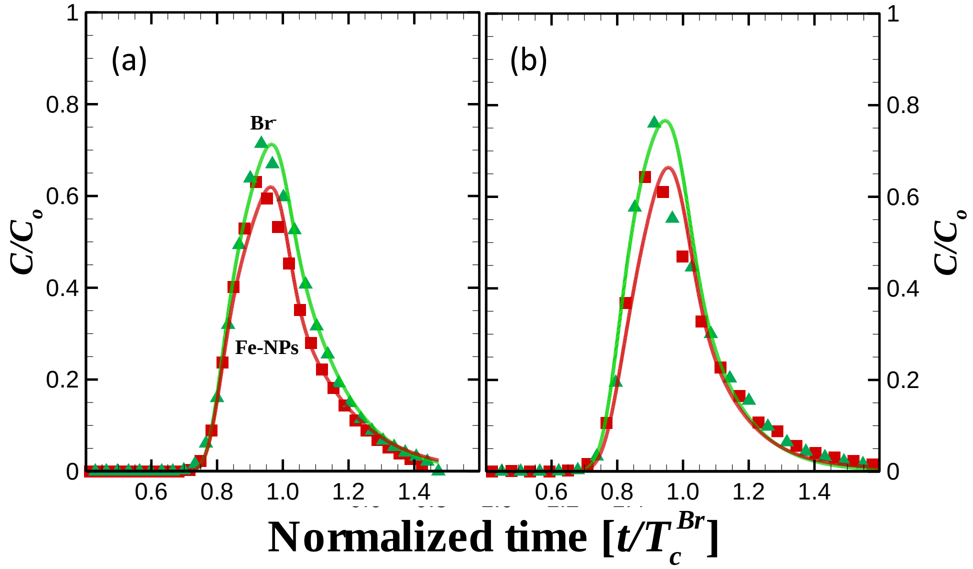

Figure 2-3. Observed (symbols) and simulated (solid lines) normalized BTCs of Br$^-$ and Fe-NP for suction-drained columns for an injection flowrate of (a) 0.06 mL/min (Set D), and (b) 0.14 mL/min (Set B3). The time axis is normalized by the time to the center of mass of the Br$^-$ BTC (T_c^{Br}). Injection Fe-NP concentration of 1000 mg/L (dosage of 10 mg) was used.

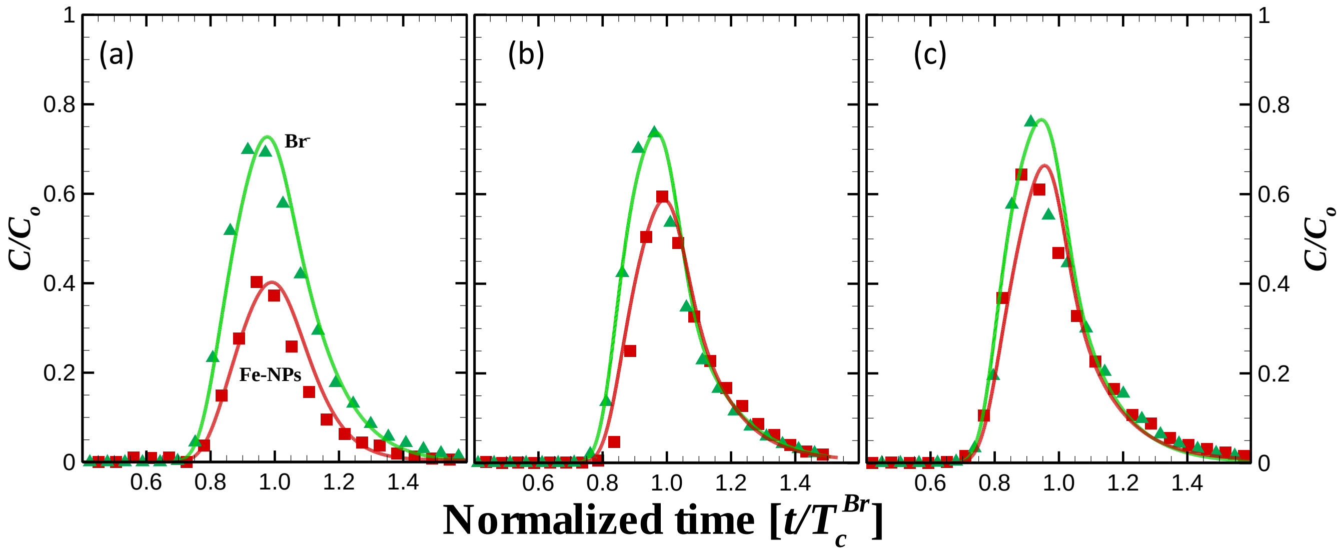

Figure 2-4. Observed (symbols) and simulated (solid lines) normalized BTCs of Br$^-$ and Fe-NP for suction-drained columns subjected to different input NP dosages (a) 0.5 (Set B1), (b) 5 (Set B2), and (c) 10 mg (Set B3) of Fe-NPs. Injection Fe-NP concentration of 50, 500, and 1000 were used respectively for (a) to (c). The time axis is normalized by the time to the center of mass of the Br$^-$ BTC (T_c^{Br}). Injection flow rate of 0.14 mL/min was used.

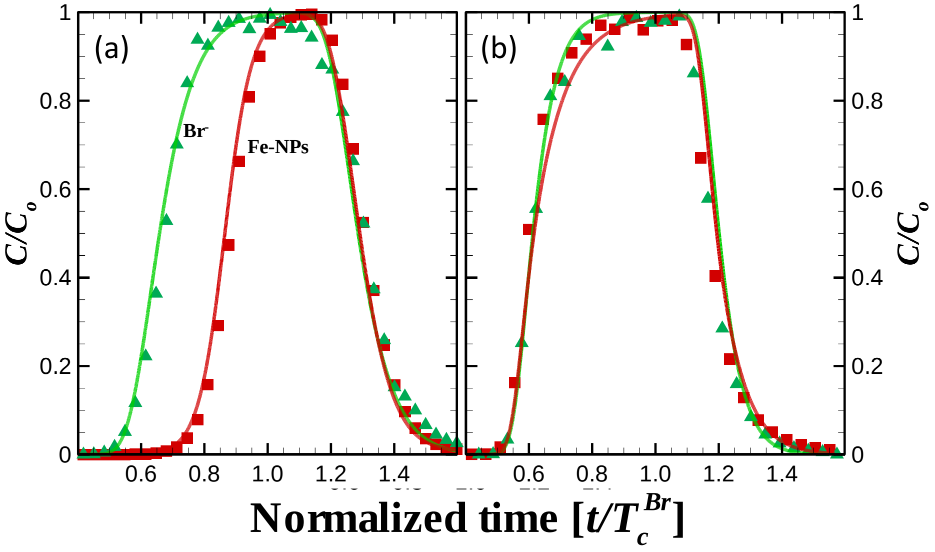

Figure 2-5. Observed (symbols) and simulated (solid lines) normalized BTCs of Br$^-$ and Fe-NPs for suction-drained columns packed with (a) SSS (Set E1) and (b) BS (Set E2) materials. The time axis is normalized by the time to the center of mass of the Br$^-$ BTC (T_c^{Br}). Injection flowrate of 0.14 mL/min and Fe-NP concentration of 1000 mg/L (dosage of 45 mg) were used.

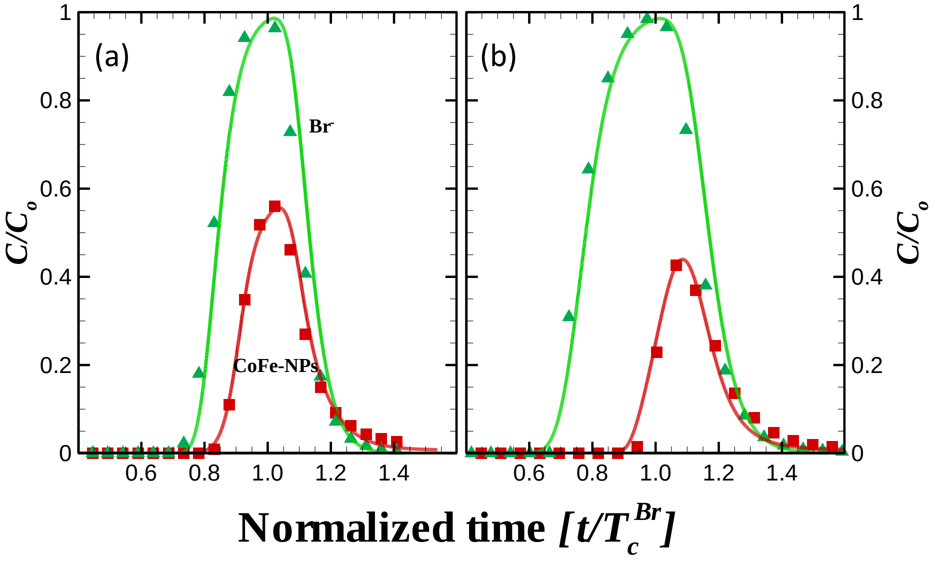

Figure 2-6. Observed (symbols) and simulated (solid lines) normalized BTCs of Br$^-$ and CoFe-NPs for unsaturated (a) non-impacted column (Set F2; Control) and (b) crude oil-impacted columns (Set F1). The time axis is normalized by the time to the center of mass of the Br$^-$ BTC (T_c^{Br}). Injection CoFe-NPs concentration of 500 mg/L (dosage of 10 mg/L) and injection flowrate of 0.14 mL/min were used.

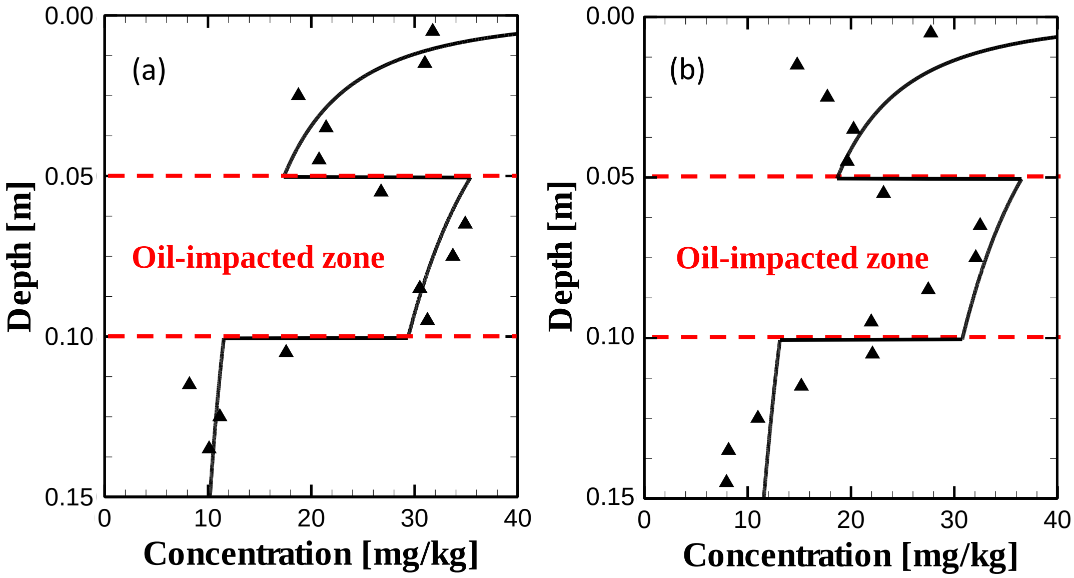

Figure 2-7. Observed (symbols) and simulated (solid line) CoFe-NP retained concentration profiles from the crude oil-impacted columns (a) Replicate 1, and (b) Replicate 2. The oil-impacted zone was located between 0.05 and 0.10 m from the base of the column, and the remainder of the column was packed with clean sand. Injection CoFe-NP concentration of 500 mg/L (input dosage of 10 mg/L) and injection flowrate of 0.14 mL/min were used.

Table 2-1. Summary of operating conditions for the six sets of column experiments explored in this study.

NP Formulation	Exp. set	Aquifer Material[1]	Initial Saturation	Q [mL/min]	C_{inj} [mg/L]	V_{pulse} [mL]	Dose [mg]	Description
Transport	A	BS	Saturated	0.14	500	10	5	Saturated system
	B1	BS	Drained	0.14	50	10	0.5	Low NP concentration
	B2	BS	Drained	0.14	500	10	5	Medium NP concentration
	B3	BS	Drained	0.14	1000	10	10	High NP concentration
	C	BS	Dry	0.14	500	10	5	Initially dry system
	D	BS	Drained	0.06	1000	10	10	Lower flow rate
	E1	SSS	Drained	0.14	1000	45	45	Finer material & high NP dose
	E2	BS	Drained	0.14	1000	45	45	BS & high NP dose
Binding	F1	BS	Unsaturated	0.14	500	20	10	Oil-impacted system
	F2	BS	Unsaturated	0.14	500	20	10	Control

1. BS is Borden sand, and SSS is a synthesized silty sand.

Table 2-2. BTC metrics for Br^- and NPs. Average values and standard deviations are shown.

Exp. set	Tracer			NPs					
	M_R[1]	T_{peak}[3]	T_c^{Br}[4]	Dose	M_R	$C_{retained}^{MB}$ [2]	T_{peak}	T_c^{NP}[4]	T_c^{NP}/T_c^{Br}
	[%]	[min]	[min]	[mg]	[%]	[mg/kg]	[min]	[min]	[-]
A	100	370	396	6.1	83	3.4	380	395	1.00
B1	97	325	347	0.2	53	0.4	325	394	1.01
B2	100±11	340±61	331±66	5.5±0.71	76±5	4.3±1.9	350±6	343±46	1.00±0.02
B3	99±3	320±0	347±7	10.2±0.89	91±5	4.3 ± 0.6	300±0	350±6	1.01±0.01
C	101±4	340±46	374±61	6.2±0.62	25±5	18.6 ± 1.0	385±40	454±46	1.22±0.07
D	99±3	600±46	630±37	8.0±0.75	76±7	6.6 ± 1.3	590±42	631±36	1.00±0.01
E1	98±2	600±20	572±34	53.2±3.5	65±1	65.2 ± 4.4	612±61	621±36	1.09±0.00
E2	97	350	442	43.1	96	6.4	405	439	1.00
F1	99±2	340±35	322±3	8.8±0.63	26 ±3	33.0±2.0	372±31	392±16	1.22±0.04
F2	100	360	390	8.1	49	15.0	415	420	1.05

1. M_R is percent of injected mass recovered.
2. $C_{Retained}^{MB}$ is the average NP concentration retained estimated from mass balance considerations.
3. T_{peak} is the time to the peak of the BTC.
4. T_c is the time to the center of the mass of Br^- or NP BTC.

Table 2-3. Calibrated model parameters. Average values are shown.

Exp. set	Tracer							NPs					
	α_L	ϕ_m	ϕ_{im}	ϕ_T	f_s	γ_{Br}	R^2	γ_{NP}	$M_{attach}^{\max}$	k_a	k_d	k_{str}	R^2
	[m]×10^{-4}	[-]	[-]	[-]	[-]	[1/s]×10^{-5}	[-]	[1/s]×10^{-5}	[mg/kg]	[1/s]×10^{-5}	[1/s]×10^{-6}	[1/s]×10^{-4}	[-]
A	3.6	0.32	NA	0.32	1.00	NA	0.99	NA	7.6	1.6	0.6	--	0.99
B1	2.4	0.27	0.03	0.30	0.90	1.3	0.98-0.99	3.8	7.3	3.1	3.0	--	0.92-0.95
B2	4.0±1.6	0.28±0.02	0.03±0.00	0.31	0.91±0.02	1.0±0.1	0.96 -0.99	1.9±0.7	7.9±0.78	5.1±1.4	7.5±1.0	--	0.96-0.98
B3	3.6±1.7	0.28±0.02	0.03±0.00	0.31	0.91±0.01	1.5±0.3	0.95-0.99	1.3±0.1	8.9±0.25	1.9±0.4	9.1±0.4	--	0.93-0.97
D	1.8±0.3	0.26±0.02	0.03±0.00	0.30	0.88±0.00	0.7±0.2	0.99	0.5±0.2	7.3	1.5±0.8	0.3±0.1	--	0.96-0.99
E1	11±4	0.28±0.01	0.03±0.00	0.31	0.91±0.02	2.0±0.7	0.95-0.99	3.9±1.2	65.4±1.7	40±12	1.1±0.2	--	0.95-0.99
E2	2.1	0.29	0.03	0.31	0.91	2.2	0.99	2.1	6.2	1.0	7.6	--	0.98
F1-oil zone[1]	1.4±0.9	0.31±0.01	0.02±0.01	0.33	0.94±0.03	2.0±0.7	0.95-0.99	2.3±1.6	26.4±1.2	2800±150	4.8±1.1	3.0±0.6	0.95-0.97
F1-clean zone[2]	1.9±0.8	0.31±0.01	0.02±0.01	0.33	0.94±0.03	2.0±0.7	0.95-0.99	2.1±1	8.2±1.3	27±12	7.6±1.1	3.0±0.6	0.95-0.97
F2	1.6	0.33	0.02	0.35	0.93	3.0	0.99	2.0	7.8	24	7.8	2.6	0.98

1. F1-oil zone is the crude oil zone in the middle of the impacted columns.
2. F1-clean zone is the upper and lower clean zones in the impacted columns.

Chapter 3

Unsaturated Transport and Targeted Binding of Pluronic-coated Nanoparticles in a Large Column system

Abstract

Delivery of nanoparticles (NPs) through an unsaturated zone in order to attach to a non-aqueous phase liquid (NAPL) target zone requires an understanding of the transport and binding behaviour of the NPs. In this investigation, NPs coated with a tunable amphiphilic co-polymer were employed in a series of experiments using a 1.4 m long column representative of the unsaturated zone above a shallow aquifer. To evaluate the NP targeted binding capabilities, a crude oil source zone was emplaced in the column. NPs coated with a lower polymer concentration which promote enhanced binding to NAPLs were successfully delivered and retained in the crude oil zone at concentrations ~3 times higher than elsewhere in the column, evident by the NP retention profile. Results from a model that accounts for both physical and chemical nonequilibrium transport provided a good description of the observed asymmetrical NP breakthrough curves. The estimated attachment rate coefficient was about two-orders of magnitude higher for the crude oil zone than the rate for the non-impacted zones, demonstrating preferential binding to the crude oil. NP retention observed at the top of the column was attributed to straining caused by the lower water content and aggregation. In addition to the reversible attachment and straining, results indicated consistent NP retention as the solution migrated further down the column and perhaps some NP mass loss due to aggregation and trapping. As a consequently, a mass loss term was used in the model for the lower half of the column to provide a reasonable fit to the observed data. Findings of this study revealed that despite the demonstrated targeted binding capability of these NPs in unsaturated systems, their delivery to a target NAPL zone distal from the injection location may be a challenge due to possible aggregation over longer travel distances.

3.1 Introduction

Nanoremediation is an emerging technology that exploits the transport and reactivity of particles (< 100 nm in diameter) to treat target contaminants in soil and groundwater (Karn et al., 2009). Considerable attention has been devoted to improving the mobility of nanoparticles (NPs) in porous media; however, delivery of these reagents is still a major limitation. Inefficient delivery of NPs to an impacted target zone may result in NPs migrating downgradient leading to potential environmental consequences. To address this concern, NPs can be engineered to maintain low interaction with porous media and selectively bind to non-aqueous phase liquid (NAPL) contaminants using amphiphilic polymer coatings (Linley et al., 2019; O'Caroll et al., 2013; Saleh et al., 2005; Saleh et al., 2007). Saleh et al. (2007) observed enhanced mobility of amphiphilic copolymer modified iron NPs in saturated porous media, and reported that NPs with a high hydrophobe/hydrophile ratio allowed for targeted binding at NAPL/water interfaces. Once NPs are preferentially bound to a NAPL/water interface, their mobility is restricted and the risk of migration and deposition in non-impacted zones is reduced (Linley et al., 2019; Phenrat et al., 2011). Targeted binding of NPs at NAPL/water interfaces is affected by the hydrophobicity of the NPs which is proportional to the polymer structure (Bishop et al., 2010; Saleh et al., 2007) and concentration (Linley et al., 2020b). Phenrat et al. (2011) established selective binding to NAPL/water interfaces in saturated sand packed 2-D cells using copolymer coated nano-zero valent iron (nZVI), and observed preferential accumulation of nZVI particles in the NAPL zone when moderate to high NP concentrations were used. Recently, we achieved targeted binding of engineered iron oxide NPs towards NAPL-impacted saturated and unsaturated porous media by adding a copolymer coating to the surface of the NPs. This coating promotes hydrophobic interactions with the NAPL, as well as NP stability in aqueous solutions (Jaberi et al., 2021; Linley et al., 2019, 2020a,b).

Knowledge of transport and binding behaviour of NPs is required to design efficient delivery systems in complex subsurface environments as well as to protect groundwater. The transport of NPs through a porous medium is primarily dictated by advection and dispersion, wherein particles move with groundwater, but is also influenced by Brownian and gravitational forces which dominate for small (<0.1 µm) and large (>1 µm) particles, respectively (Elliot and Zhang, 2001). The interactions between NPs and macromolecules exist in natural porous media may change the surface coating of NPs, affecting their retention behaviour along their pathway and governs how far NPs can migrate (Louie et al., 2016). If NP aggregation occurs the increased particle size may result in particle-grain surface collisions due to gravitational sedimentation and interception (Petosa et al., 2010). In saturated porous media, retention of NPs is limited to pore straining (trapping of NPs in pore throats) and attachment at solid-water interfaces (SWIs), while NP transport is further complicated in the unsaturated zone due to the presence of the air phase (Bradford et al., 2003).

Hence, NP retention is much more pronounced owing to a range of phenomena at the microscopic (interaction of NPs with air, in addition to water and solid interfaces) and macroscopic scales (preferential flow and fingering) (McCarthy and McKay, 2004). Yecheskel et al. (2018) reported that the retention of silver NPs was saturation dependant since the retention of NPs decreased with increasing water saturation. Torkzaban et al. (2008) explored the impact of water content on NP transport using experimental and modeling tools, and suggested that a higher retention of NPs (carboxylate-modified latex) in an unsaturated porous medium was due to the entrapment of NPs in immobile porosity regions where the velocity is lower, such as solid-solid junctions, air-water-solid (AWS) interfaces, and dead-end pores. Their experimental observations verified that NP straining was directly correlated with the degree of immobile porosity regions which increased with decreasing water content. Zhang et al. (2010) used direct visualization (digital bright field microscopy) to confirm that NPs were mainly trapped at the AWS interfaces due to the lower velocity in these regions in addition to attachment at the SWIs. Typically, in unsaturated porous media the hydrodynamic interactions (e.g., fluid flow and diffusion) move NPs close to AWIs, where non-DLVO forces such as hydrophobic and capillary forces play a significant role in NP interactions with AWIs and lead to strong retention (Wan and Wilson, 1994; Morales et al., 2009).

Despite extensive investigation on the mobility of NPs in saturated conditions, the transport behaviour of NPs in unsaturated conditions remains poorly quantified. Liang et al. (2013a) observed that the mobility of silver NPs in unsaturated packed columns (loamy sand) was enhanced with increased flowrate. In our previous work (Jaberi et al., 2021), we explored the role of initial water content, flow rate, NP injection concentration, and sediment texture on the transport and retention of engineered iron oxide NPs using a series of bench-scale column experiments. Results from this work indicated that NP transport was directly correlated with water saturation and immobile porosity regions (i.e., AWS interfaces). The transport of NPs decreased with a lower injection flowrate as a result of an increase in residence time and comparatively reduced water saturation. It was also observed that the retention of NPs increased in sediments with higher clay and silt content which provided larger surface area and subsequently more NP retention sites. The transport of NPs was found to be independent of concentration for the investigated range (50 to 1000 mg/L). Aside from physical factors, physicochemical properties of the NPs can dictate their potential transport and reactivity. For example, changes in particle shape and size which could result from aggregation may lead to subsequent retention and restrict NP mobility (Petosa et al., 2010; Raychoudhury et al., 2012).

To predict the fate and transport of NPs modeling tools are typically combined with data from laboratory-scale experiments. NP transport and retention are commonly described using a modified form of the advection dispersion reaction equation (ADRE) combined with a reversible kinetic attachment/detachment model (e.g., Bradford et al., 2002; Liang et al., 2013a,b; Rahmatpour et al., 2018). Transport models that allow depth- dependant retention and reversibility of retained NPs are better descriptors of NP behaviour, especially in natural porous media (Liang et al., 2013a). Some studies have shown that when the ADRE formulation is expanded to account for both mobile and immobile porosity regions, the simulation results provide an improved description of the transport of solutes and NPs in unsaturated conditions. This expanded formulation is able to account for mass transfer of solutes and NPs between the mobile and immobile regions with lower velocity, and therefore represents both physical and chemical non-equilibrium transport (Cherrey et al. 2003; Kätterer et al., 2001; Padilla et al., 1999; Prédélus et al., 2017; Šimůnek and van Genuchten, 2008). Prédélus et al. (2017) explored the transport of NPs in small unsaturated soil columns (length of 30 cm, inside diameter of 10 cm) and employed a mobile/immobile model and demonstrated that this model provided a good description of the hydrodynamic properties of the porous medium as well as the retention and transport behaviour of NPs. In our previous study (Jaberi et al., 2021), the transport and retention behaviour of NPs in short unsaturated column systems was adequately captured by a mobile/immobile model in conjunction with a reversible kinetic attachment/detachment model.

While studies using short columns provide valuable information regarding the mechanisms controlling the transport of NPs in saturated or unsaturated porous media, they are unable to capture NP migration over transport distances representative of potential field applications. Hoggan et al. (2016) investigated the transport and retention of titanium dioxide (TiO_2) NPs in 1.2 m long columns (inside diameter of 2.5 cm) under saturated and unsaturated conditions. They observed that NP retention in unsaturated conditions was strongly correlated with depth due to variations in capillary pressure which led to increased film straining at the top of the column. The relative importance of the rate of NP collisions, interactions, release and attachment on sediments can change with travel distance (Bradford et al., 2011; Tufenkji and Elimelech 2004). For *in situ* treatment applications, NPs may be required to travel some distance (> 1 meter) from the injection point to reach a target treatment zone. *In situ* delivery of NPs, as remediation agents or as delivery vehicles for a treatment reagent, is controlled by typical physical and chemical heterogeneities and by the presence of the air phase in the unsaturated zone. To better understand and predict the transport of NPs in the unsaturated zone and to support the design of NP delivery systems, it is critical to expand our knowledge in conditions representative of a field application.

To satisfy this need, we used our previous work on the transport and targeted binding of Pluronic-coated NPs in short columns (15 cm long) (Jaberi et al., 2021; Linley et al., 2019, 2020a,b) as a springboard to investigate their behaviour in a 1.4 m long lysimeter or column. This column system was deemed to be representative of the unsaturated zone above a shallow aquifer where the water table is <1 m from ground surface. The transport of Pluronic-coated NPs in this system was evaluated first before the targeted binding capability towards a crude oil source zone was explored. To resemble a potential field delivery method, an infiltration system was used for the delivery of NPs into the column. The transport and binding behaviour of NPs in this unsaturated system was characterized using a reactive transport model. This model was previously used in our short column study where it successfully described physical and chemical non-equilibrium transport of these engineered NPs (Jaberi et al., 2021).

3.2 Materials & Methods

3.2.1 Materials

The preparation of iron oxide NPs (Fe-NPs) and cobalt ferrite NPs (CoFe-NPs) were performed as in Linley et al. (2019) and Linley (2019), respectively. These NPs are comprised of a three-layer hierarchical sphere with a core of iron oxide (Fe_3O_4) or cobalt ferrite ($CoFe_2O_4$), a middle layer of oleic acid, and an outer layer of a Pluronic block co-polymer (P104, L62) (poly (ethylene oxide)-poly (propylene oxide)-poly (ethylene oxide) (PEO-PPO-PEO)). Briefly, the preparation of the iron oxide NPs involved adding $FeSO_4 \cdot 7H_2O$ and $FeCl_3 \cdot 6H_2O$ to deoxygenated water at a molar ratio of 2:3 ($FeSO_4$:$FeCl_3$). Adequate NH_4OH and oleic acid were then added to attain final concentrations of 4 and 0.22 mol/L, respectively, and the solution was stirred at 70 °C for 1 hour, then stirred at 90 °C under flowing N_2 for additional 1 hour to purge any NH_3 gas generated. After cooling to room temperature, the precipitate was recovered by magnetic decantation and washed 3 times with deoxygenated Millipore water, and 3 times with ethanol (EtOH) before being dried under flowing air. CoFe-NPs were produced through solvothermal decomposition of iron and cobalt oleates at 180 °C in a stainless steel autoclave, then washed 3 times with EtOH before drying under flowing air. Pluronic concentration of 10 g/L (identified as the transport formulation) and 2.5 g/L (identified as the binding formulation) were used to coat the Fe-NPs and CoFe-NPs, respectively. The binding formulation has previously been shown to have a higher affinity towards crude oil, whereas the transport formulation has higher mobility and increased stability in aqueous suspensions (Linley, 2019). Transmission Electron Microscopy (TEM) images of the iron and cobalt NPs are presented in Appendix B (see Figure B-1).

Crude oil (sour crude, API gravity 13.3 (density of 0.977 g/cm^3), average linear carbon number of 25.1, kinematic viscosity 4.75 x 10^{-4} m^2/s at 40 °C) was provided by Chevron Energy Technology Company (Houston, TX, USA). Sodium bromide (NaBr, ACS grade, ≥ 99%), dichloromethane (DCM, > 99.9 %), hydrogen peroxide (H_2O_2, 30%), hydrochloric acid (HCl, ACS grade, 37%), ethanol (ACS grade, 99%), hexane (ACS Grade, >98.5%), and nitric acid (HNO_3, ACS grade, 70%) were purchased from Fisher Scientific. Iron (II) sulphate heptahydrate (FeSO4 · $7H_2O$, >99%), iron (III) chloride hexahydrate ($FeCl_3$ · 6H2O, >99%), ammonium hydroxide (NH_4OH, 28%-30% in water), oleic acid (>90%), sodium oleate (> 90% fatty acids (as oleic acid) basis), iron (III) nitrate nonahydrate ($Fe(NO_3)_3 \cdot 9H_2O$, ACS grade, > 98%), cobalt (II) nitrate ($Co(NO_3)_2 \cdot 6H_2O$, ACS grade, > 98%), sodium hydroxide (NaOH, ACS grade, > 98%), 1-pentanol (ReagentPlus® grade, >99%) were purchased from Sigma Aldrich. Pluronic co-polymer P104 and L62 were gifted by BASF, Canada. All chemicals were used as received. Millipore water was obtained from a direct water purification system (EMD Millipore, 18.2 MΩ·cm at 25 °C).

Aquifer material (denoted here as "Borden Sand" (BS)) (d_{10} of 75 µm) with 2 % gravel, 92 % sand, 5.9 % silt, and 0.1 % clay was collected from 1 m below ground surface at the University of Waterloo Groundwater Research Facility at the Canadian Force Base (CFB) Borden near Alliston, ON, Canada. The mineralogy of BS has been extensively studied and compositional analyses can be found elsewhere (Ball et al. 1990). The BS was sieved (1 mm mesh) to remove larger particles, rinsed well with Millipore water until the filtrate ran clear, oven dried at 90 °C overnight, and then stored in sealed polyethylene bags at 4°C until used. The particle size distribution was determined using standard methods (ASTM D 422, 2007) (see Figure B-2).

3.2.2 Column experiments

All experiments were conducted in a 142 cm long PVC column, with an inside diameter of 15 cm (Figure 3-1). A stainless steel mesh screen (75 µm) was fitted in the bottom of the column to prevent loss of fines, followed by a ~2 cm thick layer of glass beads (4 mm, Fisher Scientific) to collect and direct flow to the column outlet. The column was homogenously wet-packed using 3-cm thick lifts. Each lift was carefully compacted using a 5 cm diameter rod, and then the surface was scraped with an abrasive brush to prevent heterogeneous layering when the next layer was added. The column was filled to a depth of 135 cm, and a ~2 cm layer of glass beads (4 mm, Fisher Scientific) was placed on top of the final layer to distribute flow from the injection system. Three tensiometers (T5 mini-tensiometer, Hoskin scientific LTD) and three moisture probes (GS-1, Hoskin scientific LTD) were installed during packing at 5, 74 and 130 cm from the bottom of the column (denoted as bottom, center, and top probes) and used to obtain water pressure and volumetric water content data. All instruments were connected to a data logger (CR1000, Campbell Scientific) with a sampling and storage rate of once every 30 secs. The tensiometers and moisture probes were calibrated before use. Six solution samplers (Rhizon, MOM, Hoskin scientific LTD) denoted as SP-1 to SP-6 were also installed during packing in ports spaced at ~20 cm intervals along the column length. Each sampler extended 7 cm into the column and was offset horizontally by 60-degrees relative to the other samplers. Following packing, the column was saturated bottom-up, and a constant head test (ASTM 2434) was performed to estimate the saturated hydraulic conductivity (0.43 ± 0.007 cm/min). The injection system was comprised of a peristaltic pump (Cole Parmer, MasterFlex 7535-04) connected to a 15-cm diameter perforated plate (20 1-mm diameter holes evenly distributed) by a 200 cm length of 6.35-

mm diameter tubing (Flexible PVC, Fisher Scientific). The perforated plate was suspended 5 cm above the surface of the glass bead layer to spread the tracer and NPs over the upper column surface.

Three types of experiments were conducted in this column system: conservative tracer, Fe-NP transport, and CoFe-NP transport and binding. First, a conservative tracer experiment was performed to characterize the hydraulic and transport properties of the column system. Next, to explore the transport of Pluronic-coated NPs over a longer distance (140 cm compared to 15 cm previously used) in an unsaturated porous medium, Fe-NPs coated with the higher polymer coating concentration were used. Finally, the CoFe-NP transport and binding experiment involved delivering NPs with the lower polymer coating concentration to a crude oil source zone in the column. Linley (2019) showed that while NPs with either the Fe or CoFe core material (with the same coating formulation) had identical transport characteristics, the naturally high background concentration of Fe in BS (~3000 ± 400 mg/kg) required a different NP core material (i.e., cobalt) to be used so that the mass distribution of NPs retained in the column could be determined. All experiments were conducted at room temperature (~22 ^{o}C).

To achieve the initial unsaturated condition for the tracer and Fe-NP transport experiments, the water pressure head was lowered from 140 cm to 20 cm from the base of the column and the system was allowed to gravity drain for > 24 hrs. The pressure measured along the column was used to ensure that steady-state conditions were reached before the start of each experiment. For the tracer experiment, ~1000 mL of a NaBr solution (~400 mg-Br^-/L) was allowed to irrigate at a constant flowrate (~20 mL/min) for ~60 minutes, followed by Millipore water at the same flowrate for an additional ~500 min. Effluent samples were collected every 15 minutes in 40 mL glass vials (VWR, Mississauga, ON, Canada). The sample volume and filling time was used to estimate the effluent flowrate. In addition, aqueous samples (~ 3 mL) were collected from the solution samplers every 15±2 minutes using syringes and stored in 3-mL polypropylene cryogenic vials (VWR, Mississauga, ON, Canada). This sampling rate was selected (a total of 6% of total pore volume extracted by all samplers at each time point) to have minimal impact on the flow field. At the end of the tracer experiment, the irrigation rate of Millipore water was increased for 24 hrs to remove any remnant Br^- before the column was saturated and allowed to gravity drain. The Fe-NP transport experiment was conducted using the same procedure as the tracer experiment, except that instead of Br^-, a Fe-NP solution with a target concentration of 1000 mg-Fe_T/L was used.

For the CoFe-NP transport and binding experiment a crude oil zone was emplaced in the column. To prepare the crude oil source zone material, an appropriate volume of Millipore water was first thoroughly mixed with dry BS to achieve a volumetric water content of ~0.25 v/v. Then the moist BS was mixed with crude oil (2 % wt) heated to 60 °C, and homogenized by stirring. This volumetric water content value was selected so that the initial water content in the crude oil source zone was consistent with neighboring BS zones. The volumetric water content was estimated through mass measurements of the added water to the mass of dry BS used to pack a segment, multiplied by the bulk density (mass of dry BS/volume of packed segment). The upper 63 cm of column was unpacked, and a ~20-cm thick layer (~80 to 100 cm from the column bottom) of the oil-impacted BS was packed followed by the moist BS (prepared as described above) to a packed height of 135 cm (see Figure 3-1). Although a small segment (~ 5cm thick) below the crude oil source zone was packed with moist BS (74 to 79 cm), the porous medium below this height remained untouched from the previous Fe-NP transport experiment. Unlike the first two experiments, the column was not saturated and allowed to gravity drain before starting but was used as packed.

The CoFe-NP transport and binding experiment was operated to mimic a potential field application scenario with the objective to deliver NPs throughout a crude oil source zone and minimize NP migration beyond this zone to limit unwanted environmental impacts. To determine the applied irrigation rate and NP loading, preliminary simulations using the model described below (Section 3.2.4.1) were conducted to assess NP breakthrough and retained mass behaviour. The hydraulic and transport parameters estimated from the tracer experiment were used. The CoFe-NP attachment/detachment model parameters were taken from our previous short column study (Jaberi et al., 2021), and assumed to be approximately representative of NP behaviour in the longer column system. The simulated scenario that yielded the highest mass of NPs retained in the crude oil source zone and the lowest percentage of NP mass exiting this zone used: an irrigation rate of 15 mL/min, and injection CoFe-NP concentration and volume of 500 mg/L and 1000 mL. For this transport and binding experiment, NaBr was added to the CoFe-NPs injection solution to reach a Br^- concentration of ~400 mg/L. Similar to the tracer and Fe-NP transport experiments, the solution was allowed to irrigate at a constant flowrate (15 mL/min) before switching to Millipore water. The water pressure head at the bottom of the column was maintained at 20 cm consistent with the other experiments.

At the end of the CoFe-NP transport and binding experiment, the column material was carefully excavated from top to bottom, and subsamples were analyzed to determine the spatial distribution of the retained mass of CoFe-NPs. Subsamples were collected using custom made stainless-steel cylinders (3-cm ID, and 1 or 2 cm deep) from the column center, and from the four major compass directions (north, west, east, and south) (see Figure B-3). A 1-cm thick excavation lift was used in the crude oil source zone, and a 2-cm thick excavation lift elsewhere. The cylinders were placed on the surface of each lift and gently advanced with a rubber hammer. Once all cylinders were in-place, the surrounding material was carefully removed and each subsample was transferred to a 40-mL glass jar (VWR, Mississauga, ON, Canada) for storage at 4°C. The average mass of the retained CoFe-NPs per kg of sediment in each subsample was determined and used to develop a NP retention profile. The remnants of each 1-cm thick layer in the crude oil source zone was homogenized and a 10-g sample was transferred into a 50 mL glass vial (VWR, Mississauga, Ontario) for total petroleum hydrocarbon (TPH) analysis.

The mass of the NPs that can be attached to clean or crude oil impacted BS ($M_{attached}$) was estimated from batch binding tests (Table B-1) (see B-2 for details). For the Fe-NPs with the transport formulation coating, the estimated value was 7.8 ± 2.3 mg/kg for BS (Linley et al., 2020a), and for the CoFe-NPs with the binding formulation coating the estimated value was 8.2 ± 0.6 mg/kg for BS, and 25.9 ± 2.1 mg/kg for the crude oil impacted BS.

3.2.3 Analyses

To quantify the total iron or cobalt concentration (Fe_T, Co_T) present in aqueous samples (i.e., assuming the core material was composed 100 % of Fe_3O_4 and $CoFe_2O_4$, respectively), a 1 mL aliquot was digested with 0.2 mL of 12.1 mol/L HCl solution (37 %) to dissolve the NPs, diluted to a final volume of 10 mL with 0.1 mol/L HCl, and then analysed using Inductively Coupled Plasma Optical Emission Spectrometry (ICP-OES) (ICP-OES; Teledyne Leeman Laboratories; method detection limit (MDL) of 0.004 mg/L for both Fe and Co). Aqueous Br^- concentration was measured using ion chromatography (Dionex ICS-1100) with a MDL of 0.5 mg/L. The concentration of CoFe-NPs retained in sediment was estimated using solid digestion (EPA Method 3050b) of excavated subsamples followed by ICP-OES analyses (see B-1 for details). To ensure the reliability of the estimations of the retained Co_T in the sediment subsamples, our digestion method and analytical measurements used were validated by an external laboratory (ALS environmental, Waterloo, Canada) (see B-1 for details).

To determine the TPH concentration of the 10-g sample, 15 mL of DCM was added to the 50 mL glass vial and shaken for one week. An aliquot of the DCM mixture was then analysed by gas chromatography with a flame ionization detector (GC-FID; Agilent GC equipped with an auto-sampler; MDL of 0.38 mg-TPH / kg dry sediment) and the mass of TPH in each sediment sample (mg of TPH per kg of sediment) was determined.

3.2.4 Modelling

3.2.4.1 Description

The observed transport and binding behaviour of NPs was simulated using a flexible one-dimensional flow and transport model, 1DUSAT (Thomson, 2019). We previously demonstrated that this model was able to reproduce observed NP transport and binding behaviour in unsaturated 15-cm long columns (Jaberi et al., 2021). 1DUSAT solves the mixed form of Richards' equation (Celia et al., 1990) for unsaturated flow conditions combined with the non-hysteretic capillary pressure - water saturation relationship, and relative permeability function developed by van Genuchten (1980). To describe the water flow, the numerical solution of the Richards' equation requires the knowledge of the porous medium hydraulic parameters including the residual water content θ_r (m^3/m^3), total porosity (or saturated water content) ϕ_T (m^3/m^3), the van Genuchten model parameters n (-) and α (1/m), the saturated hydraulic conductivity K_s (m/s), and the tortuosity factor l (-) for the hydraulic conductivity function. The total porosity (ϕ_T) in 1DUSAT model is divided into mobile (ϕ_m) and immobile (ϕ_{im}) regions ($\phi_T = \phi_m + \phi_{im}$). The following ADRE is used to represent the mobile regions

$$\begin{aligned}&\phi_m S_w^m \frac{\partial C_w^m}{\partial t} = \frac{\partial}{\partial z}\left(D\frac{\partial C_w^m}{\partial z}\right) - q\frac{\partial C_w^m}{\partial z} - \phi_m S_w^m \psi_c^m k_a C_w^m + \rho_b k_d f_s M_{attach}^m \\ &-\phi_m S_w^m \psi_{str} k_{str} C_w^m - \phi_m S_w^m k_L C_w^m - \gamma(C_w^m - C_w^{im})\end{aligned} \tag{1a}$$

$$f_s \rho_b \frac{dM_{attach}^m}{dt} = \phi_m S_w^m \psi_c^m k_a C_w^m - f_s \rho_b k_d M_{attach}^m \tag{1b}$$

with the following reaction equations for the immobile regions

$$\phi_{im} S_w^{im} \frac{\partial C_w^{im}}{\partial t} = +\gamma(C_w^m - C_w^{im}) - \phi_{im} S_w^{im} \psi_c^{im} k_a C_w^{im} + (1-f_s)\rho_b k_d M_{attach}^{im} \tag{2a}$$

$$(1-f_s)\rho_b \frac{dM_{attach}^{im}}{dt} = \phi_{im} S_w^{im} \psi_c^{im} k_a C_w^{im} - (1-f_s)\rho_b k_d M_{attach}^{im} \tag{2b}$$

where m and im refer to mobile and immobile regions; S_w^m and S_w^{im} is water saturation (-); C_w^m and C_w^{im} is the aqueous Br$^-$ or NP concentration (g/m^3); $D = \phi_m \tilde{D} = \alpha|q| + \phi\tau_w D_w^*$ is the dispersion coefficient (m^2/s), α_L is dispersivity (m), q is Darcy flux (m/s), D_w^* is the aqueous diffusion coefficient (m^2/s), τ_w (-) is the tortuosity factor; ψ_c^m and ψ_c^{im} are blocking coefficients (-); k_a and k_d is the attachment and detachment rate coefficient, respectively (1/s); k_{str} is the straining rate coefficient (1/s) and $\psi_{str} = (1 + x / d_{50})^{-\beta}$ is the straining blocking coefficient (-) which is used to account for depth-dependent retention of NPs (1/s), d_{50} is the mean grain diameter (m), x is distance from the column inlet (m), and β is an empirical variable (-); $f_s = \phi_m / \phi_T$ is the fraction of mobile water (-); k_L is a first-order mass loss rate coefficient (1/s); ρ_b is the bulk density (kg/m^3); M_{attach}^m and M_{attach}^{im} is the mass attached to the sediment or oil-impacted sediment (g/kg); and γ is the first-order mass exchange coefficient between the mobile and immobile regions (1/s). The maximum attachment of NPs at retention sites was described using the following nonlinear Langmuirian relationship (Adamczyk et al., 1994) for the blocking coefficient, ψ_c

$$\psi_c = 1 - M_{attach} / M_{attach}^{\max} \tag{3}$$

where $M_{attach}^{\max}$ is the maximum mass of NPs that can be attached to the sediment or oil-impacted sediment (mg/kg).

3.2.4.2 Parametrization

To estimate model parameters, 1DUSAT was coupled with a heuristic global search algorithm; the dynamically dimensioned search (DDS) optimization method (Tolson and Shoemaker, 2007) within the OSTRICH toolkit (Matott, 2017). Initially the DDS algorithm searches globally across the calibration range given for each parameter, and becomes more local as it moves towards the specified number of total model evaluations.

An initial hydrostatic pressure head profile based on a 20-cm pressure head at the bottom of the domain was assumed. Transient boundary conditions were a specified water flux at the top of the domain and a prescribed water pressure head (20 cm) at the bottom. For all tracer and NP simulations, a total mass flux was specified at the top boundary, and a zero dispersive flux at the bottom boundary. The initial Br^- or NP concentration distribution was set to zero. The 137-cm long domain (135 cm of packed BS + 2 cm of glass beads) was discretized into 5000 computational volumes, and an initial time step interval of 1.0 sec was used and allowed to increase by 0.02% until a maximum time step increment of 10 secs was reached.

The hydraulic parameters including total porosity (ϕ_T), residual water saturation (S_{wr}), empirical capillary pressure - water saturation parameters (n and α) were estimated by calibration, and the saturated hydraulic conductivity (K_{sat}) was assigned the estimated value from hydraulic testing. The observed outflow data from each experiment were used as calibration targets with a root mean square error (RMSE) objective function as the model calibration criteria. To make sure that an optimal solution was obtained, three different calibration trials and 100 model evaluations were performed. For each calibration trial a different initial solution was assigned randomly from the calibration range of each parameter to allow the DDS algorithm to start from a new solution. For each model calibration step, the parameter set that produced the lowest RMSE was considered optimal. In addition, the goodness of fit was assessed using residual analyses. The randomness of the residuals (observed-simulated values) was evaluated using Shapiro-Wilk normality test and considered acceptable for $p > 0.05$ (Shapiro and Wilk, 1965).

A similar calibration approach, as described above for the hydraulic parameters, was used to estimate the transport parameters including dispersivity (α_L), mobile porosity (ϕ_m), immobile porosity (ϕ_{im}), and the first-order mass exchange coefficient (γ_{Br}) for Br$^-$ using the observed Br$^-$ effluent data as the calibration target in conjunction with the estimated hydraulic parameters. The kinetic attachment/detachment as well as straining and mass loss terms in Eqs (1) and (2) were not used for the Br$^-$ simulations. Finally, using the calibrated hydraulic and transport parameters, the NP parameters ($k_a, k_d, \gamma_{NP}, k_{str}$, and k_L (if required)) were estimated using the observed NP effluent data as well as data from the solution samplers (if available). The maximum mass of attached NPs ($M_{attach}^{\max}$) was also calibrated within a range constrained to the 95% confidence interval (CI) as determined from the binding batch tests (see Table B-1) The bulk density was assumed to be 1800 kg/m^3 (Ball et al., 1990). Based on a series of preliminary simulations, the depth-dependent straining term in Eq (1) was activated, and the straining rate coefficient (k_{str}) was an additional calibration parameter. The mean grain diameter (d_{50}) was assigned a value of 0.02 cm based on Figure B-2, and β was set to 0.432 determined by Bradford et al. (2003).

For the Fe-NP transport experiment, a sequential calibration approach was used by considering the NP data obtained from sampling points (SP-1 to SP-6) along the column as well as the Fe-NP effluent data. In this approach the domain was divided into 6 zones as shown in Figure B-4(a) and calibration was performed sequentially from the top to the bottom. For the first zone, calibration was conducted using only the Fe-NP data from the top sampler (SP-1) as the calibration target. Then for the second zone the estimated parameters for the first zone where held fixed, and the parameters for the second zone were determined using the Fe-NP data from SP-2. This sequential calibration approach proceeded down the column to the last zone (Zone 6) where the effluent Fe-NP data was used as the calibration target.

For the CoFe-NP transport and binding experiment, the observed effluent CoFe-NP data was used as the calibration targets to estimate parameters for three distinct zones (see Figure B- 4(b)): Zone 1, the upper BS packed section include ~ 5 cm below the crude-oil source zone; Zone 2 the crude-oil source zone; and Zone 3 the lower BS packed section. Since the lower section of the column (Zone 3) had been exposed to Fe-NPs from the previous experiment some differences in behaviour were expected compared to Zone 1. In addition to using the CoFe-NP BTC data as the calibration target, the parameter set that also produced the best fit with the observed retention profile (using residual analyses) was deemed optimal.

3.3 Results and discussion

3.3.1 System Hydraulics

Prior to the start of each experiment (i.e., tracer, Fe-NP transport, and CoFe-NP transport and binding), the water pressure and associated volumetric water content at the three locations along the column indicated that steady conditions existed (see Figure B-5). The controlled water pressure head at the bottom of the column resulted in a constant positive water pressure between 12 to 15 cm H_2O at the bottom tensiometer (located at 5 cm above the base) (Figure 3-2). Consistent with this positive water pressure, the corresponding water content at the bottom probe yielded values between 0.32 and 0.36 v/v which is close to the expected porosity for saturated BS (ϕ_T = 0.35) (Ball et al., 1990). Following the onset of infiltration, the water content at the top probe dramatically increased and reached a steady value of 0.23 and 0.24 (v/v) in the tracer and Fe-NP transport experiments, respectively, and 0.14 (v/v) in CoFe-NP transport and binding experiment. The lower water content at the top probe for the CoFe-NP binding experiment is attributed to the lower irrigation rate. Similarly, the water content at the center probe gradually increased to a steady value for each experiment as the wetting front propagated down the column (0.23 to 0.25 v/v for the tracer and Fe-NP transport experiments, and 0.15 v/v for the CoFe-NP transport and binding experiment). The negative water pressure head at the center and top probes (-0.7 to -0.26 m H_2O) indicated that ponding did not occur near the top of the column, and unsaturated conditions were present during all experiments above the ~20 cm saturated zone at the base of the column.

In all experiments, a sharp flow breakthrough profile at the column outlet was observed with no initial flow to a near constant rate between 15 to 30 minutes (Figure B-6). The observed average flowrate for the tracer, transport and binding experiments were 18.5 mL/min, 17.2 mL/min, and 14 mL/min, respectively, which are slightly lower than the target flowrates due to experimental variability (Table 3-1). Despite a lower flowrate used in the CoFe-NP transport and binding experiment, the earlier flow arrival at the outlet compared to the tracer and Fe-NP transport experiments (135 vs 150 minutes) could be due to the slightly different packing method used and the presence of the crude oil zone.

The calibrated hydraulic parameters using the outflow data from tracer and Fe-NP transport experiments were nearly equal (see Table B-2). The identical experimental conditions between the tracer and Fe-NP transport experiments is demonstrated by simultaneous flow arrival at the column outlet, similar water content and pressure data, as well as nearly identical estimated hydraulic parameters. The calibrated hydraulic parameters for the crude oil source zone and the non-impacted BS zones from the CoFe-NP transport and binding experiment are essentially identical, except that a slightly larger value of α was estimated for the crude-oil source zone.

3.3.2 Column Experiments

3.3.2.1 BTC observations

The shape of the observed effluent Br^- breakthrough curves (BTCs) for both experiments (i.e., tracer and CoFe-NP transport and binding experiment) was asymmetrical with a steep increase to the peak concentration followed by a gradual declining limb (Figure 3-3 and Figure 3-4). Similar tailing behaviour was observed in the effluent Br^- BTCs from our previous short column study (Jaberi et al., 2021) and is commonly attributed to the presence of immobile water regions (i.e., low velocity regions) or dead-end pores present in an unsaturated porous medium (Gao et al. 2006; Kumahor et al., 2015b; Prédélus et al., 2017). The observed effluent Fe-NP and CoFe-NP BTCs also showed an asymmetrical shape with more tailing and lower peak concentrations relative to their respective Br^- BTCs. The presence of NPs was not detected in the effluent until 390 min into the Fe-NP transport experiment and 450 min into the CoFe-NP transport and binding experiment. This delayed the arrival of the center of mass of the NP BTCs (T_c^{NP}) at the column outlet compared to the center of mass of Br^- BTC (T_c^{Br}) with a ratio (T_c^{NP}/T_c^{Br}) of 1.08 for the Fe-NP experiment and 1.11 for the CoFe-NP experiment.

The mass recovery of Br^- and NPs was estimated by integrating under the BTC and normalizing by the infiltrated mass ($M_R = M_{out}/M_{in}$). BTC metrics including M_R, time to peak concentration (T_{peak}), time to the center of mass of the effluent Br^- and NP BTCs (T_c^{Br}, T_c^{NP}) are listed in Table 3-2. Almost all the Br^- mass infiltrated was recovered (M_R ~100%) in both the tracer and CoFe-NP experiments, while the mass of NPs recovered was 30% for Fe-NP experiment and only 9% for the CoFe-NP experiment. In addition to the non-equilibrium physical transport demonstrated by the tracer BTC, the delayed NP arrival and suppressed peak concentrations with respect to the tracer, as well as the lower M_R for the NPs confirms that significant interactions occurred within the column.

NP transport was also examined along the column length using the observed Br^- and NP BTCs from the six solution samplers (Figure 3-3 and Figure 3-4). The Br^- and Fe-NP BTCs at SP-1 and SP-2 (height of 1.19 and 1.03 m) are essentially coincident; however, as the NP solution migrated down the column, both the peak concentration and tailing of Fe-NP BTCs diverged from those of the Br^- BTCs. The arrival time ratio (T_c^{NP}/T_c^{Br}) of the Fe-NP BTCs was essentially unity at SP-1 to SP-3 and gradually increased from 1.01 to 1.05 at SP-4 to SP-6. These observations reflect consistent Fe-NP retention as the solution migrated down the column and perhaps some NP mass loss due to aggregation and trapping.

Despite preliminary testing of potential interactions between the solution samplers and the CoFe-NPs that would hinder their performance to collect aqueous samples, complete clogging of the porous needle at SP-

1 and SP-2 occurred (see Figure B-8). While aqueous samples were collected from SP-3 to SP-6 their representativeness of the pore water is uncertain. Nevertheless, similar to the Fe-NPs, the arrival time of the CoFe-NP BTCs at each sampler was delayed with respect to the Br^- BTCs and increased as the NP solution migrated down the column.

Consistent with the M_R values, the retained concentration of Fe-NPs ($C_{retained}^{MB}$: mass of Fe-NPs per mass of solids based on mass balance) (Table 3-2) was 13.8 mg/kg, which is ~2 times higher than the attachment capacity of Fe-NPs to BS estimated from the batch binding tests (7.8 ±2.3 mg/kg). This additional NP retention is presumably due to the presence of AWS interfaces, and physical trapping due to aggregation.

The lateral distribution of the retained concentration of CoFe-NPs in each layer ($M_{retained}$) (using solid digestion and ICP-OES method) within the upper non-impacted zone (Zone 1 in Figure B-4(b)) and the crude oil zone (Zone 2 in Figure B-4(b)) was explored. A series of statistical analyses were performed to see if there was a difference between the concentrations determined for the five subsamples (denoted as center, north, west, east, and south) collected from each layer. Results indicated that the variation between the five concentrations for each layer in Zone 1 was not statistically significant ($p > 0.05$) suggesting the absence of preferential pathways. In contrast, a statistically significant difference was found between the concentrations determined for the five subsamples from each 1-cm layer within the crude oil zone (Figure B-10) presumably due to the minor variations in crude oil concentration. The location of the maximum retained CoFe-NP concentration in each layer within the crude oil zone is presented in Table B-3. The average CoFe-NP retained concentration in each layer were used to develop the retention profile (Figure 3-5). The CoFe-NP retention profile clearly indicates an overlap with the TPH distribution also shown on Figure 3-5. The concentration of CoFe-NPs retained in the crude oil zone (16 to 25 mg/kg) was ~3 times higher than the surrounding non-impacted zones (5 to 12 mg/kg) (Zones 1 and 3). Consistent with our previous targeted binding investigations (Linley et al., 2019, 2020a,b; Jaberi et al., 2021), the CoFe-NP accumulation in the crude oil zone demonstrates targeted binding behaviour as a result of hydrophobic interactions between hydrophobic groups in the CoFe-NP coating (i.e., PPO segment of the Pluronic coating and oleic acid inner coating) and the hydrocarbon chains in the crude oil. The concentration of CoFe-NPs retained in the non-impacted zone (Zone 1) (from 1.0 to 1.3 m and 0.74 to 0.79 m) ranged from 6 to 12 mg/kg with the higher end of this range reflecting straining of CoFe-NPs near the top of the impacted column. No CoFe-NPs were detected in the sediment subsamples from the lower non-impacted BS zone (i.e., Zone 3 in Figure B-4(b)). The average retained concentration of CoFe-NPs in the upper non-impacted BS zone (Zone 1) (7.2 ±2.0 mg/kg) and the oil zone (22 ±2.9 mg/kg) are close to the attachment capacity of CoFe-NPs to clean and crude oil-impacted BS, respectively, from the batch binding tests.

3.3.2.2 Simulations

The best-fit simulated effluent Br^- BTC from the tracer and CoFe-NP experiments closely match the observed effluent BTC data ($R^2 = 0.97$ and 0.99; residuals normally distributed, see Figure B-7) indicating that the model was able to reproduce the observed Br^- transport behaviour (Figure 3-3(a) and Figure 3-4(a)). Although the transport parameters (Table 3-3) were determined using the effluent Br^- BTC data as the calibration target, these parameters yielded good fits to the observed Br^- BTCs at the solution sampler locations ($R^2 = 0.81 - 0.99$) (Figure 3-3(a) and Figure 3-4(a)). For the CoFe-NP experiment, the simulated sampler Br^- BTCs provided a good match with the observed data at SP-3 to SP-6, except for SP-5 (Figure 3-4 (a)), likely due to sampling issues (e.g., sampling frequency or clogging of the porous needle).

The simulated Fe-NP BTC for the effluent and at the sampler locations using the sequential calibration approach provided a good fit to the observed data ($R^2 = 0.82 - 0.99$), except at SP-6 (Figure 3-3(b)). The anomalous SP-6 Fe-NP BTC data is believed to be due to the sampler issues, and thus data from SP-6 was not considered as a calibration target for the parametrization of Zone 6 (see Figure B-4(a)), instead using effluent data from the Fe-NP BTC. For all NP simulations, we assumed that the NP transport and attachment/detachment parameters (i.e, k_a, k_d, $M_{attach}^{\max}$) were identical in both the mobile and immobile porosity regions, since the sediments were homogenized prior to packing. Previously a simple reversible kinetic attachment/detachment model was sufficient to describe the retention behaviour of the Fe-NPs in short column systems (Jaberi et al., 2021; Linley et al., 2020b). However, in this study a model incorporating the depth-dependent straining term (see Eq (1a)) was found to provide a better fit with the observed Fe-NP BTCs, especially near the top of the column (i.e., for the SP-1 BTC data). This was also found to be the case for the CoFe-NPs which showed higher retention in the first 5 cm of the impacted column, a behaviour which was captured by the depth-dependent straining term. A mechanistic investigation into the straining behavior was not a focus in this research.

Based on a series of preliminary simulations, it was found that the incorporation of the generic first-order decay term in Eq 1(a) (i.e., $\phi_m S_w^m k_L C_w^m$) was necessary to simulate the observed peak concentrations in the Fe-NP BTC at the effluent and at the SP-4 and SP-5, as well as that CoFe-NP effluent BTC. This first-order decay term essentially removes NP mass from the system as result of suspected aggregation and subsequent physical trapping deeper in the column. As NPs migrate longer distances, their coating polymer structure may be stripped off due to increased contact with sediments which causes aggregation and leads to reduced mobility due to physical trapping in pore throats. As previously reported, the oxygen in the PEO chain of the coating material can interact with the surface of acidic metal oxide groups, such as silanol, and lead to stripping of Pluronic from the NP's core resulting in aggregation (Addai-Mensah, 2007).

According to colloid filtration theory (CFT) (Yao et al., 1971) the removal of NPs from an aqueous phase is a first-order kinetic process, and the NP attachment rate coefficient relies on NP mass transfer to the collector (sand grains) surface (known as collector efficiency or collector removal, η) and subsequent interactions (attachment efficiency, α). The NP mass flux to a collector surface is related to diffusion (for NPs <100 nm), gravitational sedimentation, and interception (for larger particles and aggregates). As a result of aggregation, the NP mass flux to a collector (i.e., collector efficiency) increases, and the NP concentration in the aqueous phase is reduced consistent with the use of the first-order mass loss term in Eq. (1a).

The calibrated model parameters for Fe-NPs transport experiment in each zone are presented in Table 3-4. The calibrated $M_{attach}^{\max}$ for all the six zones ranged from 7.5 to 9.2 mg/kg, which is within the ±95% CI of the BS attachment capacity for Fe-NPs from batch binding tests (Table B-1). The estimated attachment rate coefficient, k_a, was in the same order of magnitude and not significantly different for Zone 1 to 6 (ranged between 2.5 x 10^{-4} to 6.7 x 10^{-4} /s). Similarly, the average Fe-NP detachment rate coefficient, k_d, was within a narrow range of (0.8×10^{-6} to 6.5×10^{-6} /s) for the zones along the column. The mass transfer rate between the mobile and immobile regions for Fe-NPs (γ_{NP^-}) ranged between 0.3 x 10^{-5} to 0.6 x 10^{-5} /s except for Zone 6 where the value increased to 1.7 x 10^{-5} /s, indicating increased connectivity between the two regions in this zone, consistent with the increased water saturation in this zone.

A k_{str} value of 5 x 10^{-4} /s was required to fit the Fe-NP BTC at SP-1 where NP retention was pronounced at the top of the column (i.e., Zone 1 in B-4(a)) due to the comparatively lower initial water content (0.07 at the top probe) which likely favored straining of the Fe-NPs. Following the onset of infiltration, the water content at the top probe increased 0.22 after ~50 min and then remained steady (Figure 3-2). The Fe-NP BTC at SP-1 shows that by 100 mins the NP pulse had passed this sampler location suggesting that most retention occurred initially when more AWIs were present. This observation is consistent with the other studies that demonstrated the significant role of AWIs on NP transport and straining. Hoggan et al. (2016) observed increased retention of NPs at the top of a 1.2 m unsaturated column and attributed this retention behaviour to film straining caused by the increased capillary pressure. Similarly, Kumahor et al. (2015) reported that the NP straining observed at the top of unsaturated columns was due to NP attachment at the AWIs by the capillary forces. The calibrated first-order decay term, k_L , used for the simulation of the observed Fe-NP BTC at the effluent, and at SP-4 and SP-5 (i.e., only used for Zone 4 to 6) were nearly identical (Figure B-4(a)) and ranged from 4.3 to 5.2×10^{-5} /s.

The CoFe-NP effluent BTC was predicted reasonably well (Figure 3-4(b), Figure 3-5) with $R^2 = 0.98$, and residuals normally distributed (see Figure B-7). In addition, the set of the calibrated model parameters (Table 3-4) for the CoFe-NPs experiment using the effluent BTC as the calibration target, provided an acceptable fit to the retention profile ($R^2 = 0.86$), however, it was unable to reproduce the data collected from solution samplers. This does not indicate poor accuracy of the simulation (which agrees well with the NP retention profile as well as the CoFe-NP effluent BTC), but is instead a result of issues with the samplers which were found to clog when used with the CoFe-NPs, producing unreliable observations. Regardless of the mismatch between the observed and simulated peak concentrations of the CoFe-NPs at the sampler locations, the simulation was able to reproduce the arrival time of the observed BTCs, except at SP-6 (Figure 3-4(b)).

The calibrated $M_{attach}^{\max}$ for the crude oil zone (Zone 2) was ~3 times higher (23.6 mg/kg) than the $M_{attach}^{\max}$ for the surrounding non-impacted zones (Zones 1 and 3) (Table B-1). Consistent with the $M_{attach}^{\max}$, the calibrated attachment rate coefficient, k_a, for the CoFe-NPs in the crude oil zone (6.5×10^{-2} /s) was two-orders of magnitude greater than k_a for the non-impacted zones (for Zone 1: 4.5×10^{-4} and Zone 3: 2.3×10^{-4} /s). The calibrated detachment rate coefficient, k_d, for both the non-impacted and crude oil zones was within a narrow range (for Zone 2: 0.9×10^{-6} /s, Zones 1, 3: ~1.5×10^{-6} /s). This leads to significantly higher k_a / k_d in the crude oil zone, which represents stronger attachment to the crude oil. These findings are consistent with our previous study on the CoFe-NP transport and binding in unsaturated short column systems (Jaberi et al., 2021) which found k_a with two-orders of magnitude higher in a crude oil zone than the surrounding non-impacted zones (for oil zone: $2.8 \pm 0.15 \times 10^{-2}$ vs. non-impacted zone: $2.7 \pm 1.2 \times 10^{-4}$ /s).

Similar to the Simulation of the Fe-NP experiment, the model with k_L (2.2×10^{-5} /s) for Zone 3, provided an acceptable fit to the observed effluent CoFe-NP BTC. The particle deposition rate coefficient using in CFT, which is similar to the first-order decay rate coefficient used here, was estimated using a modified form of CFT developed for unsaturated conditions (Mitropoulou et al., 2013). The single-collector efficiency was estimated using the correlation relationship proposed by Tufenkji and Elimelech (2004) with mobile porosity used in place of total porosity (Mitropoulou et al., 2013). The estimated deposition rate coefficient (assuming a particle aggregate size of 10 to 100 times larger than individual NPs) (8.0×10^{-5} - 1.29×10^{-5} /s) was on the same order of magnitude as the first-order decay rate coefficient.

The estimated k_{str} was 0.8×10^{-4} /s, which is close to the k_{str} for the Fe-NPs in the transport experiment and on the same order of magnitude as our previous work used the same coated CoFe-NPs (Jaberi et al., 2021). Generally, the CoFe-NPs are more susceptible to aggregation compared to Fe-NPs due to their lower polymer coating concentration. Therefore, for the CoFe-NPs, the k_{str} may encompass a combination of aggregation and possible irreversible attachment at the AWIs near the column inlet. NP aggregation close to the injection point or column inlet has been previously reported (for example: Kasel et al., 2013; Liang et al., 2013a,b; Rahmantpour et al., 2018). Degenkolb et al. (2019) studied the transport of polyacrylic acid- and humic acid-coated CeO_2 NPs in a natural porous medium and reported that the majority of NPs retained in the first few centimeters of the columns, even though the size of the NPs was below the straining threshold. Recently, in another study under saturated conditions (Linley et al., 2021), we observed an exponential shape retention profile for CoFe-NPs (coated with 1 g/L Pluronic) in 25-cm long columns, with the highest retention near the inlet. This retention behaviour was attributed to irreversible NP attachment through adsoption of Pluronic coating to mineral materials and physical straining caused by aggregation mechanisms.

Aside from the straining and reversible attachment mechanisms, a non-linear, non-monotonic relationship between media surface roughness and particle deposition flux has been reported for favourable and unfavourable deposition conditions (i.e., suspension medium ionic strengths) (Jin et al., 2015, 2017; Torkzaban and Bradford, 2016). The secondary energy minimum alone was found to be inadequate to explain the observed particle deposition behavior because surface roughness and ionic strength affect particle deposition concurrently in a manner that is not simply additive as particle deposition rates are highly correlated with inverse Debye-Hückel length (Jin et al., 2017). Recent work has shown that detachment tends to occur at protruding roughness asperities (Li et al., 2020). While all of these mechanisms merit consideration, such mechanistic evaluation was beyond the scope of the present investigation.

3.4 Conclusions

The transport and binding properties of Pluronic coated NPs were investigated through a series of experiments in a 1.4-m long unsaturated column. Initially the transport of Fe-NPs coated with a higher polymer concentration was evaluated in this system, and then NP targeted binding to a crude oil source zone was explored using NPs coated with a lower polymer concentration (CoFe-NPs). Results indicated that the CoFe-NPs experienced substantial retention in the crude oil zone as demonstrated by: (1) low mass recovery, (2) delayed CoFe-NP arrival and suppressed peak concentrations relative to the Br^- BTCs, and (3) CoFe-NP retention profile coincident with the TPH distribution.

Data collected at various locations along the column for the in Fe-NP transport experiment showed that the arrival time of the center of mass of the Fe-NP BTCs compared to their respective Br^- BTC was essentially identical at the top three samplers (i.e., from top to the middle of the column), while gradually increasing as the NP solution migrated down the column. For both NP experiments, the NP BTC peak concentration and tailing diverged from the Br$^-$ BTCs as the NPs moved deeper in the column. Collectively, these observations are reflective of consistent NP retention as the solution migrated down the column, and perhaps some NP mass loss due to aggregation and subsequent trapping. This aggregation was attributed to possible gradual dissociation of NP coating material due to contact with the sediments.

The experimental BTCs were successfully described using a model that considers Br$^-$ and NP transport in both mobile and immobile regions. An attachment/detachment model with nonlinear Langmuirian blocking including a depth-dependent straining and mass loss term was required to represent the observed NP retention. The exponential shape of the retention profile for the top few centimeters of the column was an indication of straining and addressed by the depth-dependent straining term. Comparatively lower initial water content, correlated with the higher air–water interfacial area and lower available mobile regions for NP transport, favored straining or film straining for both the Fe-NPs and CoFe-NPs near the top of the column. In addition to the role of water content on the straining process, the high retention of CoFe-NPs at the top of the column was presumably due to aggregation as a result of the lower polymer coating concentration used. A first-order mass loss term captured the additional NP mass removed from the aqueous phase due to the suspected aggregation and subsequent trapping that occurred as the NPs moved deeper in the column system. This aggregation behaviour was not observed for these NPs in the short column systems where a simple attachment/detachment model with a nonlinear Langmuirian blocking (including the straining term for CoFe-NPs) was sufficient to describe NP retention behaviour (Jaberi et al., 2021; Linley et 2019b).

The estimated $M_{attach}^{\max}$ for the crude oil zone was ~3 times higher than the $M_{attach}^{\max}$ for the non-impacted zones which is reflective of the shape of CoFe-NP retention profile. Consistent with $M_{attach}^{\max}$, the estimated k_a was about two-orders of magnitude higher for the crude oil zone than the k_a for the non-impacted zones, demonstrating preferential binding of CoFe-NPs to the crude oil. In contrast, the estimated k_d for both zones were nearly identical giving rise to a significantly higher ratio of k_a to k_d implying stronger attachment of CoFe-NPs to the crude oil zone compared to the non-impacted sands.

Results from this study extend our knowledge of the transport and targeted binding of amphiphilic co-polymer coated NPs at a spatial scale representative of the unsaturated zone above a shallow aquifer. Preferential binding of CoFe-NPs to crude oil was demonstrated under unsaturated conditions as designed. However, it was found that in addition to reversible attachment processes and straining, the NPs experienced additional retention and trapping possibly due to increased contact with sediments and aggregation during longer travel distance. This may pose a major challenge for the delivery of these NPs to a target contaminated source zone far from the injection location which is important to consider for designing field delivery systems. Hence, prior to field trials, additional investigation is required on the retention behaviour and aggregation of these NPs at larger spatial scales or in multidimensional systems representative of near field conditions.

3.5 Acknowledgements

This research was financially supported by Chevron Energy Technology Company. The authors would like to thank Terry Ridgway and Mark Sobon for the assembly and construction of experimental apparatus and Felipe Solano, Shirley Chatten, and Mark Merlau for their technical assistance. We also acknowledge Canadian Centre for Electron Microscopy (CCEM) for providing the TEM images of CoFe-NPs.

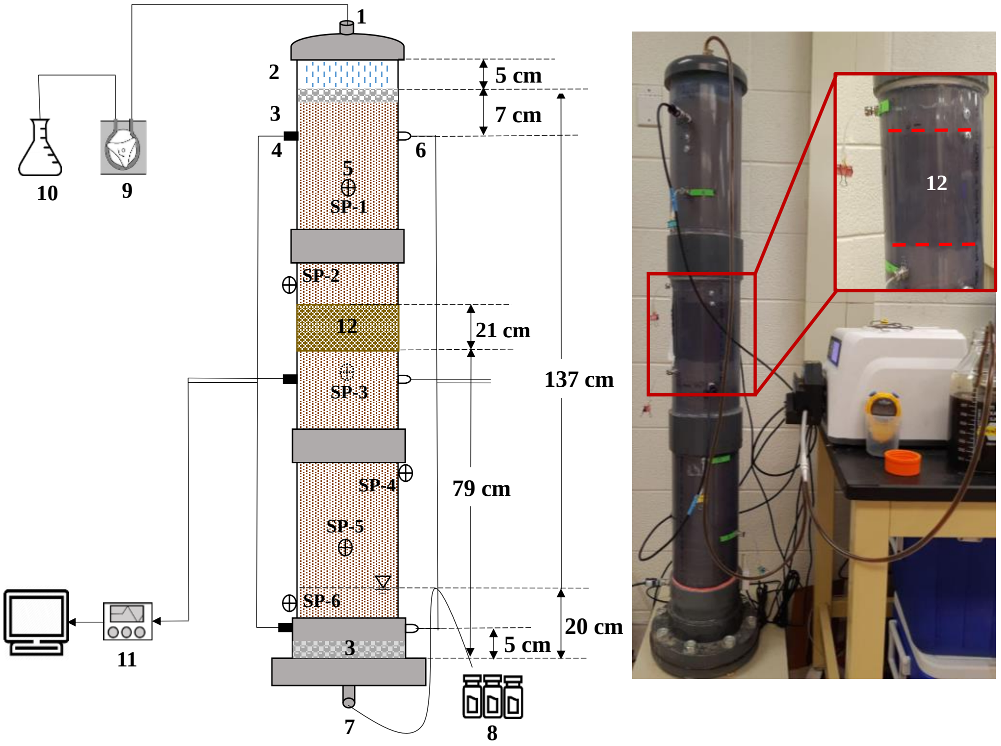

Figure 3-1. Schematic of column set-up (left) and image of the column packed with the crude-oil source zone (right). Not to scale. Key: 1. Inlet, 2. Perforated plate, 3. Glass beads, 4. Tensiometer probes (T5), 5. Solution samplers (SP-1 to SP-6), 6. Moisture probes (GS-1), 7. Outlet, 8. Sampling vials, 9. Peristaltic pump, 10. Injection solution, 11. Data logger, and 12. Crude oil source zone for binding experiment.

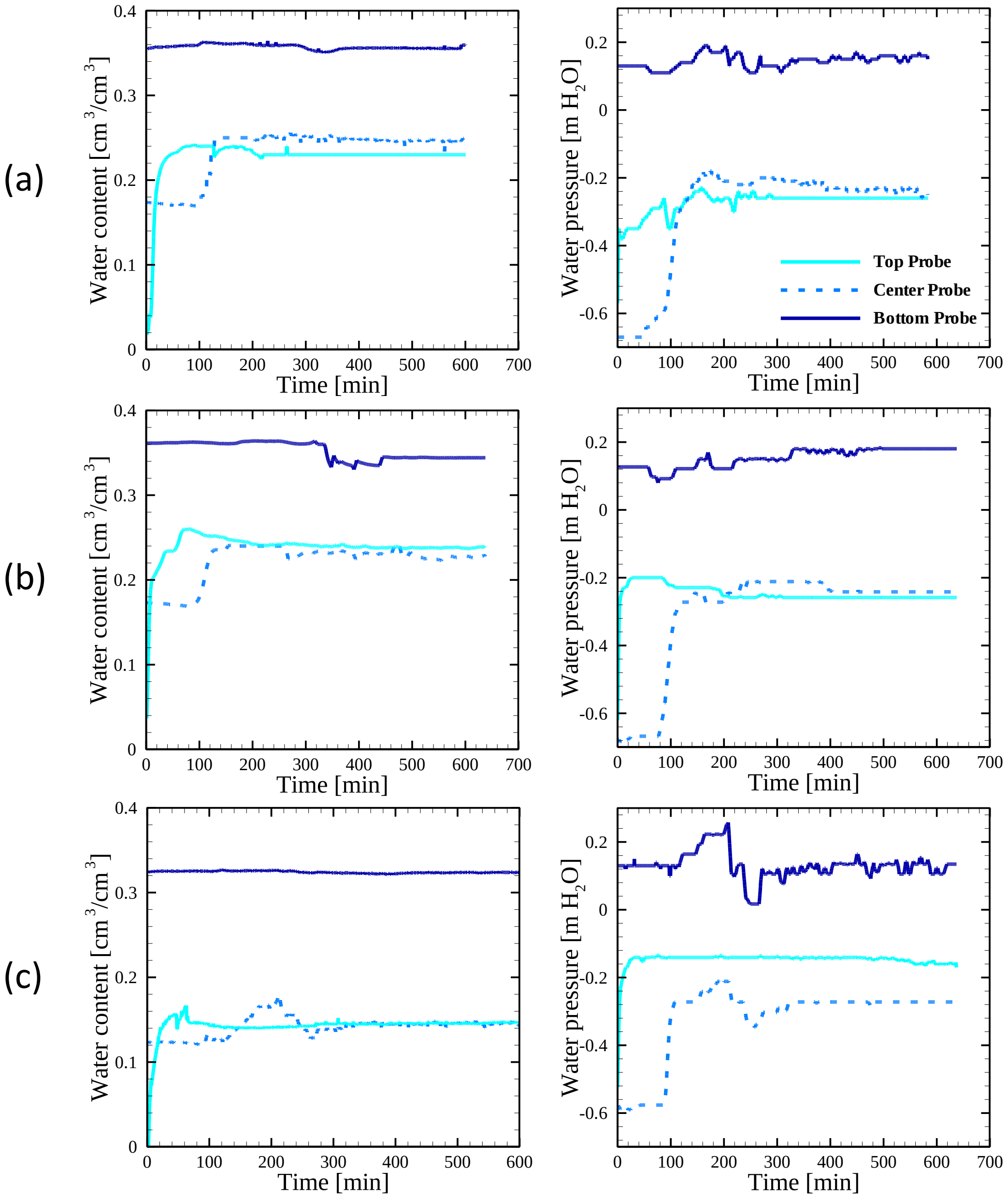

Figure 3-2. Volumetric water content and water pressure data from (a) tracer experiment, (b) Fe-NP transport experiment, and (c) CoFe-NP transport and binding experiment.

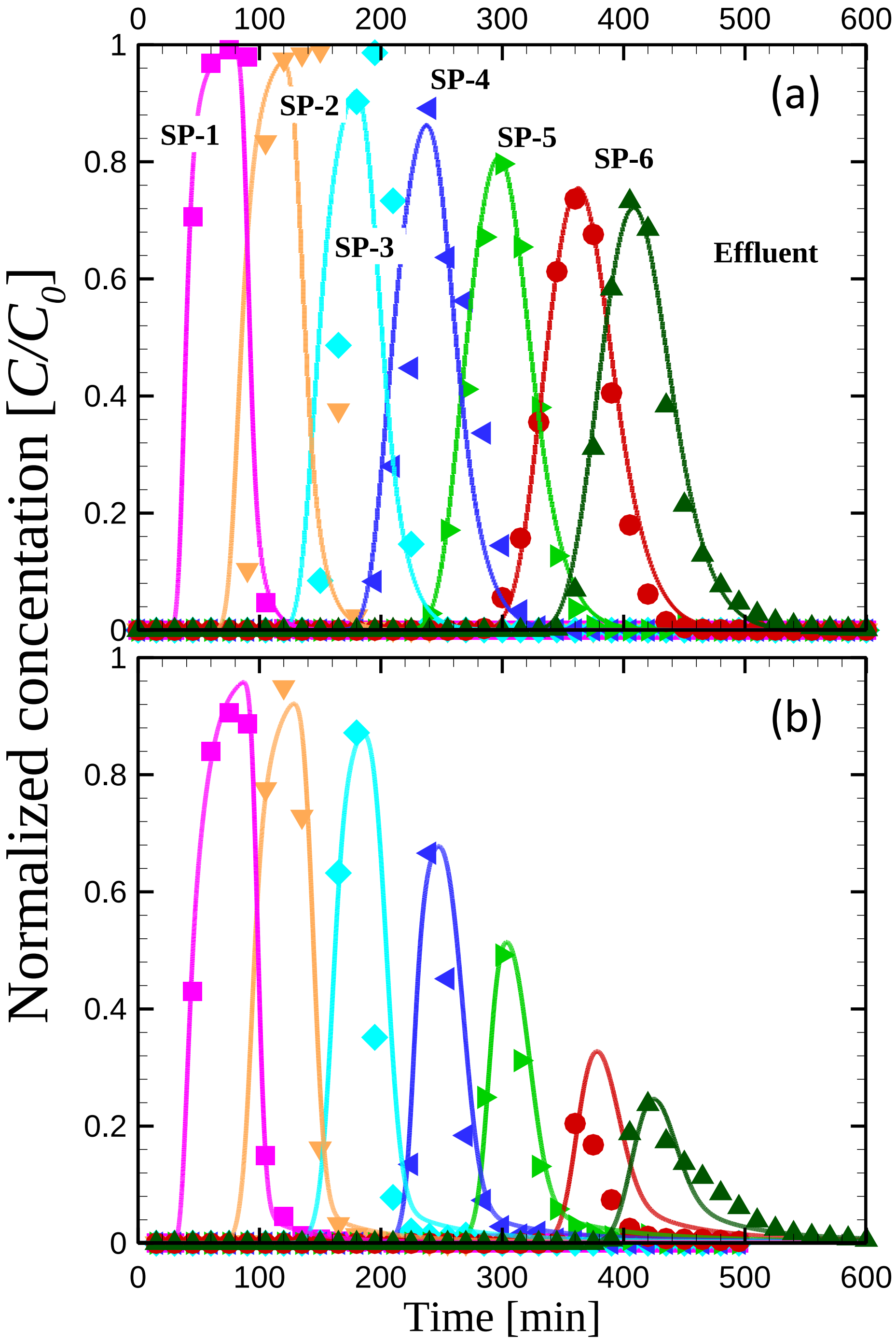

Figure 3-3. Observed (symbols) and simulated (solid lines) normalized BTCs for (a) Br^-, and (b) Fe-NPs at the solution samplers (SP-1 to SP-6) and column effluent for the tracer and Fe-NP transport experiments. Fe-NP infiltration concentration of 1000 mg/L (dosage of 1000 mg), and flowrate of 20 mL/min.

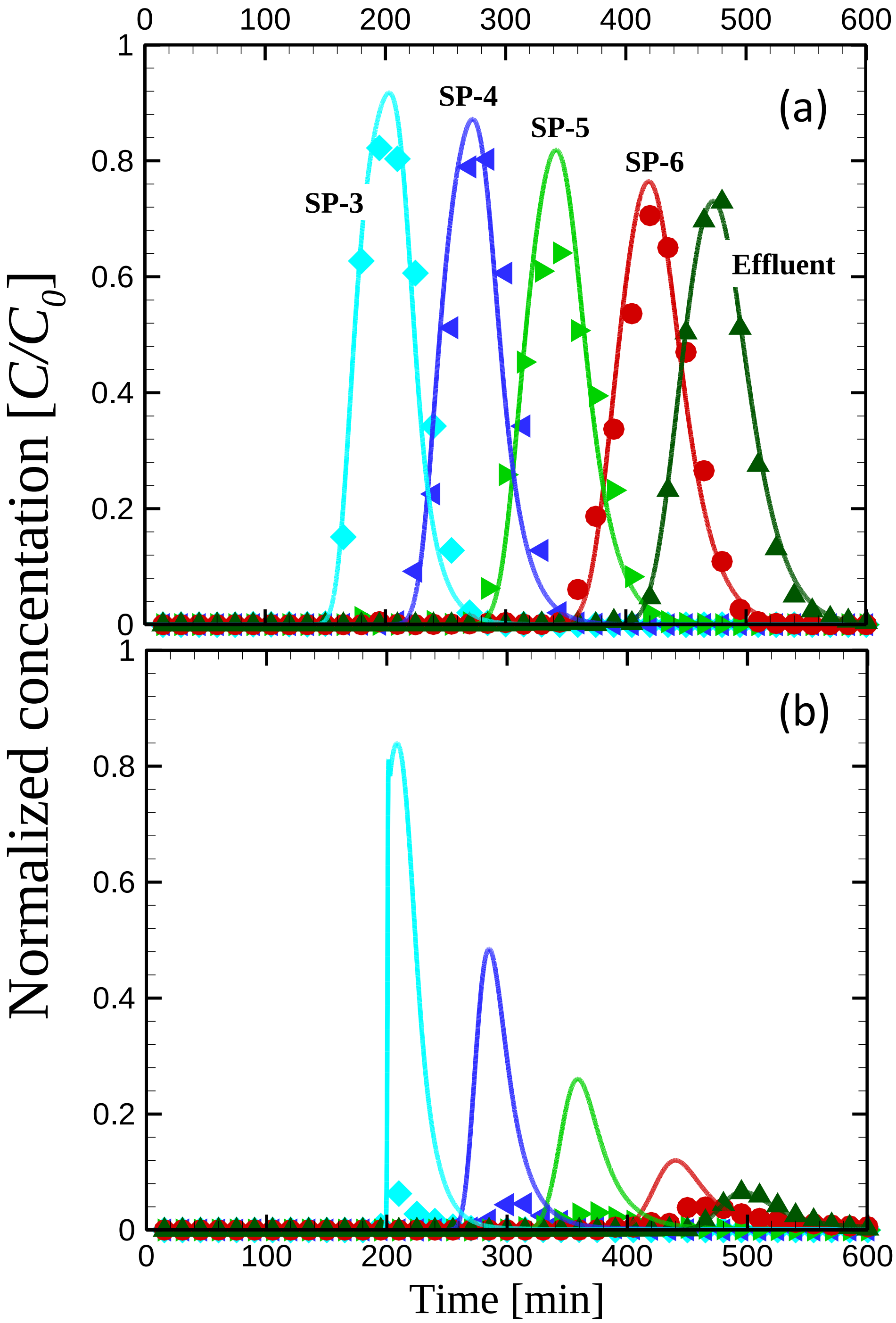

Figure 3-4. Observed (symbols) and simulated (solid lines) normalized BTCs for (a) Br^- and (b) CoFe-NPs at solution samplers (SP-3 to SP-6) and column effluent during transport and binding experiment. Infiltration CoFe-NP concentration of 500 mg/L (dosage of 500 mg), and flowrate of 15 mL/min were used. No data are available for the two samplers at the top of the column (SP-1 and SP-2) due to clogging.

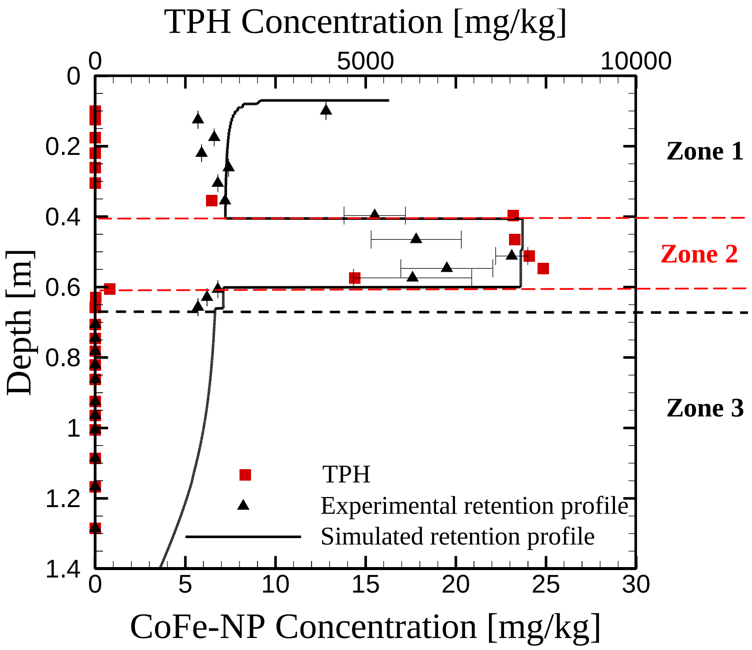

Figure 3-5. Observed (symbols) and simulated (solid line) CoFe-NP retention profile and TPH concentration (mg TPH/ kg dry sediment) in the oil-impacted column. Error bars represent the standard deviation of five subsamples in each layer. Target input concentration of CoFe-NP was 500 mg/L (target input dosage of 500 mg/L) was used. Injection flowrate was 15 mL/min. Zone 1 is the non-impacted BS (from 0.74 to 0.8 m and 1.0 to 1.37 m), Zone 2 is the crude oil BS, and Zone 3 is the non-impacted BS. Zone 3 had been exposed to Fe-NPs from the previous experiment.

Table 3-1. Summary of operating conditions for the tracer, transport and binding experiments.

Exp. ID	Injection solution	Packing material	Initial saturation	Q [mL/min]	C_{inj} [mg/L]	V_{pulse} [mL]	Dose [mg]
Tracer	NaBr	Non-Impacted	Drained[1]	20.0	1000	1000	1000
Transport	Fe-NPs	Non-Impacted	Drained	20.0	1000	1000	1000
Binding	CoFe-NPs+NaBr	Impacted[3]	unsaturated[2]	15.0	500	1000	500

1. Drained: Column was gravity-drained after saturation
2. Unsaturated: Column was packed with moist sediment, except for the zone below the impacted zone
3. Impacted: Column packed with crude oil-impacted and non-impacted sediment

Table 3-2. BTC metrics for Br^-, Fe-NPs and CoFe-NPs.

Exp. ID	Tracer			NP				
	M_R [%]	T_{peak} [min]	T_c^{Br} [4] [min]	M_R[1] [%]	$C^{MB}_{retained}$ [2] [mg/kg]	T_{peak} [3] [min]	T_c^{NP} [4] [min]	T_c^{NP}/T_c^{Br} [-]
Tracer	99	405	416	--	--	--	--	--
Transport	--	--	--	30	13.8	420	451	1.08
Binding	96	480	477	9	22.2	495	529	1.11

1. M_R is percent of injected mass recovered.
2. T_{peak} is the time to the peak of the BTC.
3. T_c is the time to the center of the mass of Br^- or NP BTC.
4. $C^{MB}_{retained}$ is mass of NPs retained per mass of dry sediment based on mass balance.

Table 3-3. Calibrated transport model parameters from tracer data.

Exp. ID	Zone ID[1]	α_L [m]×10^{-3}	ϕ_m [-]	ϕ_{im} [-]	ϕ_T [-]	γ_{Br} [1/s] ×10^{-5}	R^2
Tracer	--	1.0	0.30	0.02	0.32	3.9	0.97
Binding	1	0.7	0.26	0.01	0.27	2.0	0.99
	2	0.2	0.27	0.01	0.28	1.8	
	3	1.0	0.27	0.01	0.28	2.0	

1. Zone ID: 2 is the crude oil zone; 1 is the non-impacted BS packed above and just below the oil zone; and 3 is the non-impacted BS below Zone 1 and 2. See Figure B-4(b) for the location of each zone.

Table 3-4. Calibrated NP model parameters for the Fe-NP and CoFe-NP transport experiments.

Exp. ID	Zone ID[1]	Calibration Target BTC	f_s	γ_{NP}	$M_{attach}^{\max}$	k_a	k_d	k_L	k_{str}	R^2
			[-]	[1/s]× 10^{-5}	[mg/kg]	[1/s]× 10^{-4}	[1/s]× 10^{-6}	[1/s]× 10^{-5}	[1/s]× 10^{-4}	
Transport	1	SP-1	0.94	0.6	9.2	3.0	1.8	--	1.5	0.99
	2	SP-2		0.3	8.8	4.1	0.8	--		0.95
	3	SP-3		0.3	8.4	6.3	0.8	--		0.84
	4	SP-4		0.5	7.5	6.1	1.5	5.1		0.85
	5	SP-5		0.5	8.6	6.7	3.6	5.2		0.82
	6	Effluent		1.7	8.7	2.5	6.5	4.3		0.89
Binding	1	Effluent	0.95	1.9	7.4	4.5	2.1	--	0.8	0.98
	2		0.96	2.3	23.6	649	0.9	--		
	3		0.96	1.1	6.5	2.3	1.0	2.2		

1. Zone ID: The column was discretized into different zones for model simulation. See Figure B-4 for the location of each zone along the domain.

Chapter 4

Targeted Delivery of Nanoparticles to Crude Oil: An Unsaturated Physical Model Experiment

Abstract

In situ targeted delivery of engineered nanoparticles (NPs) has gained significant attention for offering efficient delivery of the NPs throughout a target treatment zone whilst decrease the required mass of NPs to achieve treatment goals. Amphiphilic co-polymer coated NPs have been recently proposed as an effective reagents to target non-aqueous phase liquid (NAPL) under saturated and unsaturated conditions. However all investigation has been conducted in one-dimensional systems which cannot represent the field scale complexity under multidimensional domain (e.g., heterogeneity). In this study, the capability of these NPs to bind to a heterogeneous crude oil source zone was evaluated in a less constrained unsaturated system using a two dimensional (2-D) physical model. The NP transport and retention behaviour in the 2-D system was characterized using a single porosity transport model with depth-dependent straining and kinetic attachment/detachment reactions. Preferential attachment of NPs to the crude oil source zone was demonstrated, however, significant retention of NPs was also observed between the infiltration gallery and the top of the crude oil zone as a result of straining and possible aggregation. In addition, the presence of preferential flow paths reduced the delivery efficiency into the segments of the crude oil zone with higher oil saturation and thickness, where NPs had lower accessibility and interaction with the oil phase due to the lower permeability of water flow to this zone. Results from the model simulations provided acceptable fits with the experimental observations. This study revealed the significant role of physical heterogeneity (such as permeability and water content) on NPs transport and binding behaviour that should be considered in the design of potential NP delivery strategies for targeting source zones in similar systems.

4.1 Introduction

In situ remediation has become a preferred treatment strategy for contaminated sites owing to lower costs and less environmentally disruptive modes of deployment (Kuppusamy et al., 2016). A critical function of any *in situ* remedial technology is its ability to treat the target treatment zone while avoiding delivery of reagents into other areas (Bishop et al., 2010; Elliot and Zhang, 2001; Schrick et al., 2004). The concept of targeted delivery has gained significant attention over the past two decades in the field of nanoremediation which focuses on the design of nanoparticles (NPs) with the ability to selectively attach to specific target contaminants (e.g., Bishop et al., 2010; Linley et al., 2019; Saleh et al., 2007). Accumulation of NPs within the target treatment zone may increase treatment efficiency and reduce the environmental risk of unwanted NP migration (Linley et al., 2019; Phenrat et al., 2011).

Targeted binding of NPs to non-aqueous phase liquids (NAPLs) was first demonstrated by Saleh et al. (2005) using nano zero-valent iron (nZVI) particles coated with a tri-block copolymer of poly(methacrylic acid)-block-poly(methyl methacrylate)-block-poly(styrene sulfonate) (PMAA-PMMA-PSS). They reported that the PMAA block anchored the polymer to the NP surface through strong physiosorption between carboxylic acids and the outer iron oxide layer of the particle. The PMMA block provided a low-polarity region with an affinity towards the NAPL, and the PSS block served to stabilize the NPs in water through electrosteric interactions. Similarly, Phenrat et al. (2011) reported successful NAPL targeting using polymer modified nZVI in a 2-D physical model (30 cm long x 18 cm high x 2.5 cm wide). They observed that the mass of NPs bound in the NAPL zone directly correlated with NAPL saturation as it controls the available NAPL/water interfacial area. Recently, we reported targeted binding of Pluronic-coated NPs towards NAPL (i.e., crude oil) under saturated conditions (Linley, 2019; Linley et al., 2020a,b) by adding a tunable amphiphilic co-polymer coating (Pluronic) to the surface of NPs which enhanced the hydrophobic interactions with the NAPL as well as ensured mobility. Results demonstrated that the attachment of these NPs to crude oil increased by decreasing the polymer coating concentration, increasing the NAPL concentration, and increasing temperature. The targeted binding capability of these Pluronic-coated NPs in unsaturated conditions was demonstrated using 15-cm long columns and a 1.4-m long lysimeter (Jaberi et al., 2021a,b).

The transport of NPs has been found to directly correlate with water saturation (e.g., Bradford et al., 2002; Torkzaban et al., 2008; Wan and Wilson, 1994). In saturated media, all the pores are filled with water and NP retention is limited to pore straining (i.e., physical trapping of NPs in pores and pore throats) and attachment at solid-water interfaces (SWIs), while in unsaturated media where air phase is present, additional retention occurs at air-water interfaces (AWI), solid-water-air (AWS) interfaces (Bradford et al., 2003), and thin water films formed around air-filled pores or sediments (film straining) (Wan and Wilson, 1994). In unsaturated porous media the spatial and temporal distribution of water saturation controls the transport of NPs. Straining may be affected by other physical factors such as water velocity, sediment grain size distribution, heterogeneity, and dimensionality (Bradford et al., 2002). Kasel et al. (2013) investigated the transport and retention of multi-walled carbon nanotubes in partially saturated columns (3 cm ID x 12 cm long) and a lysimeter (4 cm ID x 115 cm long), and found that NP retention was enhanced at lower water saturation due to increased air-water interfacial area. Similarly, Hoggan et al. (2016) investigated the transport and retention of titanium dioxide (TiO_2) NPs in long columns (2.5 cm ID x 120 cm long) under saturated and unsaturated conditions and observed that the retention of NPs was significantly higher in the unsaturated columns. They also found that retention directly correlated with elevation due to higher capillary pressures at the top of the column which reduced the thickness of water films on sand grains and increased film straining. Chen et al. (2008) also reported higher retention of TiO_2 NPs at lower water saturations corresponding to film straining, and Yecheskel et al. (2018) observed higher retention of silver NPs with lower water saturation due to more AWIs present. In our previous work (Jaberi et al., 2021) we found that the retention of Pluronic-coated iron oxide NPs increased with decreasing initial water saturation in column systems. The average recovery of the NP injected mass was 83% and 76% from 15-cm saturated and unsaturated sand columns, while only 25% from the initially dry columns. As water saturation is correlated with the magnitude of AWIs, this behaviour was attributed to the increased quantity of AWIs and immobile regions such as AWS interfaces. Consistently, NP retention increased in the unsaturated columns at a lower injection flowrate due to an increase in both the residence time and comparatively more AWIs.

The majority of studies exploring NP transport and retention behaviour have primarily used column experiments which do not mimic field conditions because they are not multidimensional (Mondal et al. 2021). NPs may encounter physical heterogeneities that cannot be captured in column experiments, and these heterogeneities can substantially affect the ability of the NPs to contact a source zone and ultimately decrease treatment efficiency (Phenrat et al., 2010, 2011). Therefore, prior to field-scale trials, representative multidimensional systems should be used to explore the transport and binding of NPs and support the design of pilot-scale investigations. Information gathered from these experiments are invaluable for scale-up to field applications.

Multidimensional physical models have been used to understand *in situ* delivery and transport behaviour of various reagents (e.g., Kambhu et al., 2021; MacKinnon and Thomson, 2002; Velimirovic et al., 2020). The few investigations that have reported on the transport behaviour of NPs in two-dimensional (2-D) systems have all been conducted under saturated conditions with nZVI used exclusively. For example, Busch et al. (2014) investigated the transport of nZVI in a saturated 2-D physical model (100 cm long x 40 cm high x 5 cm wide) and reported that nZVI attachment occurred in the first few centimetres near the injection point, resulting in lower recovered mass from the 2-D system compared to columns. Phenrat et al. (2010) investigated the impact of porous media heterogeneity and NP input concentration on the transport of modified-nZVI in a 2-D physical model (30 cm long x 18 cm high x 2.5 cm wide) packed with fine, medium and coarse sand (d_{50} = 99, 330, and 880 μm, respectively) and showed that heterogeneity had a significant impact on nZVI retention. They observed that much of the nZVI particles migrated through the coarser sand layer (higher conductivity) bypassing the finer sand layer. Similarly, Li et al. (2016) investigated CMC-nZVI transport in a 2-D system (sand tank) (70 cm long x 18 cm high x 2.5 cm wide) and observed preferential migration through coarser sand. Kanel et al. (2008) used a 2-D physical model (50 cm long x 28.5 cm high x 2 cm wide) to study the transport of stabilized nZVI in silica beads (d_{50} = 1.1 mm) under steady flow conditions. Their results illustrated the influence of density driven advection on NP transport which could not be captured in column experiments. Mondal et al. (2018) investigated the effects of injection flow rate and CMC concentration on nZVI transport in a 2-D porous medium system (55cm long x 45 cm high x 1.3 cm wide) wet-packed with silica sand. They found that increasing flow rate decreased nZVI attachment efficiency corresponding to longer travel distances. Darko-Kagya and Reddy (2011) investigated the transport of iron NPs in homogeneous and heterogeneous porous media in a 2-D system, and observed non-uniform spatial distribution of retained NPs due to aggregation and sedimentation as well as an increase in retention near the injection point. While these multidimensional studies provide valuable information related to NP transport in saturated conditions, the transport and binding behaviour in 2-D unsaturated systems remains unexplored.

Our previous studies on the transport and binding of Pluronic-coated NPs in small and large 1-D systems under saturated and unsaturated conditions demonstrated that targeted-delivery of these NPs to crude oil is possible. Collectively, these efforts contributed to our understanding of the application conditions required for efficient targeting which will aid in the design of potential delivery strategies (Linley et al 2019, 2020a,b; Jaberi et al., 2021a,b). However, investigation of the transport and binding of these NPs in a less physically constrained unsaturated system is a critical next step to expand our knowledge of the behaviour of these NPs in more realistic conditions. The objective of this study was to assess the capability of amphiphilic co-polymer coated NPs to bind to a heterogeneous crude oil source zone. To generate the necessary data, a NP transport experiment was performed in an unsaturated 2-D physical model (sand tank) containing a heterogeneous crude oil source zone. An infiltration gallery was used to deliver the NPs into the sand tank to mimic a potential field delivery method. HYDRUS 2-D (Šimůnek et al., 1999) was used to support the experimental observations and characterize the unsaturated transport and binding of these NPs.

4.2 Materials & Methods

4.2.1 Materials

Cobalt ferrite NPs (CoFe-NPs) used in this work were prepared as described by Linley (2019). These NPs are comprised of a three-layer hierarchical sphere with a core of cobalt ferrite, a middle layer of oleic acid, and an outer layer of a Pluronic block co-polymer (P104, L62) (poly (ethylene oxide)-poly (propylene oxide)-poly (ethylene oxide) (PEO-PPO-PEO)). NPs were prepared using solvothermal decomposition of iron and cobalt oleates at 180 °C in a stainless steel autoclave, then washed 3 times with ethanol, and dried under flowing air. A 2.5 g/L Pluronic solution (2 g/L L62 and 0.5 g/L P104) was used to coat the CoFe-NPs. A Transmission Electron Microscopy (TEM) image of the NPs is presented in Appendix C (Figure C-1).

Crude oil (sour crude, API gravity 13.3 (density of 0.977 g/cm^3), average linear carbon number of 25.1, kinematic viscosity 4.75 x 10^{-4} m^2/s at 40 °C) was provided by Chevron Energy Technology Company (Houston, TX, USA). Sodium bromide (NaBr, ACS grade, ≥ 99%), dichloromethane (DCM, > 99.9 %), hydrogen peroxide (H_2O_2, 30%), hydrochloric acid (HCl, ACS grade, 37%), ethanol (ACS grade, 99%), hexane (ACS Grade, >98.5%), and nitric acid (HNO_3, ACS grade, 70%) were purchased from Fisher Scientific. Iron (III) nitrate nonahydrate ($Fe(NO_3)_3{\cdot}9H_2O$, ACS grade, > 98%), cobalt (II) nitrate ($Co(NO_3)_2{\cdot}6H_2O$, ACS grade, > 98%), oleic acid (>90%), sodium oleate (> 90% fatty acids (as oleic acid) basis), sodium hydroxide (NaOH, ACS grade, > 98%), and 1-pentanol (ReagentPlus® grade, >99%) were purchased from Sigma Aldrich. Pluronic co-polymers P104 and L62 were gifted by BASF, Canada. All chemicals were used as received. Millipore water was obtained from a direct water purification system (EMD Millipore, 18.2 MΩ·cm at 25 °C).

Sandy aquifer material (denoted here as “Borden Sand” (BS)) (d_{10} of 75 µm) with 2 % gravel, 92 % sand, 5.9 % silt, and 0.1 % clay was collected from 1 m below ground surface (bgs) at the University of Waterloo Groundwater Research Facility at the Canadian Force Base (CFB) Borden, ON, Canada. BS is comprised of mostly quartz, amphiboles, and carbonates with minor amounts of other minerals, and has a total iron content of 1 % wt (29.6 g/kg) (Ball et al. 1990). Prior to use, the BS was sieved (1 mm mesh) to remove larger particles, repeatedly rinsed with Millipore water until the filtrate ran clear, and oven-dried at 90 °C overnight. The sediments were stored in sealed bags at 4°C until used.

4.2.2 Physical model experiments

A sand tank (90 cm long x 50 cm high x 10 cm wide) was used in this study to investigate the vertical transport and retention behaviour of NPs in an unsaturated porous medium (Figure 4-1). The width of the sand tank provided easy access for packing, and minimized possible wall effects (MacKinnon and Thomson, 2002). The sand tank shell was constructed of 4-mm thick stainless steel except for the front which was made of clear 5-mm thick Plexiglas to allow for visualization of the packed medium. To control the water table elevation, a 5-cm wide chamber at each end of the sand tank was filled with glass beads (4 mm, Fisher Scientific) and separated from the packed medium by a stainless steel perforated plate (1-mm openings with 50% open area) wrapped with nylon filter cloth (75 µm). The bottom of the sand tank sloped (8.8%) from the side walls to a central outlet opening (2 cm ID) connected to a 6.35-mm diameter tubing (outlet tube) using a brass valve (1.3 cm NPT tube fitting). A stainless steel screen (75 µm) was secured over the outlet opening to retain the packed materials. Twenty-three sampling ports (0.3 cm Swagelok stainless steel fittings) (denoted as SP-1 to SP-23) lined with Teflon septa were distributed on the back of the sand tank for the collection of (tracer and NP) aqueous samples (Figure C-2).

The sand tank was packed using two methods. The lower 20 cm of the sand tank was wet-packed using ~4-cm thick lifts. Each lift was compacted using a 5-cm diameter rod, and then the surface was scraped with an abrasive brush before addition of the next lift to minimize heterogeneous layering. The remaining 30 cm of the sand tank was packed using BS mixed with Millipore water (water content of ~0.2 v/v) so that the heterogeneous crude oil source zone could be constructed as shown in Figure 4-2. Sediment material for the crude oil source zone was comprised of moist BS mixed with 2 % or 4% wt. crude oil heated to 60 °C and homogenized by stirring. The source zone was an irregular shape (~45 cm long by ~11 cm high) with two distinct lobes and composed almost entirely of the 2% wt. crude oil sediment. The central lobe contained a circular core of the 4% wt. crude oil sediment. Packing was conducted using 2-cm thick lifts of either the moist BS or crude oil sediment as required, carefully compacted using the rod, leveled, and then the surface gently scraped with the brush. After packing, the water level at the outlet was raised to the top of the packed porous medium zone and then lowered to 2 cm from the bottom of the sand tank, and the system was allowed to gravity drain for at least 48 hrs to achieve an initial unsaturated condition.

To allow for even release of solutions into the unsaturated system, an infiltration gallery, comprising a ~6-cm thick layer of glass beads (4 mm, Fisher Scientific), and an infiltration system were emplaced at the top of the sand tank (Figure 4-2). The infiltration system, which was embedded in the glass beads, was made from twelve pieces of flexible PVC tubing (1.27 cm ID, 7.2 cm length, Fisher Scientific) with ~1-mm openings drilled at 1-cm increments along the length of each tube (Figure C-3). One end of each tube was sealed, and the other end attached to a 3.2-mm diameter tubing (inlet) using a PVC insert fitting (1 cm ID).

Each inlet tube was connected to one of two peristaltic pumps (Cole Parmer, MasterFlex 7535-04), each equipped with 3 heads.

Two experiments were performed in the sand tank: (1) a conservative tracer experiment to characterize the hydraulic and transport properties of the porous medium, and (2) a CoFe-NP experiment to explore the transport and binding behaviour of NP in heterogenous media. All experiments were conducted at room temperature (~22 ºC).

For the tracer experiment, sodium bromide (NaBr) was added to ~750 mL of a diluted water-soluble food dye (red No. 40) to reach a Br^- concentration of ~ 200 mg/L, and the solution was infiltrated at a constant rate of ~35 mL/min for ~12 minutes followed by Millipore water at the same flowrate until red dye was no longer visible through the front Plexiglas wall (~650 min). Effluent samples were collected from the outlet tube (maintained at 2 cm from the bottom of the tank) every 15 minutes in 40 mL glass vials (VWR, Mississauga, ON, Canada). The sample filling time was used to estimate the effluent flow rate. Aqueous samples were manually collected from each sampling port approximately every 15 minutes) using a 3-mL syringe with hypodermic needle (point style #2, 22 gauge, length 5 cm) and transferred into 5-mL polypropylene cryogenic vials (VWR, Mississauga, ON, Canada). The sampling volume rate (due to clogging of some ports, approximately a total of 2% of volume was being extracted each time) had no significant impact on the flow field and concentration of tracer/NP in the effluent. The temporal dye distribution as displayed on the front Plexiglas wall was monitored using a digital camera (Nikon D7100 fitted with a Nikon VR DX 18-200 mm lens) at a resolution of 4496 x 3000 pixels every 15 min. To minimize the effect of ambient light and unwanted reflections, the front of the sand tank and camera were covered with a white screen photography background cloth (2 m x 1.5 m). The images were handled using an image processing software (GIMP 2.10.18).

The CoFe-NP experiment involved infiltration of ~600 mL of the CoFe-NP solution (cobalt target concentration of 400 mg/L) followed by Millipore water at the same flowrate (35 mL/min) for a total duration of ~650 min. To quantitatively investigate the spatial distribution of the NP concentration within the sand tank, aqueous samples were collected from each sampling port using a syringe every 30 minutes in 3-mL polypropylene cryogenic vials. Effluent samples were collected every 30 minutes in 40 mL glass vials.

At the end of the NP transport and binding experiment, the porous medium in the sand tank was carefully excavated (from top to bottom) to determine the spatial distribution of the retained CoFe-NPs. Subsamples were collected using custom made stainless-steel cylinders (3-cm ID, and 1 or 2 cm deep) from specific locations in rows from the front, center, and back of the sand tank as shown in Figure C-4. 1-cm deep subsamples were collected from a rectangular box surrounding the crude oil zone, and 2-cm deep subsamples collected elsewhere. The cylinder was placed on the exposed surface at each location and gently advanced with a rubber hammer. Once all cylinders were in place for a specific excavated depth, the surrounding material was carefully removed and each subsample was transferred to a 40-mL glass jar (VWR, Mississauga, ON, Canada) and stored at 4°C (Figure C-4). A total 432 subsamples were collected. In addition, 10-g subsamples were collected from the sediment remnants of the 2% and 4% crude oil zones, and stored in 40-mL glass jars prior to total petroleum hydrocarbon (TPH) analysis.

The mass of the NPs that can be attached to clean or crude oil impacted BS (S_{max}) was estimated from batch binding tests (see C.2 for details). The estimated S_{max} value was 8.2 ± 0.6 mg/kg for BS, 25.9 ± 2.1 mg/kg for 2% crude oil impacted BS, and 29.5 ± 2.4 for 4% crude oil impacted BS (Table C-1).

4.2.3 Analyses

The total cobalt concentration (Co_T) in aqueous samples (assuming that the core material was 100 % composed of $CoFe_2O_4$) was quantified by Inductively Coupled Plasma Optical Emission Spectrometry (ICP-OES; Teledyne Leeman Laboratories). Prior to ICP-OES analysis, an aliquot of the aqueous sample (1 mL) was digested with 0.2 mL of 12.1 mol/L HCl solution (37 %) to dissolve the NPs, then diluted to a total volume of 10 mL with 0.1 mol/L HCl (method detection limit (MDL) of 0.004 mg/L for Co; corresponds to 0.04 mg-Co/kg dry sediment). The concentration of aqueous Br^- was measured using ion chromatography (Dionex ICS-1100) with a MDL of 0.5 mg/L. The concentration of CoFe-NPs retained in sediment subsamples (mg of Co/kg of dry sediment) was estimated using solid digestion of the sediment subsamples excavated (EPA Method 3050b) followed by ICP-OES analyses (see C.1 for details). The results from the digestion and analytical methods used were validated by comparison to external laboratory data (ALS environmental, Waterloo, Canada) (see C.1 for details).

To measure the TPH concentration in the 10-g subsamples excavated from crude oil zones, 15 mL of DCM was added to each sample in a 50 mL glass vial (VWR, Mississauga, Ontario) and shaken for one week. An aliquot of the DCM solution mixture was then analysed by gas chromatography with a flame ionization detector (GC-FID; Agilent GC equipped with an auto-sampler; MDL of 0.48 mg-TPH / kg dry sediment) and then used to determine the concentration of TPH in each sediment sample (g of TPH per kg of dry sediment).

4.2.4 Modelling

4.2.4.1 Description

Linley et al. (2020b, 2021) used a model that solved the single porosity advection dispersion reaction equation (ADRE) combined with a kinetic attachment/detachment relationship to successfully simulate the attachment behaviour of Pluronic-coated NPs in saturated conditions. Jaberi et al. (2021a,b) extended this effort to unsaturated conditions and found that a kinetic attachment/detachment model for both mobile and immobile porosities provided a better representation of the observed NP transport and attachment behaviour. Since HYDRUS 2D (Version 3.02, Šimůnek et al., 1999) does not allow for the simulation of NP reactions in an immobile porosity region, a single porosity system with a kinetic attachment/detachment model was used in this work to simulate NP transport and binding behaviour.

HYDRUS 2D solves the Richards' equation for transient flow, and requires the following set of hydraulic parameters for the van Genuchten-Mualem model: residual water content θ_r (L^3/L^3), total porosity (or saturated water content) ϕ (L^3/L^3), empirical parameters (n (-) and α (1/L)), saturated hydraulic conductivity K_s (L/T), and tortuosity factor l (-). Transport and retention of NPs are simulated using the ADRE combined with a kinetic attachment/detachment model which accounts for nonequilibrium reaction between the aqueous and solid phases (Šimůnek and van Genuchten, 2008). The NP mass balance equations are

$$\frac{\partial(\phi C)}{\partial t}+\frac{\partial(\rho S)}{\partial t}=\frac{\partial}{\partial x_i}\left(\phi D_{ij}\frac{\partial C}{\partial x_j}\right)-q_i\frac{\partial(C)}{\partial x_i} \tag{1a}$$

$$\rho\frac{\partial S}{\partial t}=\phi k_a\psi C-k_\mathrm{d}\rho_b S \tag{1b}$$

with the following Langmuirian-based isotherm coefficient (-) that describes time- and depth- dependent blocking of retention sites

$$\psi=\left(1-\frac{S}{S_{\max}}\right)\left(\frac{d_{50}+z-z_0}{d_{50}}\right)^{-\beta} \tag{2}$$

where C is the aqueous NP/tracer concentration (M/L^3), S is the NP concentration attached to the solid phase (M/M), ρ_b is the bulk density (M/L^3), $D_{ij}=D_T\left|q\right|\delta_{ij}+(D_L-D_T)\frac{q_j q_i}{\left|q\right|}+\theta D_w\tau_w\delta_{ij}$ is the dispersion coefficient tensor (L^2/T), D_T and D_L are the transverse and longitudinal dispersivity, respectively (L), $\left|q\right|$ is the absolute value of the Darcian fluid flux density (L/T), θ is volumetric water content (L^3/L^3), q_i and q_j is the i-th or j-th component of the flux density (L/T), D_w is the aqueous diffusion coefficient (L^2 /T), and τ_w is the tortuosity factor (-), δ_{ij} is the Kronecker delta function ($\delta_{ij}=1$ if i=j, and $\delta_{ij}=0$ if i≠j), k_a and k_d are the attachment and detachment rate coefficients, respectively (1/T), S_{max} is the maximum mass of NPs that can be attached to the solid phase (i.e., sediment or NAPL-impacted sediment) (M/M^-), z_0 is the location coordinate where the straining process starts (i.e, the surface of the porous medium profile), z is distance from the sediment surface, d_{50} is the mean diameter of porous media (L), β is an empirical variable (-). The Langmuir isotherm can describe systems containing an air phase and assumes a surface with homogeneous retention sites, monolayer adsorption, and no interactions between retained particles (Adamczyk et al., 1994; Inyinbor et al., 2016).

4.2.4.2 Parametrization

The 2-D domain (Figure 4-1) was discretized into 12348 nodes and 24469 2D-elements with a base element size of 0.02 m, which was refined to <0.02 m near the the infiltration gallery, outlet, and along the interface of the crude oil zone. This domain was divided into 5 distinct zones as shown in Figure C-5: Zone 1, the infiltration gallery and the two side chambers filled with glass beads; Zone 2, the clean BS in the first 20 cm (wet packed); Zone 3, the clean BS packed in the top 30 cm; Zone 4, the 2% wt crude oil zone; and Zone 5, the 4% wt crude oil zone.

An initial hydrostatic pressure head profile (based on the 0.02 m pressure head at the outlet) was assumed and the initial concentration for both Br^- and CoFe-NPs in the computational domain was assigned zero. A constant flux boundary condition was assigned over the length of the infiltration gallery and a seepage face boundary condition over the remainder of the upper surface. No flow boundary conditions were assigned along the side walls and bottom of the sand tank except for the outlet section where a constant pressure head of 0.02 m was prescribed. Br^- or NPs were introduced into the domain along the infiltration gallery using a specified total mass flux consistent with the concentration and flow rate for the duration of the infiltration pulse. A zero dispersive flux boundary condition was used along the remaining boundaries.

The hydraulic properties including θ_r, n, α, K_s, and l were adopted from Jaberi et al. (2021b) for the clean BS, and for the crude oil zones were determined by trial-and-error calibration using the observed outflow data from both the tracer and NP transport experiments. An estimated porosity (ϕ_T) for each zone (based on the estimated bulk density and particle density of 2.65 g/cm^3) was considered as an initial guess for calibration. The bulk density of each zone was estimated from the known mass of dry sediment used to pack each zone divided by the total volume of the zone. The parameter set which generated the lowest root-mean-square error (RMSE) was considered optimal. In addition, the performance of HYDRUS 2D was evaluated by comparing the observed and simulated effluent data using the coefficient of determination (R^2) as well as the randomness of the residuals (i.e., observed-simulated values) using a normality test (Shapiro and Wilk, 1965).

The Br^- effluent data was used to calibrate the longitudinal dispersivity (α_L) with the transverse dispersivity (α_T) assumed to be 10% of α_L (Domenico and Schwartz, 1990; Šimůnek and van Genuchten, 2006). The attachment/detachment model was not used for the tracer simulation. In addition to using the

Br^- BTC data as the calibration target, the observed Br^- data from the sampling ports were also considered during the calibration process as a confirmatory metric. Thus the longitudinal dispersivity values that produced the lowest RMSE between the simulated and observed effluent Br^- concentrations, and yielded the best visual fit with the observed Br^- data from the sampling ports were deemed optimal. Finally, a visual comparison between the observed dye spatial distribution at selected time points and the simulated tracer distribution was used as a qualitative measure of fit.

Using the calibrated hydraulic and transport parameters, the attachment/detachment parameters (k_a and k_d) in Eq (1b) were determined by trail-and-error calibration using the observed NP effluent BTC data as the calibration target. The observed NP data from sampling ports and a visual comparison between the simulated and observed CoFe-NP retention distribution was used for confirmation. The S_{max} value for each zone was taken from the results of the binding batch tests (Table C-1) except for Zone 1 (glass beads) which was assigned a value of zero. The mean grain diameter (d_{50}) was assigned a value of 0.02 cm, and β was set to 0.432 which is determined by Bradford et al. (2003).

4.3 Results & Discussion

4.3.1 System Hydraulics

For both the tracer and CoFe-NP experiments, flow appeared at the outlet ~75 minutes after the flow to the infiltration galley was initiated, and gradually increased (in ~200 min) to a nearly steady rate of ~35 mL/min. The model was able to capture the flow breakthrough profiles (reflective of the wetting front shape) ($R^2 = 0.95, 0.92$) (Figure 4-3) and the normality of residuals (observed vs simulated data) was confirmed ($p > 0.05$) (see Figure C-6 for residual plots). The calibrated hydraulic parameters for the tracer and CoFe-NP experiments were identical (see Table C-3) flow conditions were the same for both experiments. As expected, the calibrated K_s was lower for zones with crude oil (i.e., 1.7 x10^{-5} m/s for Zone 2 and 1.0 x10^{-5} m/s for Zone 3) compared to the clean BS zones (7.1 x 10^{-5} m/s). The calibrated porosity for the 2% wt. crude oil zone was also lower than the surrounding BS zones (0.28 vs 0.31) due to the presence of oil; however, for the 4% wt. oil zone the porosity (0.33) was higher than both BS and the 2% wt. oil zone likely due to slight variations in packing.

The simulated flow results indicated that the infiltrating solution migrated towards the 2% wt. crude oil zone and passed through the segments with a lower thickness and oil saturation resulting in higher Darcy velocity and preferential pathways (Figure C-7). The simulated Darcy velocity in these segments was larger at earlier times (< 82 min) (0.003 to 0.009 m/min) and then gradually decreased to steady values (0.001 to 0.002 m/min) after ~220 min. The simulated water saturation distribution showed that the water content in the top 30-cm of the sand tank (i.e., crude oil source zone and the non-impacted zone above it) was initially 50-70% and gradually increased to ~90% behind the wetting front (over ~60 minutes), corresponding to a pressure head of -0.03 to -0.001 m. The water saturation in the 4% wt. oil zone was slightly higher compared to the surrounding 2% wt. oil zone at the equilibrium state (initial water content of 71% increased to 95% after 60 min). The water pressure head at the base of the sand tank (except for the outlet section with a prescribed head of 0.02 m) increased from 2 cm to ~13 cm and remained steady after ~200 minutes.

4.3.2 Tracer and NP experiments

4.3.2.1 Observations

The shape of the observed effluent Br^- BTC was asymmetrical with a sharp increase to the peak concentration and a falling limb with a long tail (Figure 4-4) likely a result of the diversity of flow paths (see Figure C-7). The observed effluent CoFe-NP BTC also showed an asymmetrical shape with a significantly lower peak concentration and higher degree of tailing relative to the effluent Br^- BTC (Figure 4-4). The presence of NPs and Br^- in the effluent coincided at ~160 min, and the arrival of the center of mass of the NP BTCs (T_c^{NP}) at the outlet was slightly delayed compared to the center of mass of the Br^- BTC (T_c^{Br}) with a ratio (T_c^{NP}/T_c^{Br}) of 1.1. This delayed arrival of NPs with respect to Br^- indicates that size exclusion (Bradford et al., 2003) did not occur.

The mass recovery of Br^- and NPs was estimated by integrating under the BTC and normalizing by the total infiltrated mass ($M_R = M_{out}/M_{in} \times 100$). The Br^- and NP BTC metrics including M_R, time to the peak concentration (T_{peak}), and T_c^{Br} and T_c^{NP} are presented in Table 1. The recovery of Br^-, a conservative tracer, was 63%, while the NPs experienced more significant retention with only 2% recovery of the total infiltrated mass. The significantly lower peak concentration of the CoFe-NP BTC with respect to Br^- BTC as well as the lower NP M_R indicates significant interaction within the porous medium.

Images of the dye at selected time points during the tracer test are presented in Figure 4-5. The colour red in the photographs was enhanced using a digital image processing software (GIMP 2.10.18) to distinguish the dye from the porous medium, hence, the color intensity does not represent the concentration of the dye. Figure 4-5(a-c) shows that the dye front was uniform above the crude oil zones, and that the presence of the oil generated preferential pathways consistent with simulated flow results. As the dye migrated through the oil zone, it appeared to bypass the segments with increased oil thickness and saturation (i.e., the two lobes) due to reductions in relative permeability (see Figure 4-5(d-g)). The TPH concentration was 5.5 ± 1.3 g/kg in the 2% wt oil zone (equal to 17% crude oil saturation) and approximately two times higher in the 4% wt. oil zone (13.0 ± 3.8 g/kg; equal to 24% crude oil saturation). Changes in the dye distribution after ~300 min were not significant (Figure 4-5(h-j)) which coincides with the falling limb of the Br^- BTC.

The transport of Br^- and CoFe-NPs were also examined using concentration data collected from the sampling ports. Unfortunately, as a result of clogging, samples were only able to be collected from 7 ports (Figure C-9) during the tracer experiment, and from 6 ports during the NP experiment (Figure C-10). This sampling rate was selected (a total of 2% of total pore volume extracted by all samplers at each time point) to have minimal impact on the flow field. Generally, decreased peaks and spreading of the Br^- BTCs was observed from the top to the bottom of the sand tank. The front of the Br^- BTC arrived at sampling port SP-8 (located above the crude oil zone, height of 33 cm) at ~60 minutes after the tracer infiltration started, and arrived at SP-10, SP-12, and SP-15 (height of 25.5 cm) which coincide with the crude oil zone between 80 to 100 mins. Comparing these observations to the dye transport pattern (Figure 4-5), the time of the dye tracer arrival at each sampling port is slightly delayed compared to the Br^- BTC arrival time, indicating that the dye leading front could not be captured by the camera likely due to dilution (or low concentration). Below the crude oil zone, 10 cm above the sand tank base, the Br^- BTC front arrived at SP-22 (approximately below the central lobe of oil zone) at ~120 mins, and at SP-20 and SP-23 (close to the right and left bottom corners of the tank) between 300 and 350 mins, indicating lateral movement of tracer around the crude oil zone, consistent with the dye distribution (Figure 4-5(h-j)). The peak Br^- BTC concentration at SP-20 was significantly lower, and delayed compared to the peak Br^- BTC concentration at SP-23 (SP-20 and SP-30 are located at the same height and close to the right and left bottom corners of the tank, respectively), indicative of the non-uniform transport of the dye tracer below the oil zone.

The CoFe-NP BTC at SP-2 (Figure C-10), which is located below the infiltration gallery (at 40 cm from the sand tank base) shows a significantly higher peak concentration compared to SP-8, located just above the crude oil zone (at 33 cm from the sand tank base). This observation implies that the NPs experienced substantial retention within the clean zone as they moved down towards the oil zone (i.e., between the infiltration gallery and the top of the oil zone). The CoFe-NP BTCs for ports located within and below the crude oil zone showed significantly lower peak concentrations and longer tails that indicated that high retention occurred within the crude oil zones. The NP BTC at SP-8 coincided with the Br^- BTC, while at other ports the CoFe-NP BTCs were delayed compared to their respective Br^- BTC, except at SP-20 located close to the lower right-hand side of the tank (at 10 cm from the base). In addition, the CoFe-NP BTC at SP-20 showed a higher peak concentration compared to the BTC at SP-18 (located above SP-20 at 13.5 cm from the sand tank base), likely due to the non-uniform transport of CoFe-NPs below the oil zone (Figure 4-5, T = 172 min). The higher peak concentration of CoFe-NP BTC at SP-15 compared to that at SP-10 (located at the same height of 25.5 cm; SP-10 in the oil zone and SP-15 in the clean zone) indicates that the CoFe-NPs preferentially moved towards the surrounding clean BS and bypassed the two lobes in the oil zone. This preferential transport of NP is also consistent with the observed dye tracer transport pattern (Figure 4-5(c-e)).

The distribution of the retained CoFe-NPs ($M_{retained}$) across the width of the sand tank in each 1- or 2-cm thick layer across the non-impacted and crude oil zones was investigated. Results showed that there were no statistically significant differences ($p > 0.05$) indicating that the CoFe-NPs were evenly distributed across the width of the tank (Figure C-11). Hence, the CoFe-NP retained concentrations were averaged across the tank width at each sampling location and used to create a CoFe-NP retention spatial distribution. Figure 4-7(a) shows that the majority of CoFe-NPs (between 80 and 90% based on the retention data) were retained above and within the crude oil zone. The concentration of the retained CoFe-NPs in the BS non-impacted zone across the upper 30-cm of the sand tank (i.e., Zone 3 in Figure C-5) ranged from 5 to 29 mg/kg with the higher end of this range reflecting possible straining of CoFe-NPs. Jaberi et al. (2020a,b) and Linley et al. (2021) reported that a higher retention of CoFe-NPs was observed near the injection point in column systems and attributed this to irreversible attachment (capillary and/or hydrophobic forces) at the AWIs and possible aggregation. Despite the small size range of the CoFe-NPs (below the straining threshold), destabilization and aggregation of these NPs is possible in natural porous media during their transport due to Pluronic adsorption to mineral material present in BS which leaves the hydrophobic oleic acid inner coating more exposed (Linley et al., 2021; Jaberi et al., 2021a,b). In addition to aggregation, the presence of air phase would likely result in increased CoFe-NPs retention, specifically in the first ~50 min of infiltration (i.e., straining and/or attachment to AWIs) (Chen et al., 2008; Hoggan et al., 2016; Jaberi et al., 2021b), as based on the simulated water content, approximately the upper 30-cm of the tank including the top BS zone (Zone 3 in Figure C-5) and the oil zone were unsaturated.

In addition to the higher retention in the upper portion of the sand tank, a few retention hotspots were present just above the crude oil zone (red spots in Figure 4-7(a)). These locations coincide with the preferential flow paths discussed above (Figure C-7) where the increased transport of CoFe-NPs along these paths, especially during the first 80 minutes of infiltration, may have increased interaction between NPs leading to aggregation and consequent pore straining or trapping. The CoFe-NP $M_{retained}$ in the 2% wt. crude oil zone is within the same range as the upper 30 cm of the sand tank (5 to 28 mg/kg) and decreased to 3 to 11 mg/kg within the 4% wt. crude oil zone and the lower 20-cm of the sand tank (i.e., Zone 2 in Figure C-5) (Table 1). Comparing these values to the CoFe-NP attachment capacity from the batch binding tests (S_{max}) (Table C-1) indicates that in some locations within the upper 30 cm zone, the CoFe-NP retained concentration was almost 2 to 4 times higher than the estimated value from the batch tests. In contrast, the NP retained concentration was 3 times lower than the S_{max} value from the batch tests for the lower 20 cm of the sand tank due to restricted migration of CoFe-NPs below the crude oil zone. The substantially decreased CoFe-NP mass retained in the 4% wt. crude oil zone and the lower parts of the two lobes in the 2% wt. crude oil zone compared to the remained of the crude oil zone is reflective of the relatively decreased accessibility of these segments to CoFe-NPs as a result of the preferential flow paths. In contrast, our previous targeted binding investigations in saturated and unsaturated columns demonstrated higher accumulation of CoFe-NPs in crude oil-impacted sediments with $M_{retained}$ at least 2 times higher than that in the non-impacted sediments (Jaberi et al., 2021a,b; Linley et al., 2020a). Consistent with our observations, Phenrat et al. (2011) reported that the targeting of a NAPL by polymer-modified nZVI was primarily controlled by the available NAPL/water interface which is also a function of NAPL saturation. The results from this study, demonstrate that preferential flow paths, primarily caused by the relatively lower permeability of the crude oil zone, limit the degree of preferential binding that can occur throughout a crude oil zone.

4.3.2.2 Model simulations

Simulations using HYDRUS 2D provided a reasonable fit with the observed effluent Br^- and CoFe-NP BTCs (R^2 = 0.79 and 0.70, respectively, with residuals normally distributed ($p > 0.05$) (see Figure C-6); however, both the effluent Br^- and CoFe-NP BTC tails were not captured (Figure 4-4). It should be noted that for the probability plot of the residuals of tracer, the tail data points were ignored. The inability to re-create these BTC tails, specifically for the Br^-, is believed to be a result of ignoring the mass transfer between the immobile and mobile regions of flow in unsaturated porous medium and the associated reactions. The calibrated model parameters are presented in Table 2.

The model simulation using the calibrated transport parameters provided a reasonable fit to the observed Br^- BTCs at the sampling ports (R^2 =0.73 - 0.92) (Figures C-9(a)). During the calibration process it was found that a higher dispersivity for the 20-cm bottom BS zone (i.e., Zone 2, Figure C-5) was required to generate a better fit to the observed effluent BTC and capture the rising limb of the Br^- BTCs at SP-20 and SP-23. A visual comparison (qualitative assessment) between the observed and simulated dye distribution at selected time points was also in good agreement using the calibrated hydraulic and transport parameters from the flow and tracer observed data (Figure 4-6). The simulated dye distribution shows that the simulated front is slightly ahead of the observed front while consistent with the arrival time of the observed Br^- BTCs, due to the lower concentrations of the dye front that could not be captured by the camera. The simulated tracer distribution at 650 min shows that tracer presence in the side chambers and along the top portions of the sand tank (not present in the dye images due to low concentrations) may be partially responsible for the long tail in the Br^- BTC and incomplete tracer recovery (M_R = 63%).

The calibrated model parameters using the effluent CoFe-NP BTC provided an overall good agreement with the spatial distribution of the retained CoFe-NP concentration (Figure 4-7) and the sampling ports' data (R^2 =0.67 - 0.89). The observed retention of NPs in the upper 30-cm of the sand tank, as shown in Figure 4-7, was attributed to a combination of irreversible attachment at the AWIs and possible aggregation. Both of these retention mechanisms are manifested as NP mass removal from the aqueous phase and covered by the depth-dependant straining and is consistent with our previous findings in column studies (Jaberi et al., a,b). A mechanistic investigation into this retention behavior (i.e., straining) was not a focus of this research. The simulated CoFe-NP BTC at the presented 6 sampling ports were in good agreement with the observed data (Figure C-10), except at SP-10 and SP-20 for which the simulated BTC appeared earlier (at 90 vs 120 min and 170 vs 210 min, respectively) likely due to some sampling variations.

The calibrated attachment rate coefficient, k_a, for the 2% and 4% wt. crude oil zones were similar (2.7×10^{-3} and 2.3×10^{-3} /s) and an order of magnitude greater than the k_a for the upper and bottom BS zones (3.3×10^{-4} and 2.8×10^{-4} /s) indicating preferential CoFe-NP attachment to the crude oil. Previous investigations using batch binding tests (Linley et., 2020a) indicated that NP attachment to the crude oil- impacted sand increased with increasing oil concentration up to ~2% wt. which was suggested as the NP binding threshold since the addition of more oil would only contribute to thicker oil layer covering the sand grains without increasing the surface area. This finding is consistent with the nearly equal estimated k_a for the 2% and 4% oil zones here. The estimated k_d was 8.3×10^{-6} /s for the BS zones and approximately one order of magnitude lower in the oil zones (4.8×10^{-7} /s for 4% wt. oil zone and 6.4×10^{-7} /s for 2% wt. oil zone). The significantly higher ratio of k_a to k_d in the 2% and 4% wt. oil zones (by 4 orders of magnitude) compared to that in BS zones (by 2 orders of magnitude) is indicative of more irreversible or stronger attachment of CoFe-NPs to the oil-impacted sand, which is consistent with our previous studies in unsaturated columns and lysimeter. The significantly higher k_a in the oil zone compared to the clean zone is also consistent with our previous findings in the column studies (Jaberi et al., a,b).

4.4 Conclusions

This study presents the transport and targeted binding of Pluronic-coated NPs to a heterogeneous crude oil source zone in an unsaturated 2-D physical model equipped with an infiltration gallery for delivering NPs, representative of a potential field delivery application. NPs with a low concentration of the Pluronic co-polymer coating which, based on previous studies, promotes binding to an oil phase were employed in the 2-D physical model experiment. The NP BTCs exhibited significantly lower peak concentrations and higher degree of tailing relative to the tracer BTC and the recovered mass was only 2% of the total infiltrated mass compared to 63% for the tracer. Visual observations from a dye tracer experiment demonstrated preferential flow paths that bypassed thicker segments of the source zone with higher oil saturation, due to relative permeability decrease.

The spatial distribution of retained CoFe-NP indicated substantial retention of NPs in the crude oil zone and the overlaying non-impacted zone. The considerable retention of NPs in the non-impacted zone was attributed to straining favored by low water saturation and possible NP aggregation. Results also showed that NPs had less accessibility to the segments of the crude oil source zone with more thickness and higher oil saturation, as NPs followed the preferential flow paths. Hence, significantly lower NP retained mass was observed in these segments compared to the other portions of the oil zone.

The single porosity transport model with depth-dependent straining and kinetic attachment/detachment reactions provided an acceptable description of the observed NP retention behaviour. Despite approximately equal NP retained mass in the crude oil zone and the non-impacted zone above the oil zone, the estimated attachment rate coefficient, k_a, was about an order of magnitude greater for the oil zone than the k_a for the non-impacted zone, which demonstrates NP targeted binding towards crude oil. However, the substantial retention of the NPs in the non-impacted zone above the oil zone, as well as the preferential flow paths which directed NP away from the thicker and higher oil-content regions of the oil zone, reduced the degree of NP preferential binding that could occur throughout the crude oil zone.

Results of this study extend our knowledge of the transport and targeted binding of amphiphilic co-polymer coated NPs in a more realistic condition. Generally, the results demonstrated that in addition to NP characteristics (size, stability, dosage), NP transport is significantly influenced by physical factors (heterogeneity, water content) which should be considered during the design of NP delivery systems to a NAPL source in the unsaturated zone. Results have important implications for modeling the fate and transport of NPs at NAPL contaminated sites. However, more suitable models capable of handling NP aggregation and the non-equlilibrium physical and chemical transport should be used for a better description of NPs behaviour in unsaturated multidimensional systems.

4.5 Acknowledgements

This research was funded by Chevron Energy Technology Company. The assembly and construction of experimental apparatus by Terry Ridgway is highly appreciated. We thank Mark Merlau and Shirley Shatton for their technical assistance, and acknowledge the Canadian Centre for Electron Microscopy (CCEM) for providing the TEM images of CoFe-NPs.

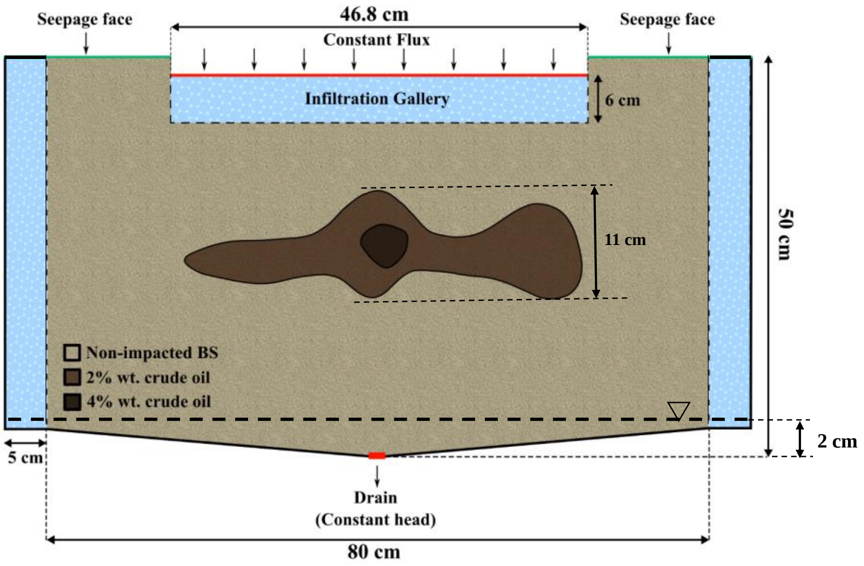

Figure 4-1. Schematic of the simulated domain (90 cm long x 50 cm high x 10 cm wide) including non-impacted and crude oil impacted sediments (2% wt. and 4% wt. crude oil). 5-cm wide chambers at each end of the sand tank were filled with glass beads and separated from the packed medium by a perforated plate wrapped with a nylon filter cloth. Tracer and CoFe-NPs were allowed to propagate through the domain, introduced at the infiltration gallery, while a 2 cm pressure head was maintained at the base.

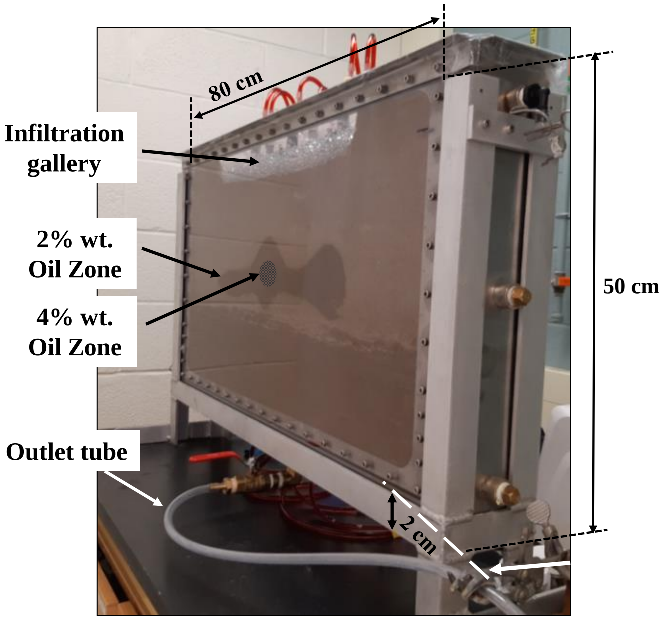

Figure 4-2. Configuration of the packed sand tank with non-impacted sand and crude oil-impacted sand. For details on the infiltration gallery see Figure C-3 (in Appendix C).

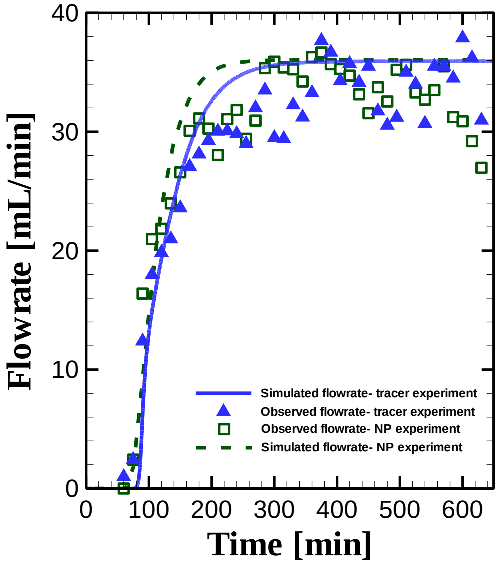

Figure 4-3. Simulated (solid line) and observed (symbols) effluent flow breakthrough profile at the outlet for tracer and CoFe-NP transport experiments.

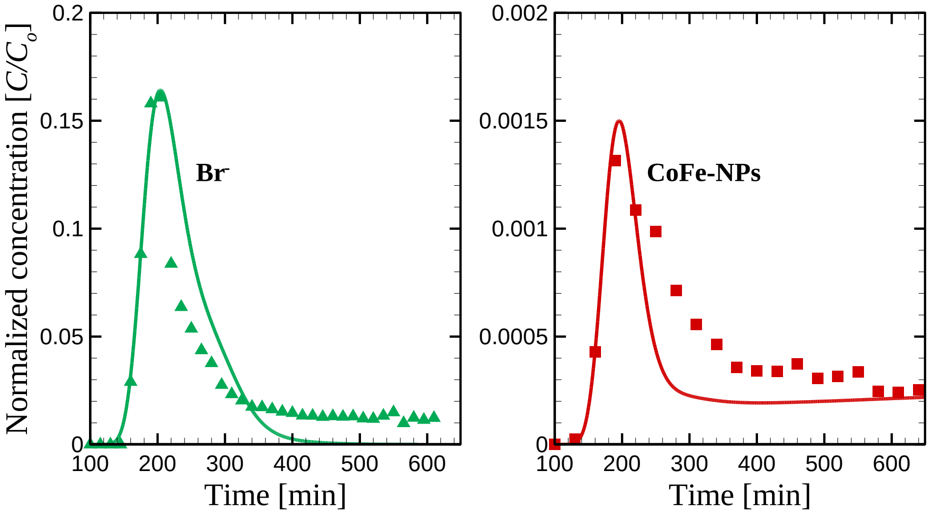

Figure 4-4. Observed (symbols) and simulated (solid line) normalized BTCs of Br^- and CoFe-NP for the tracer and CoFe-NP experiments with an injection CoFe-NP target concentration of 400 mg/L and dosage of 230 mg. The flow rate was constant at ~35 mL/min.

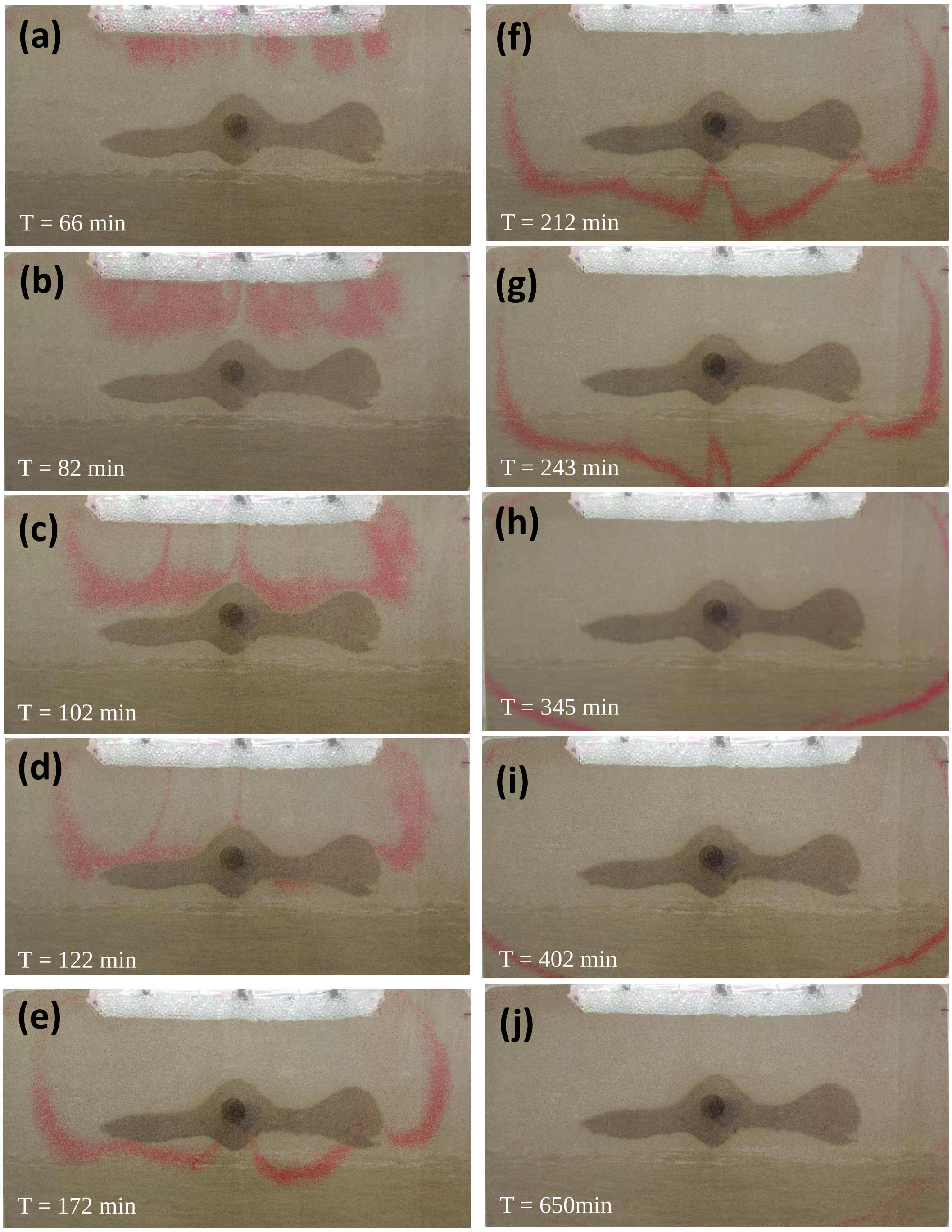

Figure 4-5. Dye distribution captured during the tracer experiment. The injection tracer solution contained (~ 200 mg/L Br^- in a diluted water-soluble food dye (red No. 40) (~750 mL)). The pulse injection of tracer solution was ~12 minutes at a constant rate of ~35 mL/min followed by Millipore water at the same flowrate until red dye was no longer visible through the front Plexiglas wall (650 min).

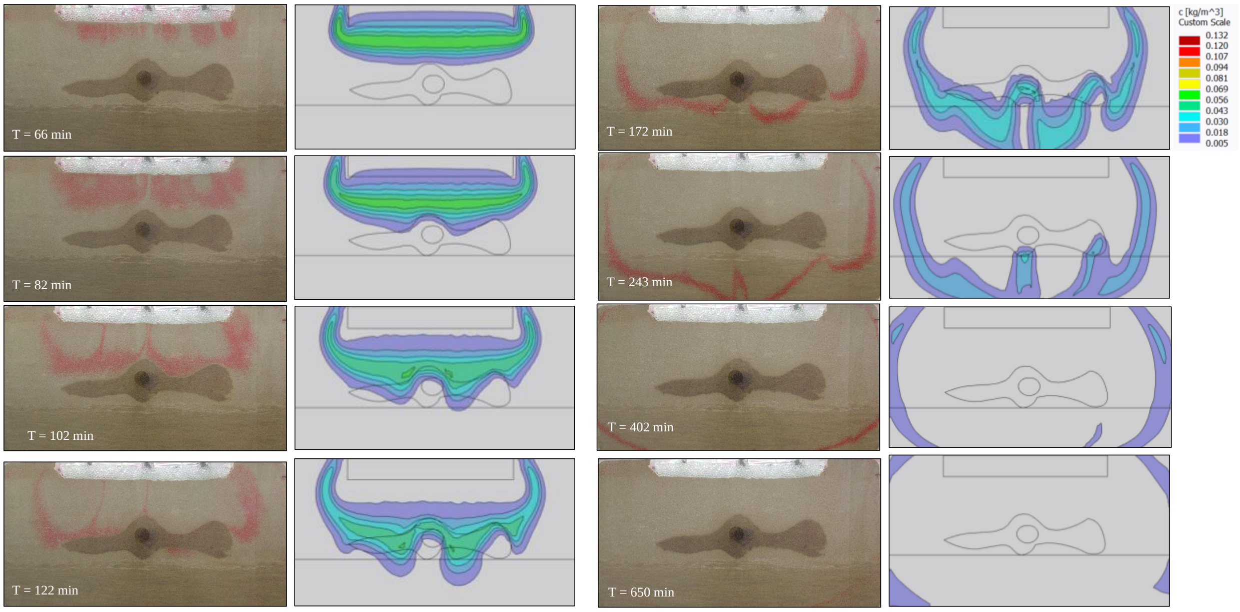

Figure 4-6. Observed and simulated tracer distribution at selected time points.

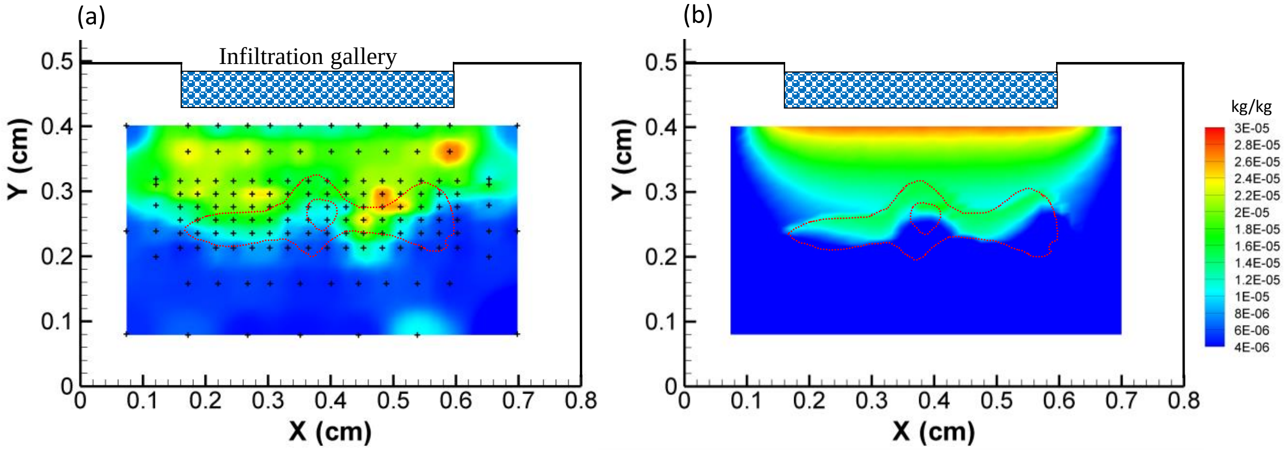

Figure 4-7. Observed (a) and simulated (b) retained concentration distribution of CoFe-NPs (kg Co_T/kg sediment) at the conclusion of the CoFe-NP experiment. Data was obtained from direct measurement of the cobalt in subsamples collected at the locations indicated (+). The average NP concentration from two or three subsamples collected across the width of the tank are presented at each location.

Table 4-1 BTC metrics for Br^- and NPs.

Exp. ID	Material	M_R	T_{peak}	T_c	Dose	$M_{retained}$	
						Min	Max
		[%]	[min]	[min]	[mg]	[mg/kg]	
Tracer	---	63%	210	290	102	---	---
CoFe-NP	Moist BS	2%	240	368	232	5	29
	2% wt. oil-impacted BS					5	28
	4% wt. oi-impacted BS					3	11
	Wet packed BS					4	11

Table 4-2 Calibrated model parameters.

Zone ID	Material	α_L	α_T	ϕ_T	K_s	S_{max}	k_a	k_d
		$[m]\times10^{-4}$	$[m]\times10^{-4}$	[-]	$[m/s]\times10^{-5}$	[mg/kg]	$[1/s]\times10^{-3}$	$[1/s]\times10^{-6}$
2	Wet packed BS	80	8	0.30	7.2	7.7	0.3	8.3
3	Moist BS	24	2.4	0.32	7.2	7.7	0.3	8.3
4	2% wt. oil-impacted BS	8	0.8	0.28	1.7	24.0	2.7	0.6
5	4% wt. oi-impacted BS	5	0.5	0.34	1.0	30.0	2.3	0.5

Chapter 5

Conclusions and Recommendations

5.1 Conclusions

The overarching objective of this research was to investigate the capability of amphiphilic co-polymer coated NPs to transport and bind to a target NAPL in unsaturated porous media. The role of some controlling factors (initial water saturation, porous medium texture, input dosage, and flowrate) on NP transport behavior and the targeted NP binding to a crude oil zone were investigated using series of short column experiments (Chapter 2) to address Research Question 1. The transport and binding ability of these NPs were later examined at a spatial scale representative of the unsaturated zone above a shallow aquifer system using a 1.4-m long column (Chapter 3) which addressed Research Question 2. Finally, a two-dimensional physical model experiment was carried out to assess the capability of the NPs to target a heterogeneous crude oil zone in a less constrained unsaturated system (Chapter 4) to address Research Question 3. In the course of these investigations, reactive transport models were used to corroborate experimental findings and describe NP transport and binding behavior (Research Question 4).

The following conclusions emerged from this research effort:

1. Multiple lines of evidence demonstrated preferential binding of Pluronic-coated NPs to a target crude oil zone in unsaturated porous media. Experimental data were used to estimate the NP attachment/detachment parameters and the results showed that typically for NPs in the crude oil zone the attachment rate coefficient, k_a, exceeds the k_a for NPs in the non-impacted zones by ~one to two order(s) of magnitude. The k_a varied on the order of 10^{-3} -10^{-2} /s for the crude oil zone, while it was on the order of 10^{-4} for the non-impacted zones. The detachment rate coefficient, k_d, was nearly identical for NPs in both the non-impacted and crude oil zones, and varied between 10^{-7} to 10^{-6} /s. The considerably higher ratio of k_a to k_d suggests stronger attachment of NPs in the crude oil zone compared to the non-impacted zones.
2. Despite the demonstrated NP targeted binding to the crude oil zone, results from the 2-D physical model experiment revealed considerable impact of the physical heterogeneities, caused by the presence of crude oil in the system, on NP transport and targeted binding. The presence of preferential flow paths as a result of the physical heterogeneity reduced the delivery efficiency of NPs to portions of the crude oil zone. Results from the column experiments showed that the retained mass of NPs was twice or three times higher in the crude oil zone than the surrounding non-impacted zones, whereas in the 2-D physical model the retained mass of NPs in the 2% wt crude oil zone and the non-impacted zone above

the crude oil zone were similar. The retained NP mass in the crude oil zone was in the range 5-28 mg/kg in the 2% wt oil zone while it was in the range of 3-11 mg/kg in the 4% wt crude oil zone due to lower permeability and hence limited accessibility of NPs to the crude oil in this zone. The considerable decrease in the NP mass retained in the 4% wt crude oil zone and the lower portions of the 2% wt crude oil zone compared to the other portions of the crude oil zone is reflective of the relatively decreased accessibility of these zones to NPs due to the preferential flow paths that were developed in this system.

3. In addition to simulated reversible attachment processes, a depth-dependent straining term was required to reproduce the observed NP retention near the top of the columns and in the non-impacted zone above the crude oil zone in the 2-D physical model. This retention behavior likely occurred as a result of aggregation (specifically for the CoFe-NPs with the lower polymer coating concentration used) and/or irreversible attachment at the air-water interfaces due to the comparatively lower initial water content.
4. Observations from large column experiment indicated that the NPs experienced consistent retention as the solution migrated further down the column possibly due to increased contact with sediments and subsequent aggregation and trapping. As a result, the simulation model that including attachment/detachment with nonlinear Langmuirian blocking and depth-dependent straining used for the short column experiments required an additional mass loss term to represent the observed NP retention behavior in the large column system. This mass loss term used is consistent with the collector efficiency rate in colloid filtration theory where removal of NPs from the aqueous phase is a first-order kinetic process.
5. Results from short column experiments established the significant role of initial water content, injection flow rate and concentration, and porous medium texture on the transport and retention behavior of the Pluronic-coated NPs in unsaturated conditions. Increased NP retention was found to directly correlate with a lower initial water content and associated higher air saturation. Similarly, at a lower injection flow rate NP retention increased due to higher air saturation and longer residence time. The initial water saturation and flow rate did not have a considerable impact on the NP attachment rate coefficient, while the detachment rate coefficient decreased with lower initial water saturation and flow rate. Substantial retention of NPs occurred in columns packed with higher clay and silt content sediment as a result of the larger surface area. The attachment rate coefficient increased by an order of magnitude in the columns with higher clay and silt content sediment and the detachment rate coefficient decreased (~8 times), suggesting a significant increase in attachment to, and decrease in detachment from, the higher clay and silt content sediment.
6. The observed asymmetrical NP breakthrough data from the unsaturated column experiments was reproduced using a model considering both mobile and immobile porosity regions, and a kinetic attachment/detachment reaction with nonlinear Langmuirian blocking for NP retention and release. An

acceptable description of NP retention behavior was obtained using a similar modelling approach for the 2-D physical model except that the model used represented the porous medium as single porosity system. These simulation efforts illustrated that models which can represent NP aggregation in addition to both physical and chemical nonequilibrium transport processes are required to better reflect the observed NP transport and binding behavior in the unsaturated experimental systems investigated.

Findings from this research contribute to our knowledge of the transport and binding behavior of Pluronic-coated NPs in unsaturated porous media. The confirmed targeted binding of these NPs to a crude oil zone present in unsaturated porous media, in addition to the previous demonstration in saturated conditions, provides the foundation to advance the use of these NPs as a treatment agent or a delivery vehicle for treatment reagents. The targeting capability of these NPs will increase treatment efficiency, specifically in cases where a large loading of a reagent is required for treatment. NP targeted binding capability is influenced by physical heterogeneity and NP depth-dependent straining which may reduce the degree of NP preferential binding that could occur throughout a crude oil zone. NP straining is inevitable, specifically in unsaturated systems, however, the role of heterogeneity should be considered in the design of potential NP delivery strategies for targeting source zones in similar systems. In addition, the significant role of initial water content, flow rate, and porous medium texture suggests that these controlling factors should be considered during the design of potential NP delivery strategies to enhance NP transport in unsaturated porous media. The noted increase in NP retention over longer travel distances due to suspected aggregation and trapping is suggestive of stability issues of these NPs in unsaturated porous media which may pose a limitation for the delivery of these NPs to a target zone distal from the injection location.

5.2 Recommendations for Future Work

Although significant contributions were obtained in this research, limitations regarding the use of NPs for field applications was identified. NPs are typically required to travel a long distance (> 1 meter) from the injection location to reach a target treatment zone, while substantial retention of the Pluronic-coated NPs, suspected as aggregation, occurred at long travel distances. Investigation is required on the stability of these NPs in relation to aggregation and impacts on NP transport in longer experimental systems. Physicochemical characterization of the NPs including morphology, concentration and size (individual or aggregate clusters) should be explored. The effect of porous media mineralogy, and groundwater geochemistry should also be considered. These factors may influence NP stability and binding behavior affecting the Pluronic coating material.

Based on the other conclusions of this research, tasks are proposed herein to further advance this work:

Investigate the impact of medium heterogeneity on NP transport and retention in representative multidimensional systems. Results from chapter 2 demonstrated the role of the porous medium grain size on NP retention as significantly higher retention was observed in columns with 20% more silty sand material (SSS) than the sandy material (BS). However, NP transport and binding behavior in heterogeneous packed systems resembling field conditions (e.g., stratified geological media) remain unknown. This study is essential for the better understanding of NPs transport behavior in field conditions to support the design of pilot-scale investigations. To collect this data, NP transport experiments should be performed in a 2-D or 3-D system packed with different well-characterized sediment types. The sediment materials should be selected in a way to represent different factors such as natural organic matter (NOM), mineral elements, grain size distribution, and permeability.

The transport and targeted binding ability of the Pluronic-coated NPs has been investigated at the laboratory- scale, however, NP transport and binding ability need to be verified using *in situ* pilot-scale investigations to access NP targeted binding feasibility. Similar NP transport experiments used in this study can be performed at the pilot-scale for example in an outdoor lysimeter (or excavated pits in large dimensions, e.g., 6 x 4 x 5 m) and similar infiltration system proposed here (Chapter 4) can be used for the introduction of tracer and NP solution into the unsaturated zone. *In situ* undisturbed lysimeters (e.g., monolith lysimeters) are often used for environmental research in vadose zone (unsaturated zone). Compared to laboratory studies, these lysimeters can take into account more physical factors along with their complex interactions which may also occur at a field site and impact NP transport and binding. Appropriate transport models for unsaturated conditions (considering both physical and chemical nonequilibrium transport and aggregation) can be calibrated using the pilot-scale experimental data to enable reliable prediction of NP transport and binding under different real-field condition scenarios (e.g., considering precipitation, evaporation, etc) and help practitioners with the efficient NP delivery systems design.

Various numerical models have been successfully applied to describe several NP transport and retention mechanisms, such as reversible attachment/detachment, irreversible attachment to AWIs, depth-dependent straining, aggregation. However, the concurrent presence of multiple mechanisms in real-field conditions has not been developed yet. For example, result from Chapter 3 and 4 indicated occurrence of aggregation and straining in addition to reversible and irreversible attachments. Hence, more robust multidimensional models with multiple transport and retention phenomena are required for the simulation of NP transport and binding real field application for the better design of remediation strategies.

NP delivery into a target treatment zone should be further optimized to help with successful *in situ* remediation. An optimization study should be performed using many lab-scale transport and binding tests combined with existing numerical model to find the optimum range of controlling factors (e.g., flow rate, NP coating concentration, and solution chemistry such as pH, and ionic strength (IS)) that maximize NP accumulation within an impacted zone. This study would help with a more systematic design for the enhanced delivery of these NPs into complex systems.

Chapter 6

References

Adamczyk, Z., Siwek, B., Zembala, M., & Belouschek, P. (1994). Kinetics of localized adsorption of colloid particles. *Advances in Colloid and Interface Science*, *48*(C), 151–280. https://doi.org/10.1016/0001-8686(94)80008-1

Addai-Mensah, J. (2007). Enhanced flocculation and dewatering of clay mineral dispersions. *Powder Technology*, *179*(1–2), 73–78. https://doi.org/10.1016/j.powtec.2006.11.008

Akhtar, M. S., Stüben, D., Norra, S., & Memon, M. (2011). Soil structure and flow rate-controlled molybdate, arsenate and chromium(III) transport through field columns. *Geoderma*, *161*(3–4), 126–137. https://doi.org/10.1016/j.geoderma.2010.12.005

Ball, W. P., Buehler, C., Harmon, T. C., Mackay, D. M., & Roberts, P. V. (1990). Characterization of a sandy aquifer material at the grain scale. *Journal of Contaminant Hydrology*, *5*(3), 253–295. https://doi.org/10.1016/0169-7722(90)90040-N

Bishop, E. J., Fowler, D. E., Skluzacek, J. M., Seibel, E., & Mallouk, T. E. (2010). Anionic homopolymers efficiently target zerovalent iron particles to hydrophobic contaminants in sand columns. *Environmental Science and Technology*, *44*(23), 9069–9074. https://doi.org/10.1021/es1017398

Bradford, S. A., Simunek, J., Bettahar, M., Van Genuchten, M. T., & Yates, S. R. (2003). Modeling colloid attachment, straining, and exclusion in saturated porous media. *Environmental Science and Technology*, *37*(10), 2242–2250. https://doi.org/10.1021/es025899u

Bradford, S. A., Torkzaban, S., & Simunek, J. (2011). Modeling colloid transport and retention in saturated porous media under unfavorable attachment conditions. *Water Resources Research*, *47*(10), 1–12. https://doi.org/10.1029/2011WR010812

Bradford, S. A., Yates, S. R., Bettahar, M., & Simunek, J. (2002). Physical factors affecting the transport and fate of colloids in saturated porous media. *Water Resources Research*, *38*(12), 63-1-63–12. https://doi.org/10.1029/2002wr001340

Brown, D. M., Bonte, M., Gill, R., Dawick, J., & Boogaard, P. J. (2017). Heavy hydrocarbon fate and transport in the environment. *Quarterly Journal of Engineering Geology and Hydrogeology*, *50*(3), 333–346. https://doi.org/10.1144/qjegh2016-142

Busch, J., Meißner, T., Potthoff, A., & Oswald, S. E. (2014). Investigations on mobility of carbon colloid supported nanoscale zero-valent iron (nZVI) in a column experiment and a laboratory 2D-aquifer test system. *Environmental Science and Pollution Research*, *21*(18), 10908–10916. https://doi.org/10.1007/s11356-014-3049-7

Celia, M. A., Bouloutas, E. T., & Zarba, R. L. (1990). A general mass-conservative numerical solution for the unsaturated flow equation. *Water Resources Research*, *26*(7), 1483–1496. https://doi.org/10.1029/WR026i007p01483

Chen, L., Sabatini, D. A., & Kibbey, T. C. G. (2008). Role of the air-water interface in the retention of TiO2 nanoparticles in porous media during primary drainage. *Environmental Science and Technology*, *42*(6), 1916–1921. https://doi.org/10.1021/es071410r

Cherrey, K. D., Flury, M., & Harsh, J. B. (2003). Nitrate and colloid transport through coarse Hanford sediments under steady state, variably saturated flow. *Water Resources Research*, *39*(6), 1–10. https://doi.org/10.1029/2002WR001944

Chowdhury, I., Hong, Y., Honda, R. J., & Walker, S. L. (2011). Mechanisms of TiO2 nanoparticle transport in porous media: Role of solution chemistry, nanoparticle concentration, and flowrate. *Journal of Colloid and Interface Science*, *360*(2), 548–555. https://doi.org/10.1016/j.jcis.2011.04.111

Darko-Kagya, K., & Reddy, K. R. (2011). Two-dimensional transport of lactate-modified nanoscale iron particles in porous media. *Remediation*, *21*(4), 45–72. https://doi.org/10.1002/rem.20299

Davis, M. E., Chen, Z., & Shin, D. M. (2008). Nanoparticle therapeutics: An emerging treatment modality for cancer. *Nature Reviews Drug Discovery*, *7*(9), 771–782. https://doi.org/10.1038/nrd2614

Degenkolb, L., Dippon, U., Pabst, S., & Klitzke, S. (2019). Transport and retention of differently coated CeO2 nanoparticles in saturated sediment columns under laboratory and near-natural conditions. *Environmental Science and Pollution Research*, *26*(16), 15905–15919. https://doi.org/10.1007/s11356-019-04965-x

Domenico, P. A., and F. W. Schwartz (1990), Physical and Chemical Hydrogeology, *John Wiley, N. Y*

Elliott, D. W., & Zhang, W. X. (2001). Field assessment of nanoscale bimetallic particles for groundwater treatment. *Environmental Science and Technology, 35*(24), 4922–4926. https://doi.org/10.1021/es0108584

Fang, J., Shan, X. quan, Wen, B., & Huang, R. xiang. (2013). Mobility of TX100 suspended multiwalled carbon nanotubes (MWCNTs) and the facilitated transport of phenanthrene in real soil columns. *Geoderma*, *207–208*(1), 1–7. https://doi.org/10.1016/j.geoderma.2013.04.035

Fang, J., Shan, X. quan, Wen, B., Lin, J. ming, & Owens, G. (2009). Stability of titania nanoparticles in soil suspensions and transport in saturated homogeneous soil columns. *Environmental Pollution*, *157*(4), 1101–1109. https://doi.org/10.1016/j.envpol.2008.11.006

Fang, J., Xu, M. jia, Wang, D. jun, Wen, B., & Han, J. yi. (2013). Modeling the transport of TiO2 nanoparticle aggregates in saturated and unsaturated granular media: Effects of ionic strength and pH. *Water Research*, *47*(3), 1399–1408. https://doi.org/10.1016/j.watres.2012.12.005

Flury, M., & Aramrak, S. (2017). Role of air-water interfaces in colloid transport in porous media: A review. *Journal of the Water Resources*, *53*, 5247–5275. https://doi.org/10.1002/2017WR020597

Gao, B., Saiers, J. E., & Ryan, J. (2006). Pore-scale mechanisms of colloid deposition and mobilization during steady and transient flow through unsaturated granular media. *Water Resources Research*, *42*(1), 1–9. https://doi.org/10.1029/2005WR004233

Herzig, J. P., Leclerc, D. M., & Le Goff, P. L. (1970). Flow of Suspensions through Porous Media— Application to Deep Filtratio. *Industrial and Engineering Chemistry*, *62*(5), 8–35. https://doi.org/10.1021/ie50725a003

Hoggan, J. L., Sabatini, D. A., & Kibbey, T. C. G. (2016). Transport and retention of TiO2 and polystyrene nanoparticles during drainage from tall heterogeneous layered columns. *Journal of Contaminant Hydrology*, *194*, 30–35. https://doi.org/10.1016/j.jconhyd.2016.10.003

Inyinbor, A. A., Adekola, F. A., & Olatunji, G. A. (2016). Kinetics, isotherms and thermodynamic modeling of liquid phase adsorption of Rhodamine B dye onto Raphia hookerie fruit epicarp. *Water Resources and Industry*, *15*, 14–27. https://doi.org/10.1016/j.wri.2016.06.001

Jaberi, N., Linley, S., Thomson, N. R., McVey, K., Sra, K., & Gu, F. X. (2021a). Nanoparticle Transport and Targeted Binding in Unsaturated Porous Media. Manuscript prepared with the intent for publication. *J. Contam. Hydrol.*

Jaberi, N., Linley, S., Thomson, N. R., McVey, K., Sra, K., & Gu, F. X. (2021b). Unsaturated Transport and Targeted Binding of Nanoparticles: Large Column Experiments. Manuscript prepared with the intent for publication. *J. Contam. Hydrol.*

Jin, C., Glawdel, T., Ren, C. L., & Emelko, M. B. (2015). Non-linear, non-monotonic effect of nano-scale roughness on particle deposition in absence of an energy barrier: Experiments and modeling. *Scientific Reports*, *5*(December), 1–14. https://doi.org/10.1038/srep17747

Jin, C., Zhao, W., Normani, S. D., Zhao, P., & Emelko, M. B. (2017). Synergies of media surface roughness and ionic strength on particle deposition during filtration. *Water Research*, *114*, 286–295. https://doi.org/10.1016/j.watres.2017.02.010

Jung, B., O'Carroll, D., & Sleep, B. (2014). The influence of humic acid and clay content on the transport of polymer-coated iron nanoparticles through sand. *Science of the Total Environment*, *496*, 155–164. https://doi.org/10.1016/j.scitotenv.2014.06.075

Kambhu, A., Li, Y., Gilmore, T., & Comfort, S. (2021). Modeling the release and spreading of permanganate from aerated slow-release oxidants in a laboratory flow tank. *Journal of Hazardous Materials*, *403*(April 2020), 123719. https://doi.org/10.1016/j.jhazmat.2020.123719

Kamrani, S., Rezaei, M., Kord, M., & Baalousha, M. (2018). Transport and retention of carbon dots (CDs) in saturated and unsaturated porous media: Role of ionic strength, pH, and collector grain size. *Water Research*, *133*, 338–347. https://doi.org/10.1016/j.watres.2017.08.045

Kanel, S. R., Goswami, R. R., Clement, T. P., Barnett, M. O., & Zhao, D. (2008). Two dimensional transport characteristics of surface stabilized zero-valent iron nanoparticles in porous media. *Environmental Science and Technology*, *42*(3), 896–900. https://doi.org/10.1021/es071774j

Karn, B., Kuiken, T., & Otto, M. (2009). Nanotechnology and in situ remediation: A review of the benefits and potential risks. *Environmental Health Perspectives*, *117*(12), 1823–1831. https://doi.org/10.1289/ehp.0900793

Kasel, D., Bradford, S. A., Šimůnek, J., Heggen, M., Vereecken, H., & Klumpp, E. (2013). Transport and retention of multi-walled carbon nanotubes in saturated porous media: Effects of input concentration and grain size. *Water Research*, *47*(2), 933–944. https://doi.org/10.1016/j.watres.2012.11.019

Kätterer, T., Schmied, B., Abbaspour, K. C., & Schulin, R. (2001). Single- and dual-porosity modelling of multiple tracer transport through soil columns: Effects of initial moisture and mode of application. *European Journal of Soil Science*, *52*(1), 25–36. https://doi.org/10.1046/j.1365-2389.2001.00355.x

Kumahor, S. K., de Rooij, G. H., Schlüter, S., & Vogel, H.-J. (2015). Water Flow and Solute Transport in Unsaturated Sand-A Comprehensive Experimental Approach. *Vadose Zone Journal*, *14*(2), vzj2014.08.0105. https://doi.org/10.2136/vzj2014.08.0105

Kumahor, S. K., Hron, P., Metreveli, G., Schaumann, G. E., Klitzke, S., Lang, F., & Vogel, H. J. (2016). Transport of soil-aged silver nanoparticles in unsaturated sand. *Journal of Contaminant Hydrology*, *195*, 31–39. https://doi.org/10.1016/j.jconhyd.2016.10.001

Kumahor, S. K., Hron, P., Metreveli, G., Schaumann, G. E., & Vogel, H. J. (2015). Transport of citrate-coated silver nanoparticles in unsaturated sand. *Science of the Total Environment*, *535*, 113–121. https://doi.org/10.1016/j.scitotenv.2015.03.023

Kuppusamy, S., Palanisami, T., Megharaj, M., Venkateswarlu, K., & Naidu, R. (2016). Reviews of Environmental Contamination and Toxicology. In *Rev Environ Contam Toxicol* (Vol. 236). https://doi.org/10.1007/978-3-319-20013-2

Labud, V., Garcia, C., & Hernandez, T. (2007). Effect of hydrocarbon pollution on the microbial properties of a sandy and a clay soil. *Chemosphere*, *66*(10), 1863–1871. https://doi.org/10.1016/j.chemosphere.2006.08.021

Lecoanet, H. F., & Wiesner, M. R. (2004). Velocity effects on fullerene and oxide nanoparticle deposition in porous media. *Environmental Science and Technology*, *38*(16), 4377–4382. https://doi.org/10.1021/es035354f

Li, J., Rajajayavel, S. R. C., & Ghoshal, S. (2016). Transport of carboxymethyl cellulose-coated zerovalent iron nanoparticles in a sand tank : Effects of sand grain size , nanoparticle concentration and injection velocity. *Chemosphere*, *150*, 8–16. https://doi.org/10.1016/j.chemosphere.2015.12.075

Li, T., Shen, C., Wu, S., Jin, C., & Bradford, S. A. (2020). Synergies of surface roughness and hydration on colloid detachment in saturated porous media: Column and atomic force microscopy studies. *Water Research*, *183*, 116068. https://doi.org/10.1016/j.watres.2020.116068

Liang, Y., Bradford, S. A., Simunek, J., Heggen, M., Vereecken, H., & Klumpp, E. (2013). Retention and remobilization of stabilized silver nanoparticles in an undisturbed loamy sand soil. *Environmental Science and Technology*, *47*(21), 12229–12237. https://doi.org/10.1021/es402046u

Liang, Y., Bradford, S. A., Simunek, J., Vereecken, H., & Klumpp, E. (2013). Sensitivity of the transport and retention of stabilized silver nanoparticles to physicochemical factors. *Water Research*, *47*(7), 2572–2582. https://doi.org/10.1016/j.watres.2013.02.025

Lin, D., Tian, X., Wu, F., & Xing, B. (2010). Fate and Transport of Engineered Nanomaterials in the Environment. *Journal of Environmental Quality*, *39*(6), 1896–1908. https://doi.org/10.2134/jeq2009.0423

Linley, S. (2019). Polymeric Coatings for Targeted Nanoparticle Delivery to Subsurface Contaminants. University of Waterloo.

Linley, S., Holmes, A., Leshuk, T., Nafo, W., Thomson, N. R., Al-Mayah, A., … Gu, F. X. (2019). Targeted nanoparticle binding & detection in petroleum hydrocarbon impacted porous media. *Chemosphere*, *215*, 353–361. https://doi.org/10.1016/j.chemosphere.2018.10.046

Linley, S., Mellage, A., Thomson, N. R., Van Cappellen, P., & Rezanezhad, F. (2021). Spatiotemporal geo-electrical sensing of a Pluronic-coated cobalt ferrite nanoparticle slug in natural sand flow-through columns. *Science of the Total Environment*, *769*, 144522. https://doi.org/10.1016/j.scitotenv.2020.144522

Linley, S., Thomson, N. R., McVey, K., Sra, K., & Gu, F. X. (2020). Factors affecting pluronic-coated iron oxide nanoparticle binding to petroleum hydrocarbon-impacted sediments. *Chemosphere*, *254*, 126732. https://doi.org/10.1016/j.chemosphere.2020.126732

Linley, S., Thomson, N. R., McVey, K., Sra, K., & Gu, F. X. (2020). Influence of Pluronic coating formulation on iron oxide nanoparticle transport in natural and oil-impacted sandy aquifer media. *Canadian Journal of Chemical Engineering*, *98*(3), 642–649. https://doi.org/10.1002/cjce.23650

Liu, D., Johnson, P. R., & Elimelech, M. (1995). Colloid Deposition Dynamics in Flow Through Porous Media: Role of Electrolyte Concentration. *Environmental Science and Technology*, *29*(12), 2963–2973. https://doi.org/10.1021/es00012a012

Louie, S. M., Gorham, J. M., McGivney, E. A., Liu, J., Gregory, K. B., & Hackley, V. A. (2016). Photochemical transformations of thiolated polyethylene glycol coatings on gold nanoparticles. *Environmental Science: Nano*, *3*(5), 1090–1102. https://doi.org/10.1039/c6en00141f

MacKinnon, L. K., & Thomson, N. R. (2002). Laboratory-scale in situ chemical oxidation of a perchloroethylene pool using permanganate. *Journal of Contaminant Hydrology*, *56*(1–2), 49–74. https://doi.org/10.1016/S0169-7722(01)00203-0

Makselon, J., Zhou, D., Engelhardt, I., Jacques, D., & Klumpp, E. (2017). Experimental and Numerical Investigations of Silver Nanoparticle Transport under Variable Flow and Ionic Strength in Soil. *Environmental Science and Technology*, *51*(4), 2096–2104. https://doi.org/10.1021/acs.est.6b04882

Matott, L. S. (2017). Ostrich: An optimization software tool, documentation and user's guide, version 1.6. *State University of New York at Buffalo*.

McCarthy, J. F., & McKay, L. D. (2004). Colloid transport in the subsurface: Past, present, and future challenges. *Vadose Zone Journal*, 3(2), 326-337.

Mitropoulou, P. N., Syngouna, V. I., & Chrysikopoulos, C. V. (2013). Transport of colloids in unsaturated packed columns: Role of ionic strength and sand grain size. *Chemical Engineering Journal*, *232*, 237–248. https://doi.org/10.1016/j.cej.2013.07.093

Molnar, I. L., Sanematsu, P. C., Gerhard, J. I., Willson, C. S., & O'Carroll, D. M. (2016). Quantified Pore-Scale Nanoparticle Transport in Porous Media and the Implications for Colloid Filtration Theory. *Langmuir*, *32*(31), 7841–7853. https://doi.org/10.1021/acs.langmuir.6b01233

Molnar, I. L., Willson, C. S., O'Carroll, D. M., Rivers, M. L., & Gerhard, J. I. (2014). Method for obtaining silver nanoparticle concentrations within a porous medium via synchrotron X-ray computed microtomography. *Environmental Science and Technology*, *48*(2), 1114–1122. https://doi.org/10.1021/es403381s

Mondal, A., Dubey, B. K., Arora, M., & Mumford, K. (2021). Porous media transport of iron nanoparticles for site remediation application: A review of lab scale column study, transport modelling and field-scale application. *Journal of Hazardous Materials*, *403*, 123443. https://doi.org/10.1016/j.jhazmat.2020.123443

Mondal, P. K., Furbacher, P. D., Cui, Z., Krol, M. M., & Sleep, B. E. (2018). Transport of polymer stabilized nano-scale zero-valent iron in porous media. *Journal of Contaminant Hydrology*, *212*(November), 65–77. https://doi.org/10.1016/j.jconhyd.2017.11.004

Morales, V. L., Gao, B., & Steenhuis, T. S. (2009). Grain Surface-Roughness Effects on Colloidal Retention in the Vadose Zone. *Vadose Zone Journal*, *8*(1), 11–20. https://doi.org/10.2136/vzj2007.0171

O'Carroll, D., Sleep, B., Krol, M., Boparai, H., & Kocur, C. (2013). Nanoscale zero valent iron and bimetallic particles for contaminated site remediation. *Advances in Water Resources*, *51*, 104–122. https://doi.org/10.1016/j.advwatres.2012.02.005

Padilla, I. Y., Yeh, T. C. J., & Conklin, M. H. (1999). The effect of water content on solute transport in unsaturated porous media. *Water Resources Research*, *35*(11), 3303–3313. https://doi.org/10.1029/1999WR900171

Park, C. M., Chu, K. H., Heo, J., Her, N., Jang, M., Son, A., & Yoon, Y. (2016). Environmental behavior of engineered nanomaterials in porous media: A review. *Journal of Hazardous Materials*, *309*, 133–150. https://doi.org/10.1016/j.jhazmat.2016.02.006

Petosa, A. R., Jaisi, D. P., Quevedo, I. R., Elimelech, M., & Tufenkji, N. (2010). Aggregation and deposition of engineered nanomaterials in aquatic environments: Role of physicochemical interactions. *Environmental Science and Technology*, *44*(17), 6532–6549. https://doi.org/10.1021/es100598h

Phenrat, T., Cihan, A., Kim, H. J., Mital, M., Illangasekare, T., & Lowry, G. V. (2010). Transport and deposition of polymer-modified Fe0 nanoparticles in 2-D heterogeneous porous media: Effects of particle concentration, Fe 0 content, and coatings. *Environmental Science and Technology*, *44*(23), 9086–9093. https://doi.org/10.1021/es102398e

Phenrat, T., Fagerlund, F., Illangasekare, T., Lowry, G. V., & Tilton, R. D. (2011). Polymer-modified Fe 0 nanoparticles target entrapped NAPL in two dimensional porous media: Effect of particle concentration, NAPL saturation, and injection strategy. *Environmental Science and Technology*, *45*(14), 6102–6109. https://doi.org/10.1021/es200577n

Prédélus, D., Lassabatere, L., Coutinho, A. P., Louis, C., Brichart, T., Slimène, E. Ben, … Angulo-Jaramillo, R. (2014). Tracing Water Flow and Colloidal Particles Transfer in an Unsaturated Soil. *Journal of Water Resource and Protection*, *06*(07), 696–709. https://doi.org/10.4236/jwarp.2014.67067

Prédélus, D., Lassabatere, L., Louis, C., Gehan, H., Brichart, T., Winiarski, T., & Angulo-Jaramillo, R. (2017). Nanoparticle transport in water-unsaturated porous media: effects of solution ionic strength and flow rate. *Journal of Nanoparticle Research*, *19*(3). https://doi.org/10.1007/s11051-017-3755-4

Quinn, J., Geiger, C., Clausen, C., Brooks, K., Coon, C., O'Hara, S., … Holdsworth, T. (2005). Field demonstration of DNAPL dehalogenation using emulsified zero-valent iron. *Environmental Science and Technology*, *39*(5), 1309–1318. https://doi.org/10.1021/es0490018

Rahmatpour, S., Mosaddeghi, M. R., Shirvani, M., & Šimůnek, J. (2018). Transport of silver nanoparticles in intact columns of calcareous soils: The role of flow conditions and soil texture. *Geoderma*, *322*(February), 89–100. https://doi.org/10.1016/j.geoderma.2018.02.016

Raychoudhury, T., Tufenkji, N., & Ghoshal, S. (2012). Aggregation and deposition kinetics of carboxymethyl cellulose-modified zero-valent iron nanoparticles in porous media. *Water Research*, *46*(6), 1735–1744. https://doi.org/10.1016/j.watres.2011.12.045

Raychoudhury, T., Tufenkji, N., & Ghoshal, S. (2014). Straining of polyelectrolyte-stabilized nanoscale zero valent iron particles during transport through granular porous media. *Water Research*, *50*, 80–89. https://doi.org/10.1016/j.watres.2013.11.038

Saleh, N., Phenrat, T., Sirk, K., Dufour, B., Ok, J., Sarbu, T., … Lowry, G. V. (2005). Adsorbed triblock copolymers deliver reactive iron nanoparticles to the oil/water interface. *Nano Letters*, *5*(12), 2489–2494. https://doi.org/10.1021/nl0518268

Saleh, N., Sirk, K., Liu, Y., Phenrat, T., Dufour, B., Matyjaszewski, K., … Lowry, G. V. (2007). Surface modifications enhance nanoiron transport and NAPL targeting in saturated porous media. *Environmental Engineering Science*, *24*(1), 45–57. https://doi.org/10.1089/ees.2007.24.45

Schrick, B., Hydutsky, B. W., Bishop, E. J., Blough, J. L., & Mallouk, T. E. (2004). Zero-valent metal nanoparticles for soil and groundwater remediation. *American Chemical Society*, *228*(1), 2187–2193.

Shang, J., Flury, M., Chen, G., & Zhuang, J. (2008). Impact of flow rate, water content, and capillary forces on in situ colloid mobilization during infiltration in unsaturated sediments. *Water Resources Research*, *44*(6), 1–12. https://doi.org/10.1029/2007WR006516

Shapiro, S. S. & Wilk, M. B. (1965). "An Analysis of Variance Technique for Normality (Complete Samples)". Biometrika 52, pp. 591-611.

Šimůnek, J., & van Genuchten, M. T. (2008). Modeling Nonequilibrium Flow and Transport Processes Using HYDRUS. *Vadose Zone Journal*, *7*(2), 782–797. https://doi.org/10.2136/vzj2007.0074

Šimůnek, J., van Genuchten, M. T., & Šejna, M. (1999). *The HYDRUS Software Package for Simulating the Two- and Three-Dimensional Movement of Water, Heat, and Multiple Solutes in Variably-Saturated Porous Media*.

Sirivithayapakorn, S., & Keller, A. (2003). Transport of colloids in unsaturated porous media: A pore-scale observation of processes during the dissolution of air-water interface. *Water Resources Research*, *39*(12). https://doi.org/10.1029/2003WR002487

Sridevi, V., & Lakshmi, P. K. S. (2013). Role of NZVI, Metal oxide and carbon nanotube for ground water cleanup and their comparison- An overview. *Proceedings of the International Conference on "Advanced Nanomaterials and Emerging Engineering Technologies", ICANMEET 2013*, (lI), 737–742. https://doi.org/10.1109/ICANMEET.2013.6609401

Thomson, N.R., 2019. 1DUSAT: A Flexible One-Dimensional Unsaturated Flow and Solute Transport Model. University of Waterloo. https://uwaterloo.ca/scholar/nthomson/models

Tolson, B. A., & Shoemaker, C. A. (2007). Dynamically dimensioned search algorithm for computationally efficient watershed model calibration. *Water Resources Research*, *43*(1). https://doi.org/10.1029/2005WR004723

Torkzaban, S., Hassanizadeh, S. M., Schijven, J. F., de Bruin, H. A. M., & de Roda Husman, A. M. (2006). Virus Transport in Saturated and Unsaturated Sand Columns. *Vadose Zone Journal*, *5*(3), 877–885. https://doi.org/10.2136/vzj2005.0086

Torkzaban, S., & Bradford, S. A. (2016). Critical role of surface roughness on colloid retention and release in porous media. *Water Research*, *88*, 274–284. https://doi.org/10.1016/j.watres.2015.10.022

Torkzaban, S., Bradford, S. A., van Genuchten, M. T., & Walker, S. L. (2008). Colloid transport in unsaturated porous media: The role of water content and ionic strength on particle straining. *Journal of Contaminant Hydrology*, *96*(1–4), 113–127. https://doi.org/10.1016/j.jconhyd.2007.10.006

Torkzaban, S., Kim, Y., Mulvihill, M., Wan, J., & Tokunaga, T. K. (2010). Transport and deposition of functionalized CdTe nanoparticles in saturated porous media. *Journal of Contaminant Hydrology*, *118*(3–4), 208–217. https://doi.org/10.1016/j.jconhyd.2010.10.002

Tosco, T., Petrangeli Papini, M., Cruz Viggi, C., & Sethi, R. (2014). Nanoscale zerovalent iron particles for groundwater remediation: A review. *Journal of Cleaner Production*, *77*, 10–21. https://doi.org/10.1016/j.jclepro.2013.12.026

Tratnyek, P. G., & Johnson, R. L. (2006). Nanotechnologies for environmental cleanup. *Nano Today*, *1*(2), 44–48. https://doi.org/10.1016/S1748-0132(06)70048-2

Treumann, S., Torkzaban, S., Bradford, S. A., Visalakshan, R. M., & Page, D. (2014). An explanation for differences in the process of colloid adsorption in batch and column studies. *Journal of Contaminant Hydrology*, *164*, 219–229. https://doi.org/10.1016/j.jconhyd.2014.06.007

Tufenkji, N., & Elimelech, M. (2004). Deviation from the classical colloid filtration theory in the presence of repulsive DLVO interactions. *Langmuir*, *20*(25), 10818–10828. https://doi.org/10.1021/la0486638

van Genuchten, M. T. (1980). A Closed-form Equation for Predicting the Hydraulic Conductivity of Unsaturated Soils. Soil Science Society of America Journal, 44(5), 892–898. https://doi.org/10.2136/sssaj1980.03615995004400050002xan Genuchten, M. T. (1980). A Closed-form Equation for Predicting the Hydraulic Conductivity of Unsaturated Soils. *Soil Science Society of America Journal*, *44*(5), 892–898. https://doi.org/10.2136/sssaj1980.03615995004400050002x

Velimirovic, M., Bianco, C., Ferrantello, N., Tosco, T., Casasso, A., Sethi, R., … Hofmann, T. (2020). A large-scale 3D study on transport of humic acid-coated goethite nanoparticles for aquifer remediation. *Water (Switzerland)*, *12*(4). https://doi.org/10.3390/W12041207

Wan, J., & Wilson, J. L. (1994). Colloid transport in unsaturated porous media. *Water Resources Research*, *30*(4).

Wang, Y., Becker, M. D., Colvin, V. L., Abriola, L. M., & Pennell, K. D. (2014). Influence of residual polymer on nanoparticle deposition in porous media. *Environmental Science and Technology*, *48*(18), 10664–10671. https://doi.org/10.1021/es500523p

Yao, K. M., Habibian, M. T., & O'Melia, C. R. (1971). Water and Waste Water Filtration: Concepts and Applications. *Environmental Science and Technology*, *5*(11), 1105–1112. https://doi.org/10.1021/es60058a005

Yecheskel, Y., Dror, I., & Berkowitz, B. (2018). Silver nanoparticle (Ag-NP) retention and release in partially saturated soil: Column experiments and modelling. *Environmental Science: Nano*, *5*(2), 422–435. https://doi.org/10.1039/c7en00990a

Zhang, W., Morales, V. L., Cakmak, M. E., Salvucci, A. E., Geohring, L. D., Hay, A. G., … Steenhuis, T. S. (2010). Colloid transport and retention in unsaturated porous media: Effect of colloid input concentration. *Environmental Science and Technology*, *44*(13), 4965–4972. https://doi.org/10.1021/es100272f

Appendix A

Supplementary Materials for Chapter 2

A.1 Binding Batch Studies

About 15 g of sediment (Borden sand (BS), synthetic silty sand (SSS), or oil-impacted BS) was added to 20 mL scintillation vials, followed by 10 mL of aqueous nanoparticle suspension diluted by a factor of 100 with Millipore DI water. The vials were allowed to sit at room temperature for 48 h. The nanoparticle suspension was then collected by filtration (Whatman glass microfiber filter, Grade 934-AH) and analysed by ICP-OES for the measurements of total iron or cobalt concentration. All batch tests were performed in triplicate.

A.2 Calibrated Br^- transport model parameters

The estimated total porosity for all saturated and gravity-drained columns was ~0.30 and slightly higher in the unsaturated columns (0.33 and 0.35) due to different packing. The fraction of mobile porosity (f_s) was consistent for all experimental Sets at ~0.9 (slightly higher in the unsaturated columns (0.93 and 0.94)). The calibrated first-order mass transfer rate coefficient for Br^- (γ_{Br}) between the mobile and immobile regions varied from 1 x 10^{-5} to 3 x 10^{-5} /s, except for Set D which was lower at 0.7 x 10^{-5} /s. The lower value for Set D is presumably related to the lower flow rate used in these trials which gives rise to decreased connectivity between the two regions. The dispersivity value for all the saturated, suction-drained and unsaturated columns ranged from 1.6 x 10^{-4} to 4.0 x 10^{-4} m, except for the dispersivity value of the SSS-packed columns which was higher (11.0 ± 4 x 10^{-4} m) reflecting an increase in velocity variations as a result of the increased silt and clay content. The similar dispersivity value for the control column and the oil-impacted zone of Set F1 indicates that the crude oil did not have a significant impact on variations in pore water velocity.

A.3 Depth-dependant straining

The calibrated straining rate coefficient, k_{str} , was $3.0 \pm 0.6 \times 10^{-4}$ /s which is similar to the value reported by Linley et al. (2021) for same CoFe-NPs (and same coating formulation) in saturated conditions where attachment by physisorption and straining caused by aggregation were suggested as the underlying causes. Despite the small size range of the CoFe-NPs (below the straining threshold), it is possible that NP aggregation occurred. Specifically, the Pluronic coating may have been removed from the NP core due to hydrogen bonding interactions between the oxygen in the PEO chain and acidic metal oxide surface groups present, resulting in destabilization and aggregation of the NPs (Linley et al., 2020a). In addition, the presence of air phase results in increased CoFe-NPs retention (i.e., straining and attachment to AWIs) as previously discussed.

Table A-1. Estimated attached NP mass for different sediments and NP formulations from batch binding tests.

Aquifer material	NP formulation	Measured $M_{attached}$	±95% CI	
			lower limit	upper limit
		[mg/kg]	[mg/kg]	[mg/kg]
BS	Transport	7.8 ± 2.3	6.19	9.32
SSS	Transport	37.3 ± 2.4	34.16	40.45
BS	Binding	8.2 ± 0.6	7.57	8.91
Impacted-BS	Binding	25.9 ± 2.1	23.57	28.32

Table A-2. Estimated hydraulic parameters for all column experiments.

Label	$S_{wr}{}^{1}$	ϕ_T	α	n	R^2
	[-]	[-]	[1/m]	[-]	
B1	0.22	0.30	14.50	1.14	0.97
B2	0.21	0.31	15.00	1.40	0.95
B3	0.22	0.31	15.00	1.20	0.98
D	0.22	0.30	15.00	1.30	0.93
E1	0.22	0.31	11.00	1.17	0.98
E2	0.20	0.31	15.00	1.30	0.94
F1	0.20	0.33	15.00	1.30	0.99
F2	0.20	0.35	15.00	1.30	0.93

[1] Residual water saturation = $\phi_{residual} / \phi_T$

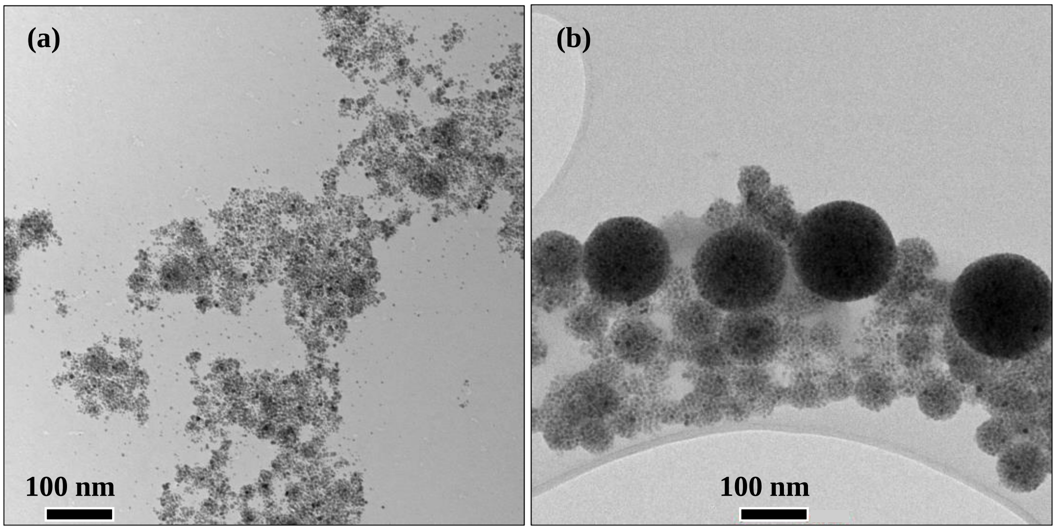

Figure A-1. TEM image of (a) Fe-NP with 10 g/L Pluronic (transport formulation) and (b) CoFe-NP with 2.5 g/L Pluronic (binding formulation).

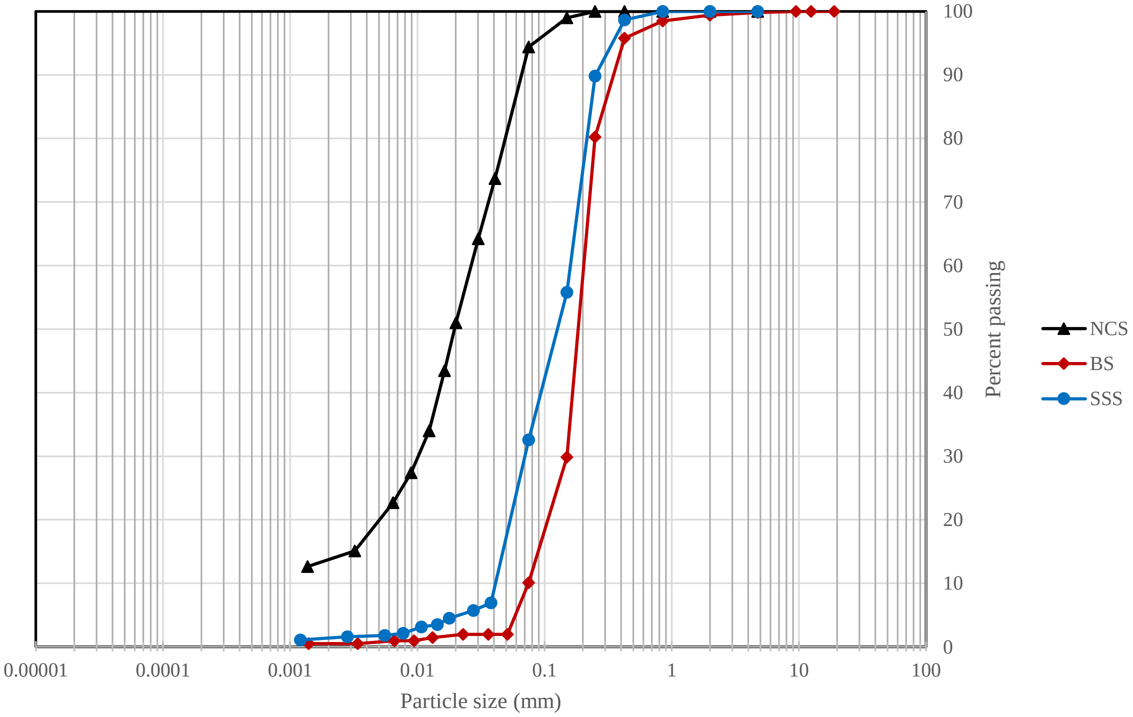

Figure A-2. Particle size distributions curves.

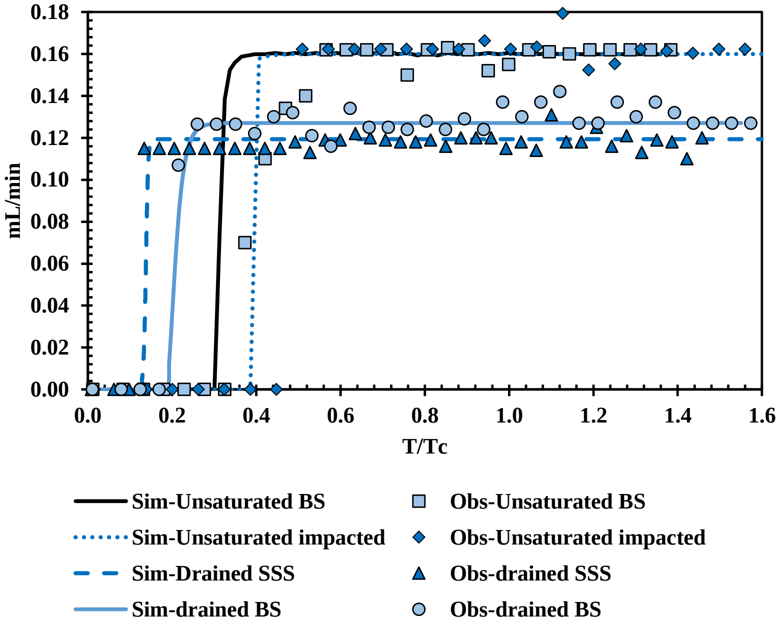

Figure A-3. Representative observed and simulated flow profiles for a suction-drained BS (B2) and SSS column (E1), and for an unsaturated BS (F2) and crude oil-impacted column (F1).

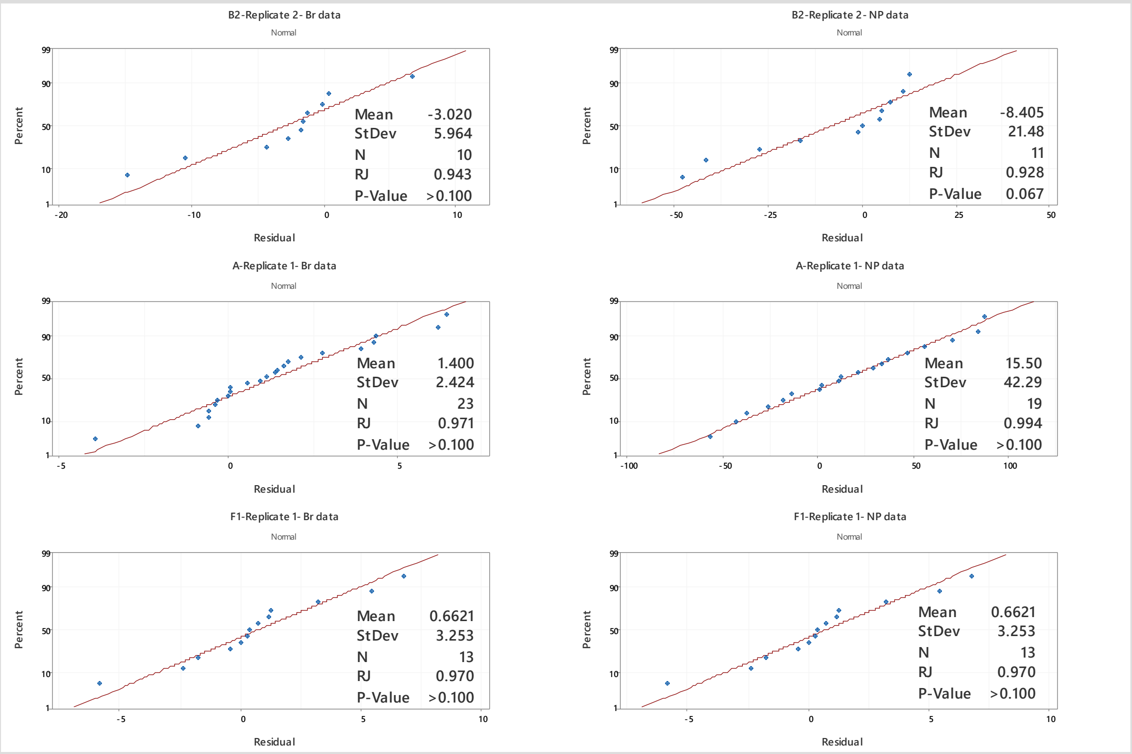

Figure A-4. Examples of residuals plots from Br$^-$ and NP data from Set B2, Set A, and Set F1. Normality was deemed acceptable for *p*-value > 0.05.

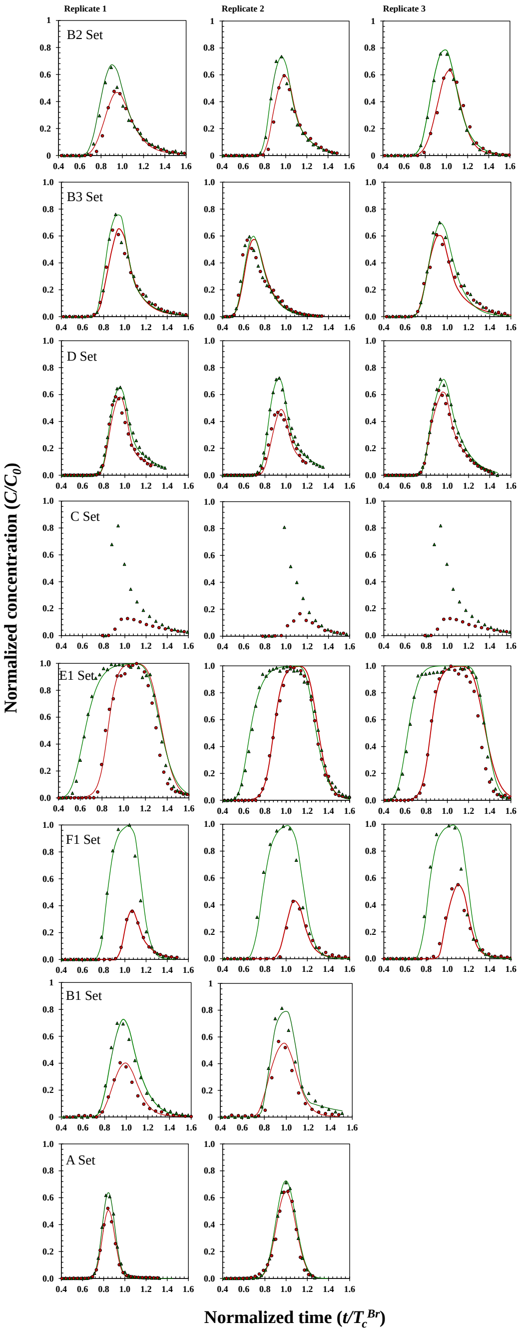

Figure A-5. Observed (symbols) and simulated (solid lines) normalized BTCs of Br$^-$ and Fe-NPs for all trials. All sets were performed in triplicate, except for Set E2 and Set F2 which were performed in one column as a control for Sets E1 and Set F1, respectively. Data for trials that were considered outliers are not shown here (i.e., Trial 3 of Set A and Set B1).

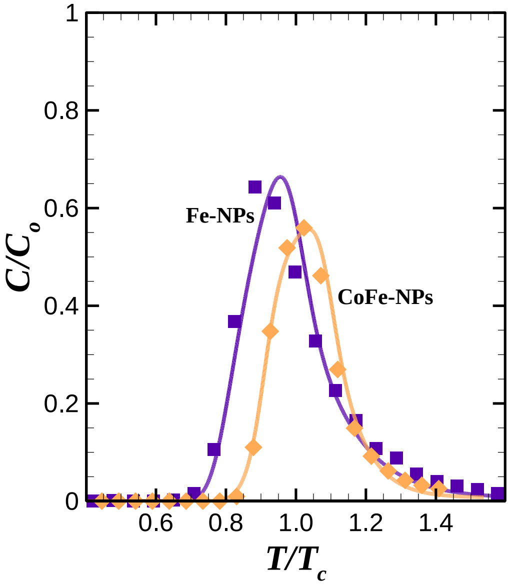

Figure A-6. An example of observed (symbols) and simulated (solid lines) normalized BTCs of CoFe-NP for non-impacted unsaturated column (denoted as control column) (Set F2) and Fe-NPs for gravity-drained column (Set B3) (non-impacted). Experimental condition for both sets was nearly identical; Columns were packed with sandy aquifer material (BS), the injection flowrate of 0.14 mL/min, and NP injection dosage of 10 mg were used.

Appendix B
Supplementary Materials for Chapter 3

B.1 Solid Digestion Method and Validation

Each excavated sediment subsample was oven dried at 90 ^{o}C for 12 hrs to remove moisture, then homogenized, and 1 g was transferred into a 50 mL digestion tube (VWR, Mississauga, Ontario). The crude oil (if any) and NPs present were digested by adding 10 mL of concentrated HNO_3 (70 %) to each tube which was then heated at ~95 ^{o}C for 30 min. After cooling, 5 mL of concentrated HNO_3 (70 %) was added and the tube re-heated to 95 ^{o}C until the reaction was complete (indicated by lack of brown smoke) and the solution volume reduced to ~5 mL. After the tube was cooled, 3 mL of H_2O_2 (30%) was added and gently heated at 85 to 90 ^{o}C until effervescence was observed. Once effervescence subsided, the tube was removed from the heating block and allowed to cool. When cooled, an additional 3 mL of H_2O_2 was added and the tube heated (95 ^{o}C) until effervescence was insignificant, and the solution volume was reduced to 5 mL. To ensure complete digestion of the NPs, 10 mL of concentrated HCl (37 %) was added and the tube was heated (95 ^{o}C) until the volume was reduced to 5 mL. The digestate was then diluted by Millipore water to a total volume of 10 mL and filtered (Whatman No. 41). The filtrate was analysed using ICP-OES to estimate Co_T which was then used to calculate the mass of CoFe-NPs in each sediment subsample (mg of CoFe-NPs per kg of dry sediment).

To validate this solid digestion method, 10 g of clean BS was spiked with 0.08 mg of CoFe-NPs, and three subsamples (1 g each) were digested using the above method. Three samples from non-spiked BS were also digested and analyzed as control. The remaining portions of the spiked and non-spiked BS samples were sent to an external laboratory (ALS Environmental, Waterloo, Canada) for analyses using EPA 200.2/6020A method. This method is for digestion of metals in soil using a collision/reaction cell (CRC) followed by ICP-MS measurements. Briefly in this method, sediment samples are dried, disaggregated, and sieved (2 mm). The < 2 mm fraction is ground to pass through a 0.355 mm sieve, and then leachable metals in the < 2 mm fraction were solubilized by heated digestion with nitric and hydrochloric acids. The average recovered mass of CoFe-NPs reported by the external lab was 0.09±0.02 mg while the method used in this study yielded a value of 0.08±0.0001 mg. The near identical values suggest that the method used in this study is accurate for the intended purpose.

B.2 Binding Batch Studies

Two (2) % wt. crude oil-impacted Borden sand was prepared by mixing an adequate amount of moist BS (~0.2 v/v water content) with crude oil heated to 60 °C, and homogenized by stirring. Then 15 g of the mixture was added to 20 mL scintillation vials, followed by 10 mL of aqueous NP suspension diluted by a factor of 100 with Millipore water. The vials were left at either room temperature for 48 h. The same process was repeated with clean and dried Borden sand. The NP suspension was then collected by filtration (Whatman glass microfiber filter, Grade 934-AH) and analysed by ICP-OES. All batch tests were performed in triplicate.

Table B-1. Estimated attached NP mass from batch binding tests for crude-oil impacted and non-impacted Borden sand (BS) and different NP formulations.

Material	NP formulation	$M_{attached}$	±95% CI	
		[mg/kg]	lower limit [mg/kg]	upper limit [mg/kg]
BS	Iron oxide	7.8 ± 2.3	6.19	9.32
BS	Cobalt ferrite	8.2 ± 0.59	7.37	8.91
Impacted-BS	Cobalt ferrite	25.9 ± 2.10	23.57	28.32

Table B-2. Estimated hydraulic parameters.

Exp. ID	Material	S_{wr}^2 [-]	ϕ_T [-]	α [1/m]	*n* [-]	R^2
Tracer	Non-Impacted	0.22	0.32	14.00	1.65	0.95
	BS	0.22	0.32	14.00	1.60	0.93
Binding	Non-Impacted BS[1]	0.22	0.27	14.00	1.30	0.97
	Impacted BS[1]	0.21	0.28	15.00	1.32	

1. Non-impacted BS (Borden sand) is used in Zone 1 and 3, Impacted BS is used in Zone 2. The column was discretized into different zones for model simulation. See Figure B-4 for the location of each zone along the domain.
2. Residual water saturation = $\phi_{residual} / \phi_T$

Table B-3. Lateral distribution of retained CoFe-NPs in each layer within impacted zone

Height	Average $M_{retained}$ [1]	Maximum $M_{retained}$	Location of maximum $M_{retained}$	TPH
[m]	[mg/kg]	[mg/kg]	[-]	[mg/kg]
1.00	17.7±1.7	19.3	N	7700
0.94	19.0±2.5	22.1	E	7800
0.89	23.0±0.9	24.2	W	8000
0.85	21.0±2.5	24.7	S	8300
0.83	18.5±3.2	22.9	S	4800

1. $M_{retained}$: Retained concentration of CoFe-NPs in sediment (estimated based on solid digestion and ICP-OES method (see B.1 for details)

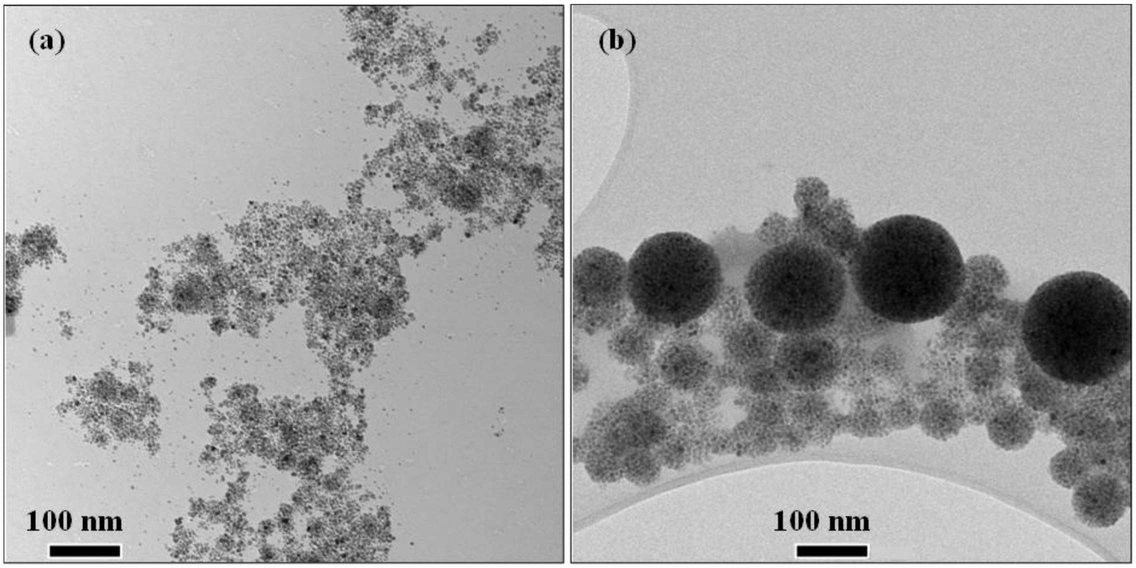

Figure B-4. TEM image of (a) Fe-NPs with transport formulation coating (10 g/L Pluronic) and (b) CoFe-NPs with binding formulation coating (2.5 g/L Pluronic).

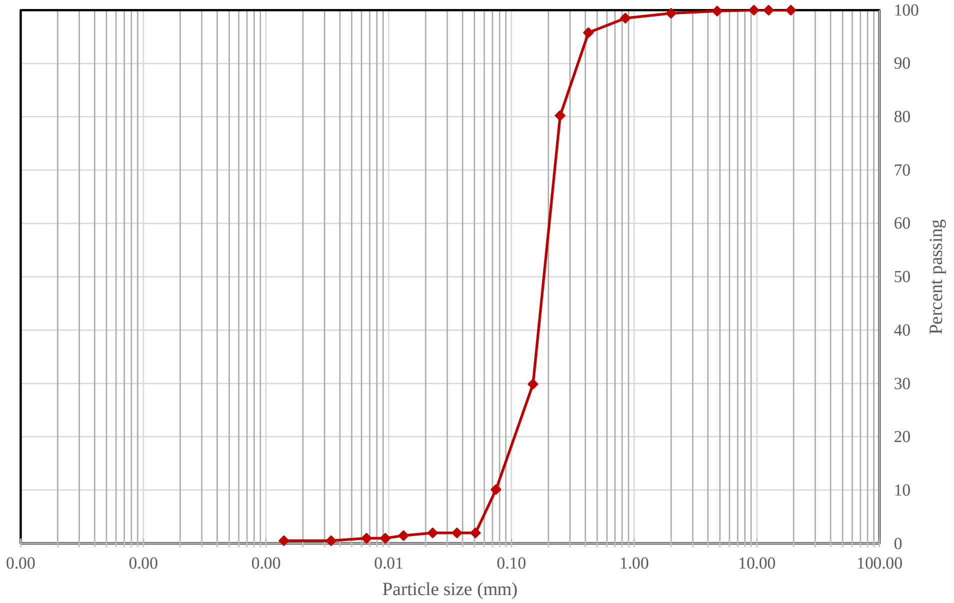

Figure B-5. Particle size distribution curve of BS sediment.

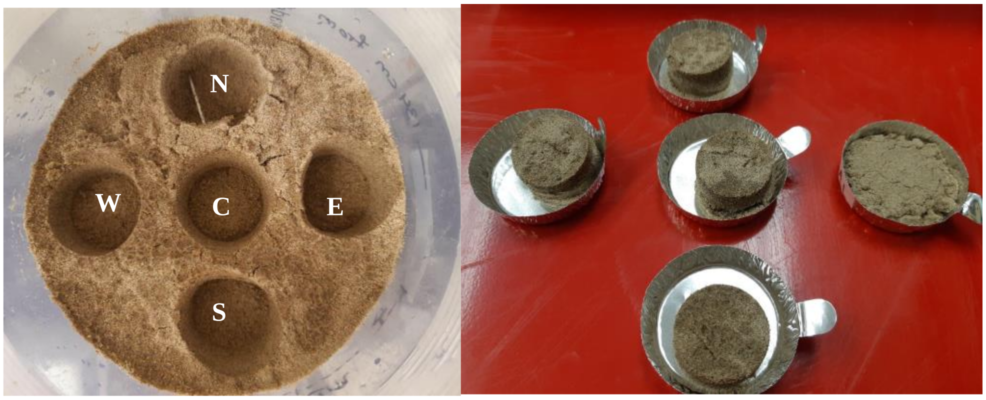

Figure B-6. Subsample excavation from the column center (C), and from the four major compass directions (north, east, south, and west). 1-cm thick lifts were used in crude oil source zone, and 2-cm thick lifts elsewhere.

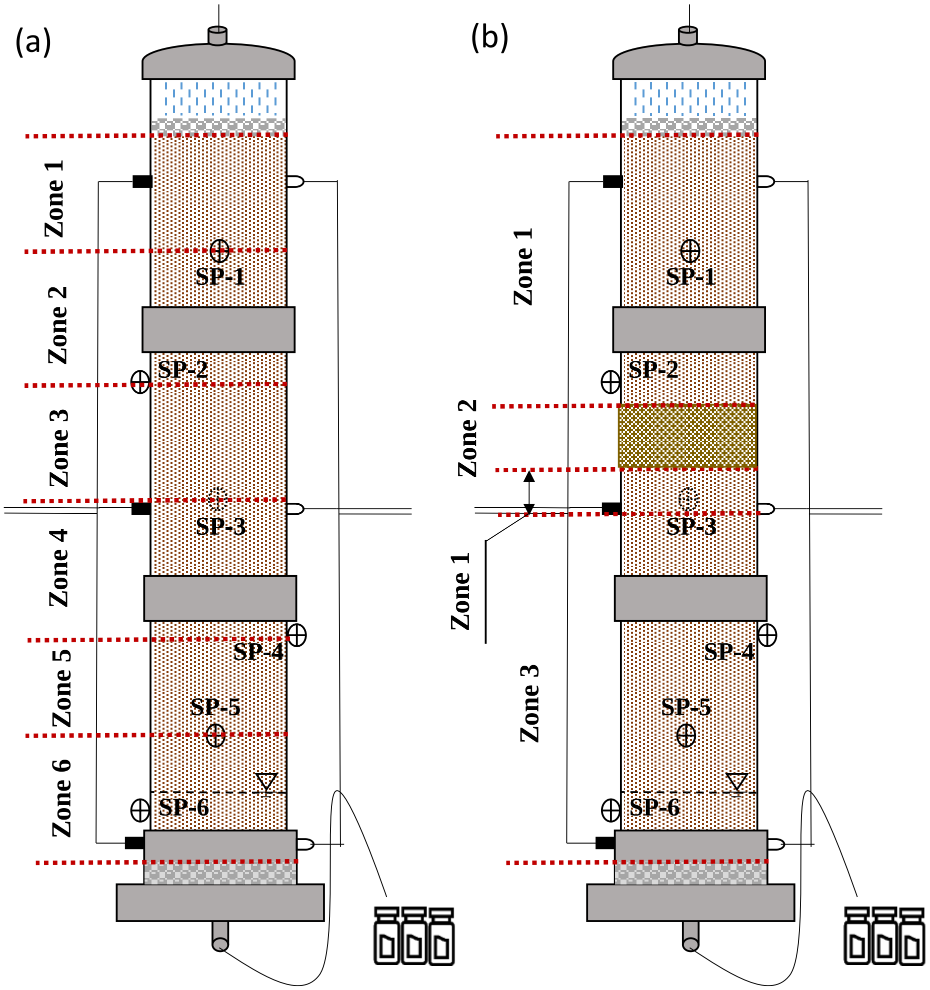

Figure B-4. Division of the model domain for parameter calibration for (a) Fe-NP experiment, and (b) CoFe-NP experiment.

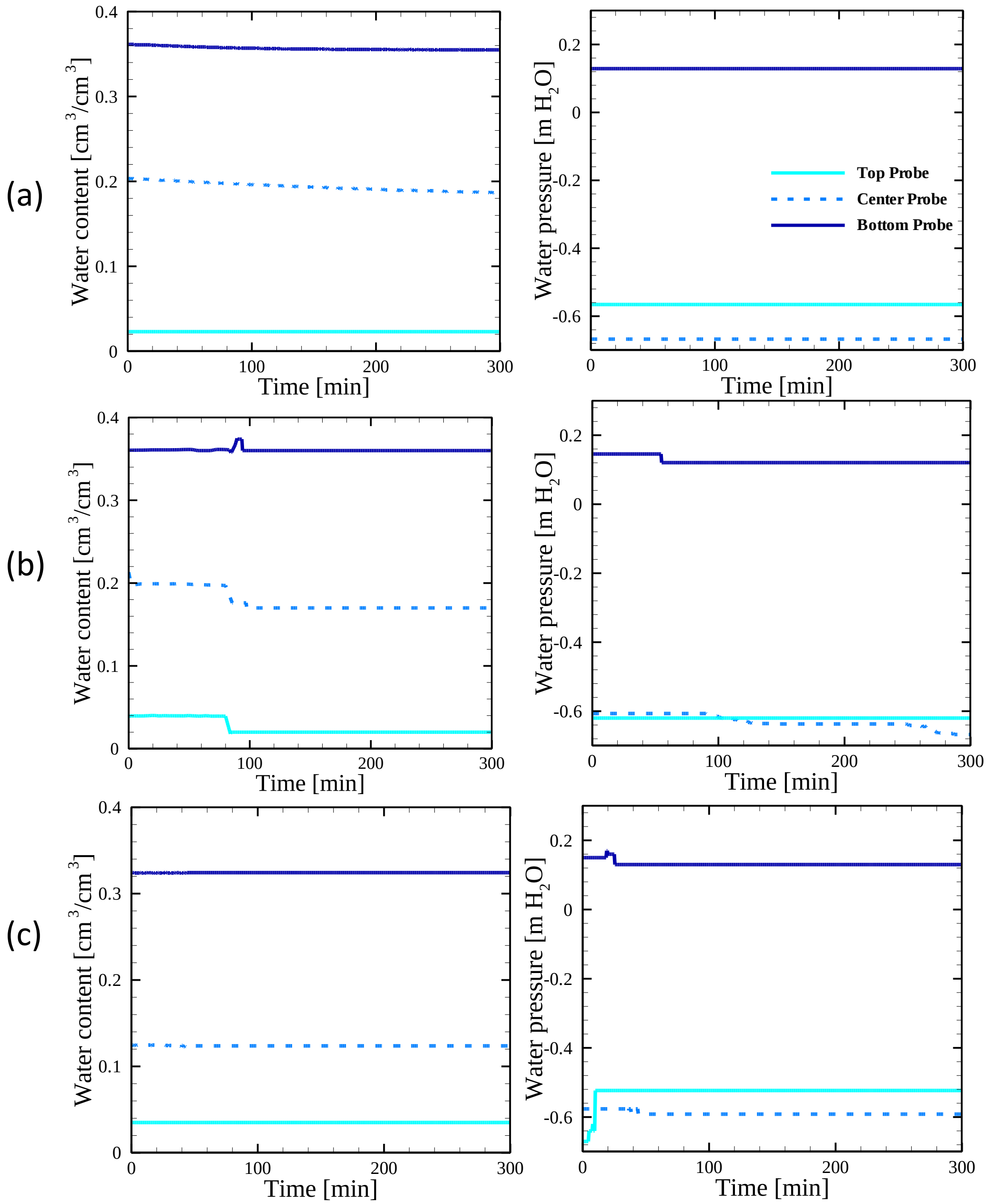

Figure B-5. Volumetric water content and water pressure data ~300 minutes prior to the start of each experiment from (a) tracer test, (b) Fe-NP transport experiment, and (c) CoFe-NP transport and binding experiment.

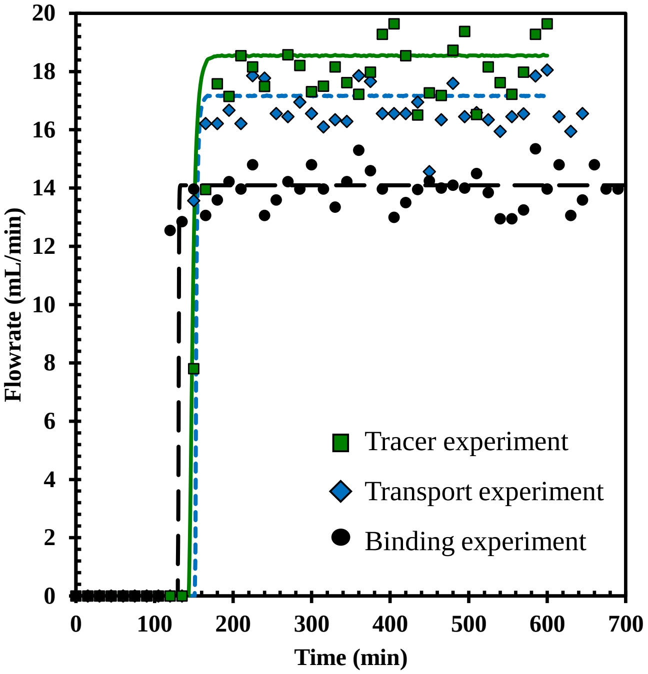

Figure B-6. Effluent flowrate profile from the tracer, Fe-NP transport, CoFe-NP transport and binding experiments.

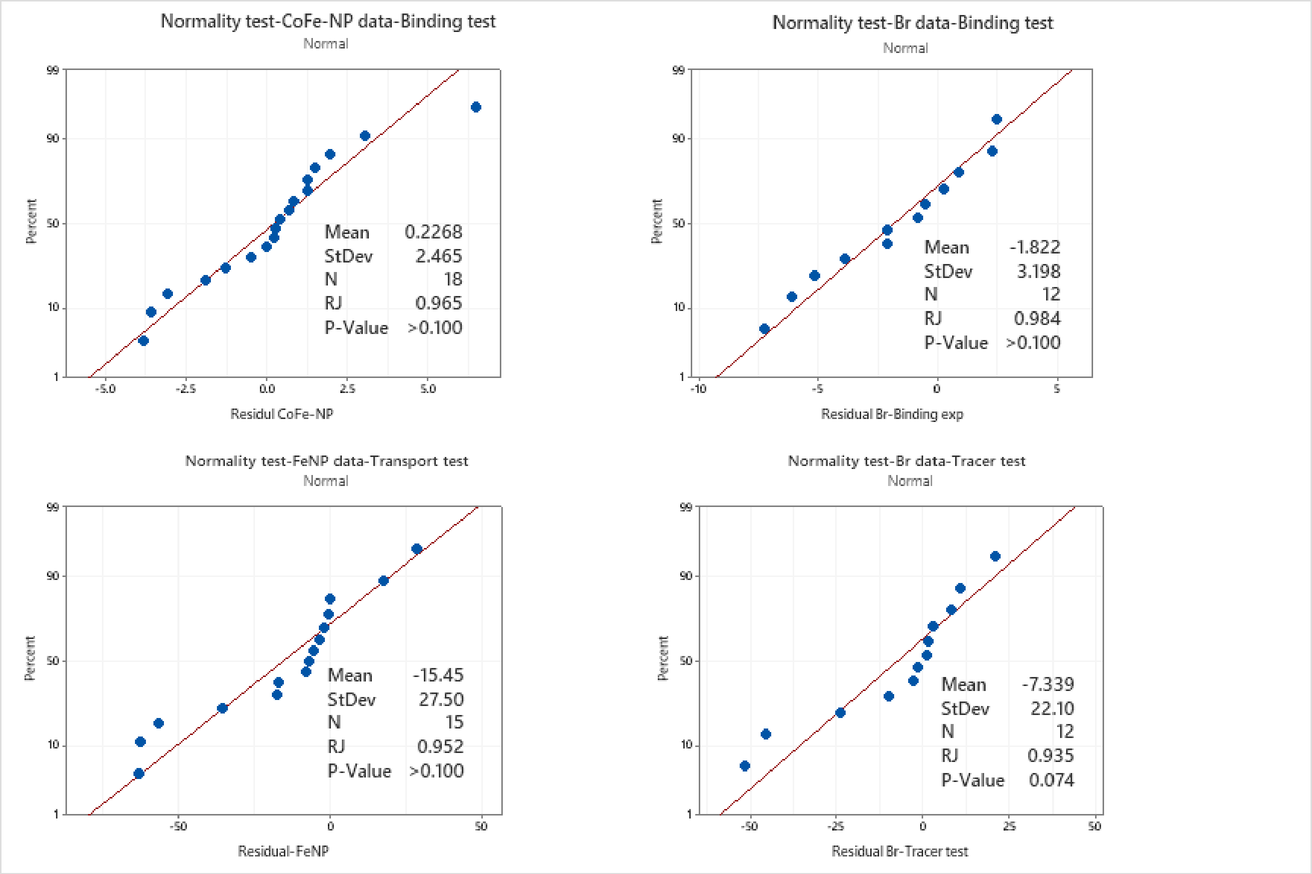

Figure B-7. Normality test for residuals from effluent Br$^-$ and NP data for tracer, Fe-NP transport, and CoFe-NP transport and binding experiments. Normality deemed acceptable for $p > 0.05$.

Figure B-8. Porous needle of a solution sampler clogged by CoFe-NPs (black areas) (SP-1 and SP-2) during the CoFe-NP transport and binding experiment. For the binding experiment, it was found that the CoFe-NPs had a physical interaction with the samplers (SP-1 and SP-2), which caused complete clogging of the porous needle. No interactions were observed between the porous needle in the Fe-NPs transport experiment. Linley (2019) reported that the only difference between the CoFe-NPs (lower coating concentration) and the Fe-NPs (higher coating concentration) is a larger morphology of CoFe-NPs (Figure B-1). Since most of the CoFe-NPs were retained in the crude-oil zone, and less NP mass passed below this zone, aqueous samples where able to be collected from the samplers located below the crude oil zone; however, the representativeness of these samples of the pore water concentration is uncertain.

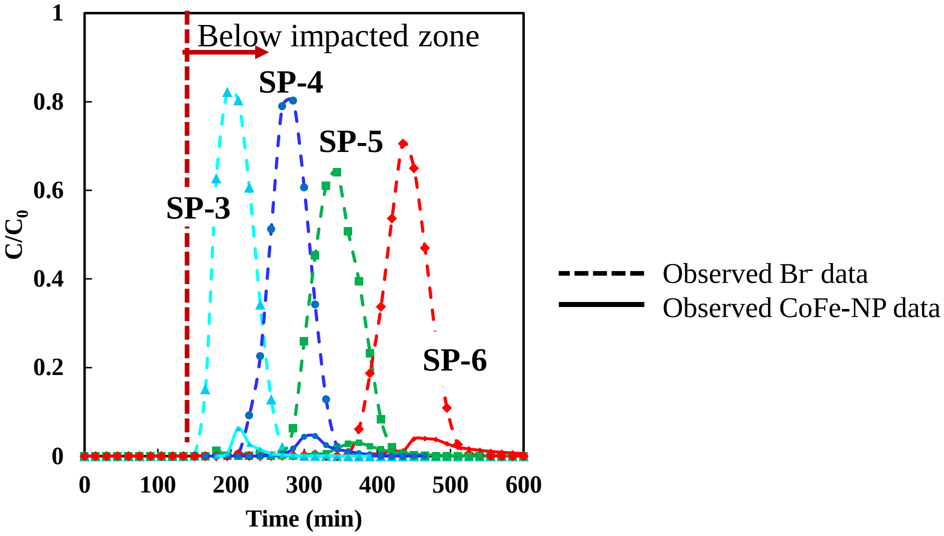

Figure B-9. Observed BTCs of tracer and CoFe-NPs from samplers at different locations along the column.

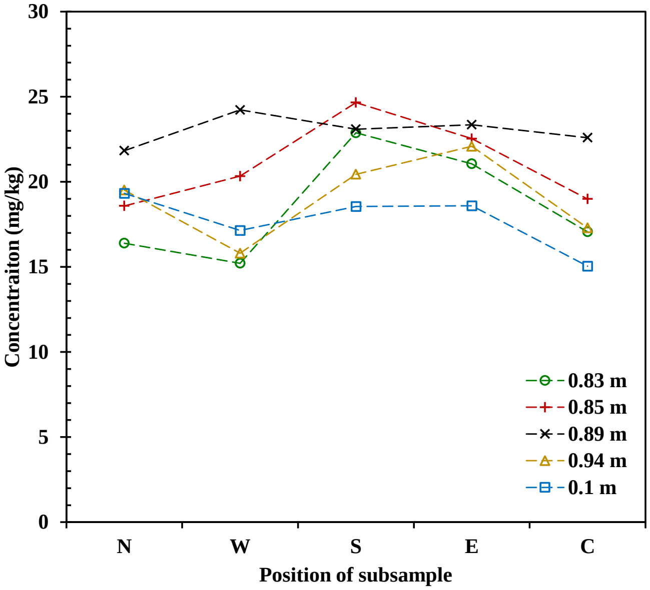

Figure B-10. Estimated concentration of retained CoFe-NPs (mg/kg) at different positions (center and the four major compass directions) across a 1-cm thick lift at five vertical locations within the crude oil source zone.

Appendix C

Supplementary Materials for Chapter 4

C.1 Solid Digestion Method and Validation

Each sediment subsample was oven dried at 90 ^oC for 12 hrs to remove moisture, then homogenized, and 1 g of the sample was transferred into a 50 mL digestion tube (VWR, Mississauga, Ontario). The oil and NPs present in the sample were digested by adding 10 mL of concentrated HNO_3 (70 %) to each tube which was then heated at ~95 ^oC for 30 min. After cooling, 5 mL of concentrated HNO_3 (70 %) was added and the tube re-heated to 95 ^oC until the reaction was complete (indicated by lack of brown smoke) and the solution volume reduced to ~5 mL. After the tube was cooled, 3 mL of H_2O_2 (30%) was added and gently heated at 85 to 90 ^oC until effervescence was observed. Once effervescence subsided, the tube was removed from the heating block and allowed to cool. When cooled, an additional 3 mL of H_2O_2 was added and the tube heated (95 ^oC) until effervescence was insignificant, and the solution volume was reduced to 5 mL. To ensure complete digestion of the NPs, 10 mL of concentrated HCl (37 %) was added and the tube was heated (95 ^oC) until the volume was reduced to 5 mL. The digestate was then diluted by Millipore water to a total volume of 10 mL and filtered (Whatman No. 41). The filtrate was analysed by ICP-OES to estimate Co_T which was used to calculate the mass of NPs in each sediment lift (mg of NP per kg of sediment).

For the validation of the digestion method, our estimated NP concentration in sediments was compared to the estimated values for the same sediment samples by an external laboratory; For this purpose, approximately 10 g of clean sand was spiked with known mass of NP aqueous suspension and 3 samples (1-g each) were taken as spiked sand and digested using the EPA Method used in this study and analysed by ICP-OES. 3 Samples from non-spiked BS were also digested and analysed as control. The remaining of the spiked and non-spiked BS samples were sent to an external laboratory (ALS environmental, Waterloo, Canada), which operated EPA 200.2/6020A method. This method is a digestion of metal in soil using Collision / Reaction Cell (CRC) followed by ICP-MS measurements. Briefly in this method, sediment samples were dried, disaggregated, and sieved (2 mm). For tests intended to support Ontario regulations, the <2mm fraction was grounded to pass through a 0.355 mm sieve. Strong Acid Leachable Metals in the <2mm fraction were solubilized by heated digestion with nitric and hydrochloric acids.

The injected mass of NPs to the 10-g sediment samples (NP spiked or non-spiked) was 0.08 mg. The average recovered mass of NP from these samples was 0.09±0.02 mg analysed by external lab (ALS) and 0.08±0.0001 mg analysed by our solid digestion method, which are nearly identical. In addition to validity, the mass of NP added to the sediment samples was identical to the mass of NPs recovered from the samples using the solid digestion method which shows the reproducibility and accuracy of the method used.

C.2 Binding Batch Studies

Batch binding test was conducted by adding ~15 g of sediment (clean or crude oil-impacted sediments) to 20 mL scintillation vials, followed by 10 mL of aqueous nanoparticle suspension (diluted by a factor of 100 with Millipore DI water). The vials were allowed to sit at room temperature for 48 h. The nanoparticle suspension was then collected by filtration (Whatman glass microfiber filter, Grade 934-AH) and analysed by ICP-OES. All batch tests were performed in triplicate.

Table C-1. Estimated attached CoFe-NP mass from batch binding tests for crude-oil impacted and non-impacted Borden sand (BS).

Material	S_{max}	±95% CI	
		lower limit	upper limit
	[mg/kg]	[mg/kg]	[mg/kg]
BS	8.2 ± 0.6	7.37	8.91
2% wt. oil-impacted BS	25.9 ± 2.1	23.57	28.32
4% wt. oi-impacted BS	29.5 ± 2.4	26.74	32.21

Table C-2. Estimated hydraulic parameters (used flow data from tracer experiment).

Zone ID	Material	θ_r	ϕ_r	α	n	K_s
		[-]	[-]	[1/m]	[-]	[m/s]×10^{-5}
3	Moist BS	0.06	0.32	14.00	1.30	7.20
4	2% wt. oil-impacted BS	0.06	0.28	15.00	1.32	1.70
5	4% wt. oi-impacted BS	0.06	0.34	15.00	1.30	1.0
2	Wet packed BS	0.06	0.3	14.00	1.30	7.20

Table C-3. Estimated hydraulic parameters (used flow data from CoFe-NP experiment).

Zone ID	Material	θ_r	ϕ_T	α	n	K_s
		[-]	[-]	[1/m]	[-]	[m/s]×10^{-5}
3	Moist BS	0.06	0.33	14.00	1.30	7.20
4	2% wt. oil-impacted BS	0.06	0.28	15.00	1.32	1.50
5	4% wt. oi-impacted BS	0.06	0.35	15.00	1.30	0.90
2	Wet packed BS	0.06	0.31	14.00	1.30	7.20

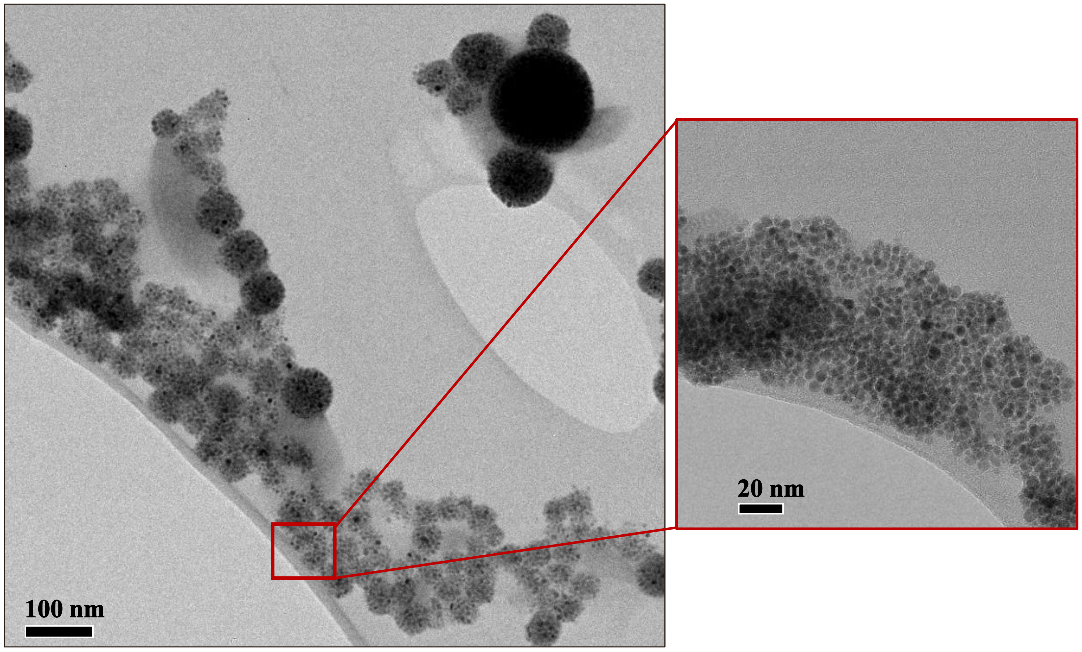

Figure C-1. TEM images of cobalt iron nanoparticles (CoFe-NPs; 2.5 g/L Pluronic coating concentration) at two magnifications.

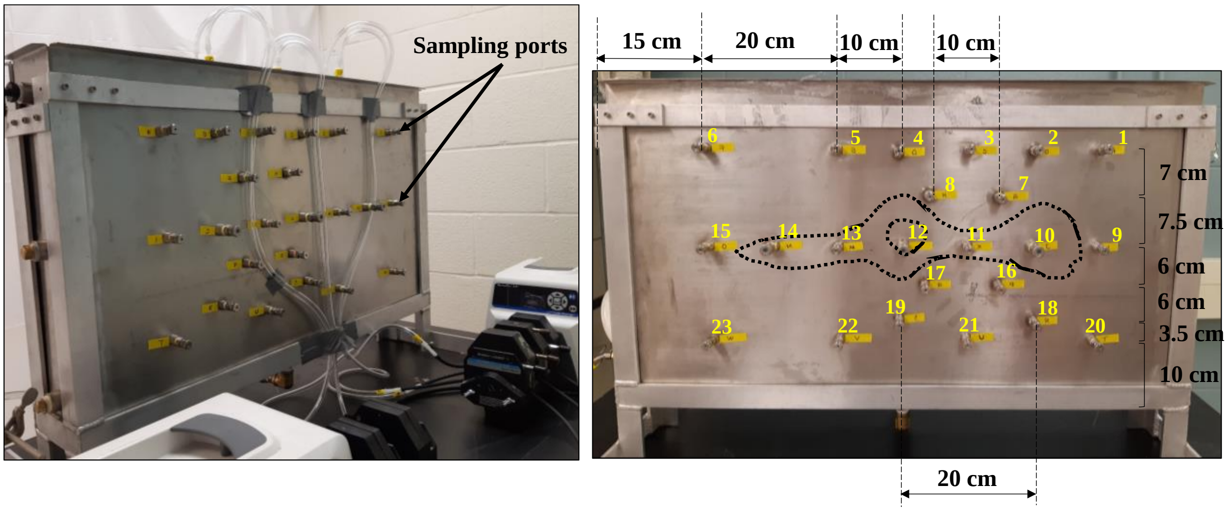

Figure C-2. Spatial distribution of the sampling ports at the back of the sand tank. Aqueous samples were manually collected during the experiments from each sampling port (every 15 minutes) using a 3-mL syringe with hypodermic needle and then transferred into 5-mL polypropylene cryogenic vials.

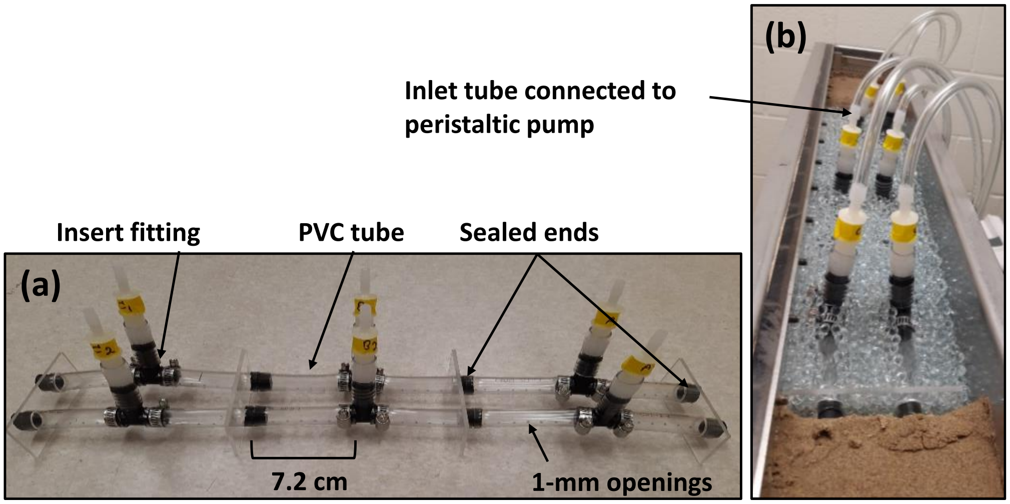

Figure C-3. Infiltration gallery comprised of (a) an injection system made from twelve pieces of flexible PVC tubing (1.27 cm ID, 7.2 cm length) with ~1-mm openings drilled at 1-cm increments along the tube length. One end of each tube was sealed, and the other end attached to a 3.2-mm diameter tubing (inlet) using a PVC insert fitting (1 cm ID) and (b) glass beads (4 mm) with the injection system embedded. All inlet tubes were connected to two peristaltic pumps to pluviate tracer, CoFe-NP aqueous suspension, and water during the experiments.

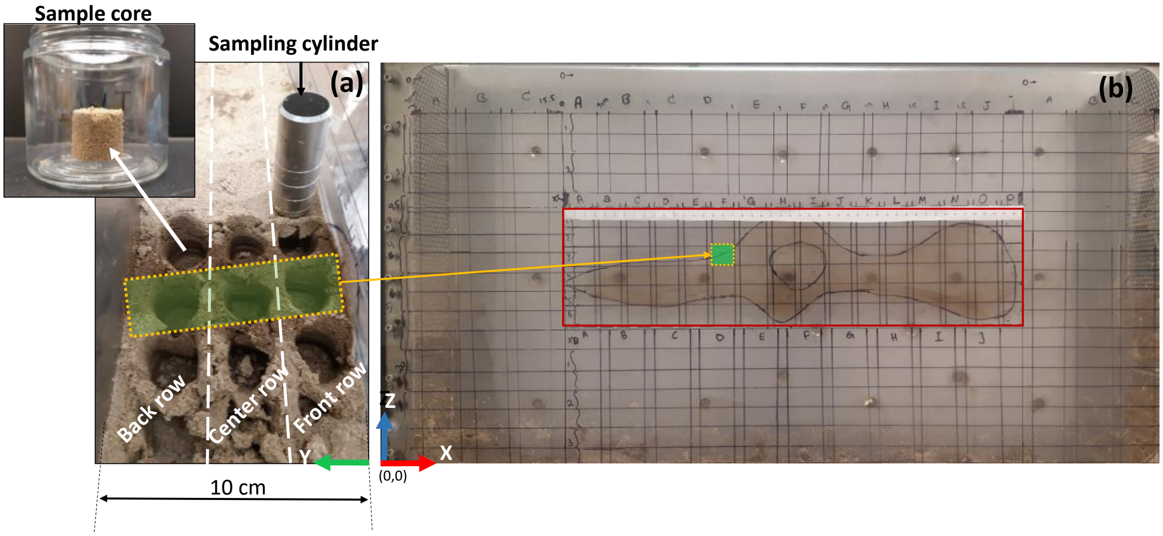

Figure C-4. (a) Sampling across the width of the sand tank from the back (7.9 cm from the front Plexiglas wall), front (2.1 cm) and center (5.0 cm) for a layer at a depth of 28 cm from the base of the tank, and (b) Sampling scheme in the x-z plane; 1-cm deep subsamples were collected from the red rectangular box surrounding the crude oil zone, and 2-cm deep subsamples collected elsewhere. As an example, subsamples in the green box shown in (a) are related to the location F3 (X: 30, Z: 28) on the sampling scheme (b).

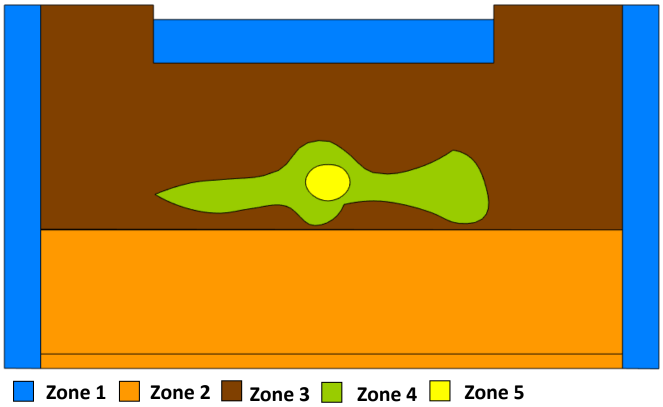

Figure C-5. Specified zones or subregions in the numerical model: Zone 1) infiltration gallery and the two side chambers filled with glass beads, Zone 2) clean BS in the first 20 cm (wet packed; denoted as lower BS zone), Zone 3) clean BS packed in the top 30 cm (denoted as upper BS zone), Zone 4) 2% wt oil zone, and Zone 5) 4% wt oil zone.

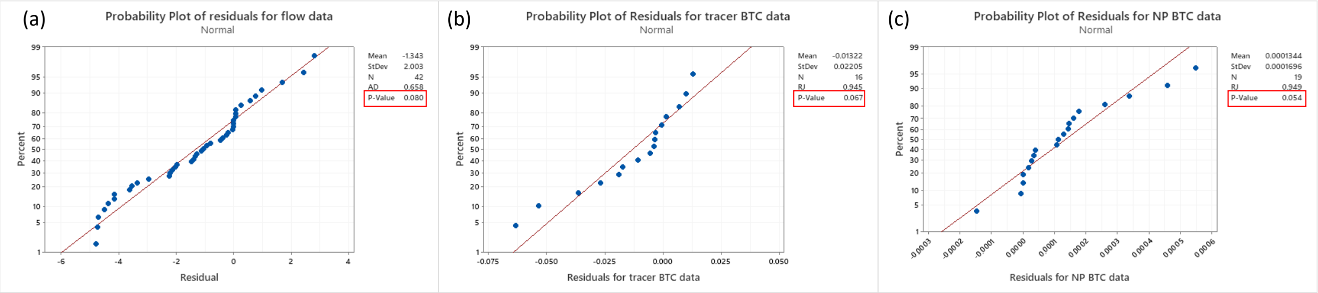

Figure C-6. Normality test for residuals from flow data (a), effluent Br^- data (b), and effluent NP data (c) for tracer and CoFe-NP experiments. Normality was deemed acceptable for *p*-value > 0.05. For the probability plot of the residuals of tracer the tail data points were ignored.

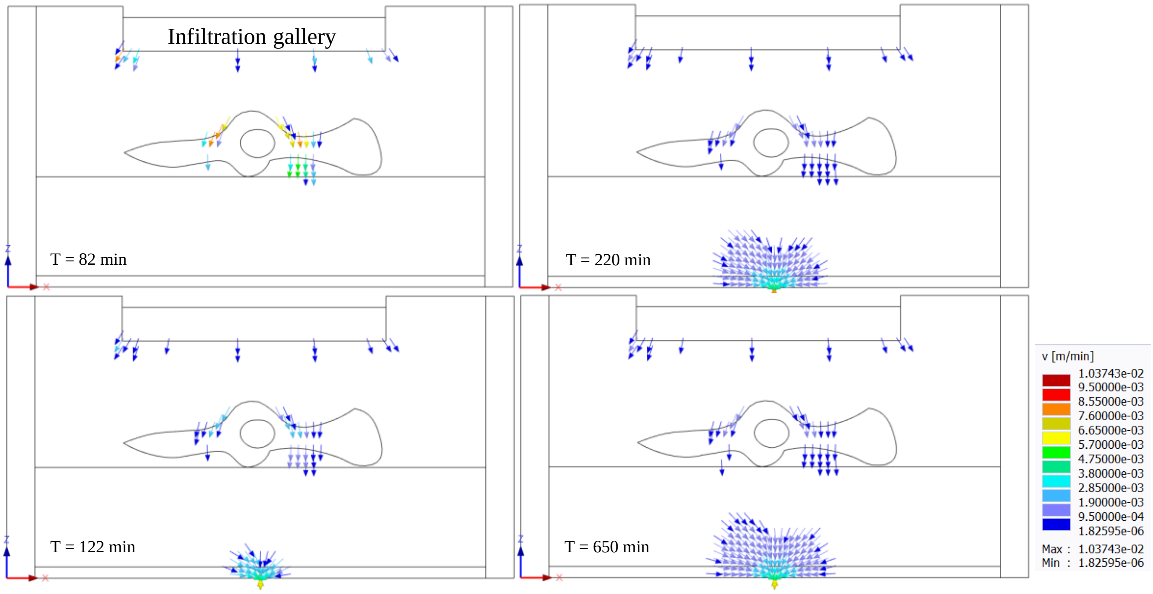

Figure C-7. Spatial distribution of the Darcy flux at different times during tracer transport experiment. Similar pattern was observed for the velocity vectors (or flow streams) from NP transport experiment.

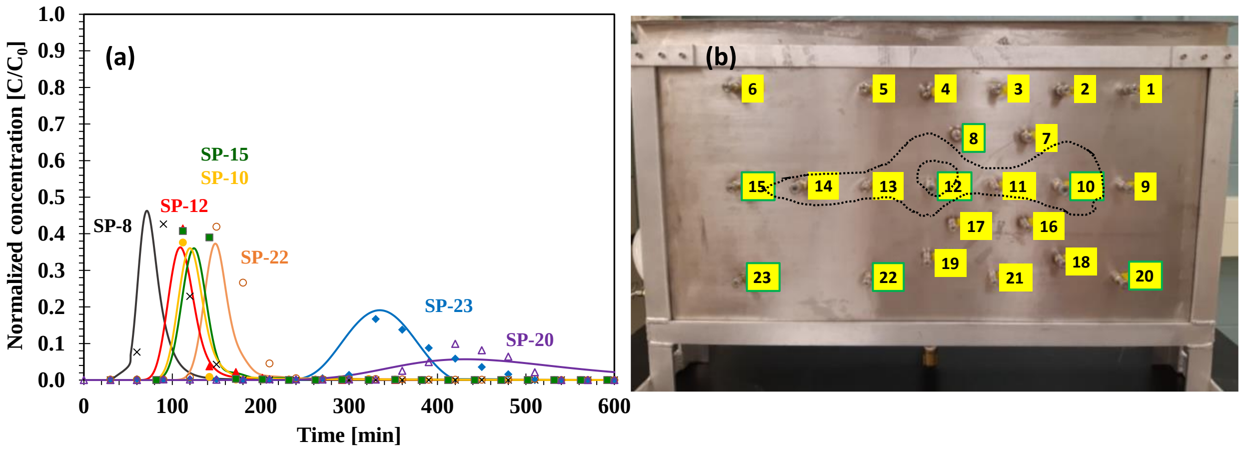

Figure C-9. (a) Observed (symbols) and simulated (lines) Br$^-$ BTCs at different sampling ports and (b) location of the sampling ports at the back of the sand tank. Data for the other ports is not available due to the clogging of the syringe needles by sand grains.

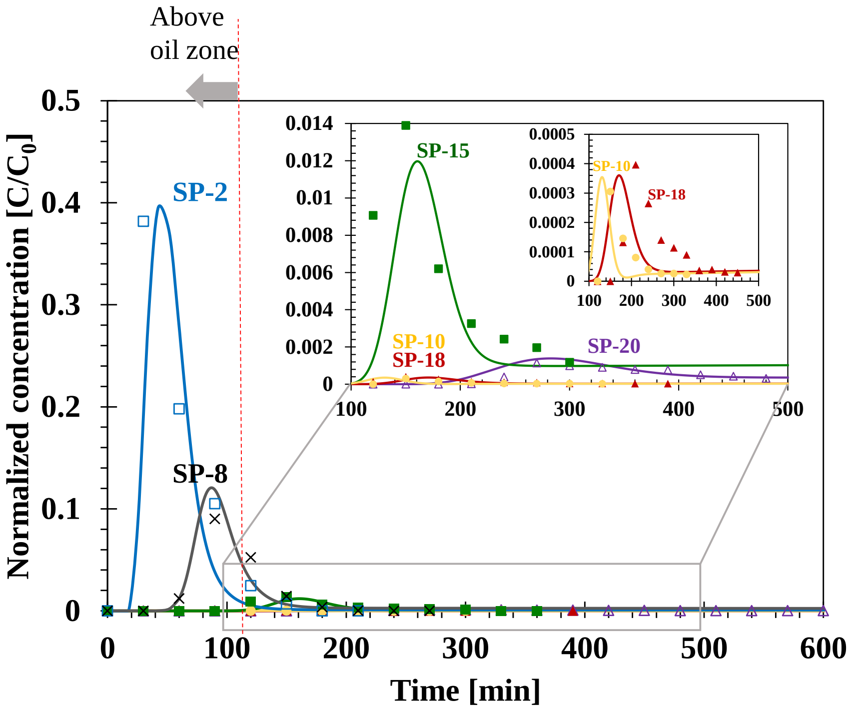

Figure C-10. Observed (symbols) and simulated (lines) CoFe-NP BTCs at different sampling ports. Data for the other sampling ports is not available due to the clogging. SP-2 and SP-8 are located above the oil zone, the rest are within or below the oil zone. For the location of each sampling point see Figure C-10.

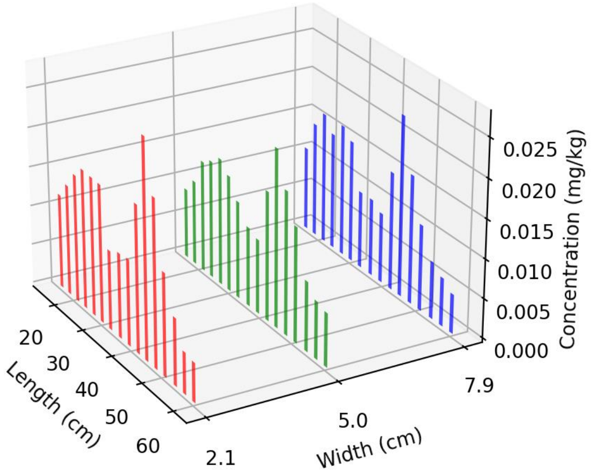

Figure C-11. An example of the observed retained concentration of CoFe-NPs in subsamples collected across the width of the sand tank (back (7.9 cm), front (2.1 cm) and center (5.0 cm rows)) for a layer at of depth of 25.6 cm. Width is from the center of the sampling core to the front Plexiglas wall. This figure clearly indicates that the NP retained concentrations in all rows overlap with each other.